STRUCTURAL INVESTIGATIONS OF NON-HEME FE(II) AND ALPHA-KETOGLUTARATE DEPENDENT DIOXYGENASES USING ELECTRON PARAMAGNETIC RESONANCE SPECTROSCOPY

By

Thomas M. Casey III

A DISSERTATION

Submitted to
Michigan State University
in partial fulfillment of the requirements
for the degree of

Chemistry - Doctor of Philosophy

2013

ABSTRACT

STRUCTURAL INVESTIGATIONS OF NON-HEME FE(II) AND ALPHA-KETOGLUTARATE DEPENDENT DIOXYGENASES USING ELECTRON PARAMAGNETIC RESONANCE SPECTROSCOPY

By

Thomas M. Casey III

Non-heme Fe(II) and alpha-ketoglutarate dependent dioxygenases are a relatively large family of enzymes important in a wide range of biologically and medically relevant processes. Enzymes of this family are believed to use a generally conserved catalytic mechanism and possess a common 2-histidine, 1-carboxylate (typically supplied by Asp/Glu) Fe(II) coordination motif known as a "facial triad." One member of this family, Taurine Hydroxylase (TauD), catalyzes the oxidation of taurine and cofactor alpha-ketogluteric acid (α-KG) to succinate, carbon dioxide (CO_2), and aminoacetylaldehyde using molecular oxygen (O_2). To study the catalytically relevant active site structure with Electron Paramagnetic Resonance Spectroscopy (EPR) enzyme samples were prepared with nitric oxide (NO) as a surrogate to O_2 forming a S=3/2 $\{FeNO\}^7$ centered active site. Using Electron Spin Echo Envelope Modulation (ESEEM) we have measured the position and orientation of taurine in relation to the magnetic axes of the $\{FeNO\}^7$ complex at TauD's active site center. Using Hyperfine Subevel Correlation (HYSCORE), a 2 dimensional version of the ESEEM experiment, we have provided insight into the orientation of directly coordinated His ligands providing a frame of reference for the structural relationship of the substrate and ligands. HYSCORE spectra for samples prepared without substrate or α-KG aided in the understanding of ligand coordination to the $\{FeNO\}^7$

complex. Xanthine Hydroxylase (XanA) is a poorly understood member of this family of enzymes that catalyzes the conversion of xanthine and α-KG to succinate, CO_2, and uric acid. XanA has been shown to allow for growth of Aspergillus nidulans on xanthine as the sole source of nitrogen in the absence of xanthine dehydrogenase activity, the enzyme usually responsible for this function. Homology models based on sequence similarity to TauD have been constructed but are not well studied. The methodology for studying TauD was applied to XanA to provide spectroscopic support for the homology model.

ACKNOWLEDGEMENTS

I would first like to thank Dr. John McCracken for the opportunity to join his research group and learn under his guidance. His patience while instilling important knowledge have made any success I've achieved possible.

I would also like to thank Dr. Bob Hausinger for his help and support throughout my research efforts. A special thanks to Piotr Grzyska for providing the Taurine Hydroxylase enzyme samples used in this study. Also, William Kittleman for providing the Xanthine Hydroxylase enzyme samples. Thanks to Rahul Banerjee under the guidance of Dr. Robert Cukier for his assistance in performing a geometry optimization of a crystal structure used for comparison in this thesis.

I would like to acknowledge the assistance in data analysis, MATLAB programming, and learning provided by Matt Krzyaniak and Mike Howart. Their help was instrumental in the completion of my thesis work.

A thank you to my committee: Dr. David Weliky, Dr. Robert Cukier, and Dr. Dana Spence for allowing me the opportunity to continue my graduate career.

An important thank you to Dr. Michael Sevilla at Oakland University. Dr. Sevilla gave me a chance to experience scientific research for the first time as an undergraduate student. The research environment he allowed me to participate in made a career in chemistry something I would like to pursue.

Lastly, thank you to my Dad (Tom), Mom (Karen), Sister (Kristen), Brother (Jeff), and fiancée (Angela) for all you did to support me over these past 5 years. I love you all!

TABLE OF CONTENTS

LIST OF TABLES

LIST OF FIGURES

LIST OF SYMBOLS AND ABBREVIATIONS

ΔE - Energy difference

^{14}N - Nitrogen

1GVG - Crystal structure for Clavaminate Synthase

1GY9 - Crystal structure for TauD

^{1}H - Hydrogen

1OS7 - Crystal structures for TauD

^{2}H - Deuterium

$\boldsymbol{A}$ - Hyperfine coupling tensor

a.u. - arbitrary units

a_{iso} - Isotropic hyperfine coupling constant

ANS - Anthocyanidin synthase

Asp - Aspartic Acid

B_0 - magnetic field strength

CarC - Carbapenem Synthase

CAS - Clavaminate synthase

CD - Circular Dichroism

cm^{-1} - wavenumbers

CO_2 - Carbon dioxide

Cov - covariance matrix

CW EPR - Continuous Wave Electron Paramagnetic Resonance

D - Magnitude of the Zero field splitting

DAOCS - deacetoxycephalosporin N synthase

DFT - Density Functional Theory

dx_n - change in parameter used in calculating Jacobian matrix terms

e - electric charge

E - Rhombic Zero field splitting parameter

e^2Qq/h - Quadrupole coupling strength

EDTA - Ethylenediamineteraacetic acid

ENDOR - Electron Nuclear Double Resonance

EPR - Electron Paramagnetic Resonance

ESEEM - Electron Spin Echo Envelope Modulation

f - function

Fe - Iron

g - g factor

g_e - free electron g value

g_{eff} - effective g value

Glu - Glutamate

g_n - Nuclear g value

$\hat{H}$ - Hamiltonian Operator

h - Planck's constant

HF - Hyperfine

HFI - Hyperfine Interaction

His - Histidine

HSO_3^- - Bisulfite

HYSCORE - Hyperfine Sub level Correlation

Hz - Hertz

I - nuclear spin

$\hat{I}$ - nuclear spin operator

IPNS - Isopenicillin N synthase

J - Joules

$J_{n \times m}$ - Jacobian matrix of *n* parameters and *m* data points

K - Kelvin

k_B - Boltzman's constant

K_i - Annealing parameter

L-DOPA - L-3,4-dihydroxyphenylalanine

lwpp - Line width parameter

m.w. - microwave

MCD - Magnetic Circular Dichroism

M_D - Density matrix

M_I - nuclear spin quantum number

MO - Molecular Orbital

M_S - electron spin quantum number

mT - Millitesla

NO - Nitric oxide

NQI - Nuclear Quadrupole Interaction

N_α - Population in the α (M_S=+1/2) spin state

N_β - Population in the β (M_S=-1/2) spin state

O_2 - Molecular Oxygen

P_i - probability of acceptance in simulated annealing

p_n - individual parameter

p_n - individual parameter varied in fitting

q - electric field gradient

Q - Nuclear quadrupole moment

Q" - Quadrupole coupling tensor

R(α, β, γ) - 3 dimensional rotation matrix for translating tensor orientations

rR - Resonance Raman

S - electron spin

s - seconds

$\hat{S}$ - Spin operator

SDFT-PT - spin density functional theory perturbation theory

$\hat{S}_x$ - Spin operator for x component of spin angular momentum

$\hat{S}_y$ - Spin operator for y component of spin angular momentum

$\hat{S}_z$ - Spin operator for z component of spin angular momentum

T - dipolar coupling strength (MHz)

T - Temperature

T_0 - initial temperature parameter for simulated annealing

T_1 - Spin-lattice relaxation time

T1 - time spacing for microwave pulse sequences

T2 - time spacing for microwave pulse sequences

TauD - Taurine Hydroxylase

TfdA - 2,4-dichlorophenoxyacetate/α-KG dioxygenase

T_i - temperature parameter for simulated annealing

TWT - Traveling Wave Tube amplifier

TyrH - Tyrosine Hydroxylase

UF - Unified Field

UV/VIS - Ultraviolet/Visible Spectroscopy

XanA - Xanthine Hydroxylase

XAS - X-Ray absorption spectroscopy

y_m - individual point in data set subject to fitting

ZFS - Zero field splitting

α-KG - alpha-ketogluteric acid

β_e - Bohr magneton

β_N - Nuclear magneton

δ - isomer shift in Mössbauer spectroscopy

η - Quadrupole asymmetry parameter

ν - Frequency

ρ - Hyperfine asymmetry parameter

σ - standard deviation

τ - time spacing

χ^2 - sum of the square of residuals

ω - angular frequency

CHAPTER 1

NON-HEME FE(II)/ALPHA KETOGLUTARATE DEPENDENT HYDROXYLASES

INTRODUCTION

Non-heme mononuclear Fe(II) centered enzymes that oxidize a target substrate make up one of the largest and most diverse family of enzymes currently known **(1)**. Enzymes in this family are capable of activating molecular oxygen (O_2) to catalyze a variety of oxidative reactions that are important in synthesis, degradation, and various manipulations of biomolecules. The largest and most diverse class of enzymes belonging to this family is dependent on the cofactor alpha ketoglutarate (α-KG) **(2-4)**. Most members of this class couple an oxidative decarboxylation of α-KG to the hydroxylation of a relatively inert C-H bond. Figure 1.1 illustrates the basic hydroxylation reaction.

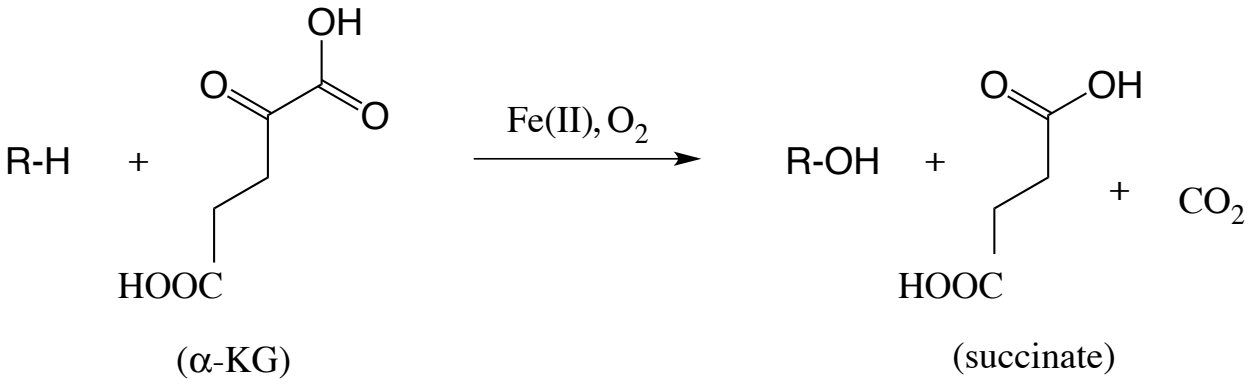

Figure 1.1 The α-KG dependent hydroxylases couple the oxidative decarboxylation of α-KG to the hydroxylation of a C-H bond on the target substrate. One molecule of succinate and CO_2 are liberated in the process.

Despite the diversity of substrates recognized by this class, all enzymes have a generally conserved tertiary structure for the substrate binding pocket, a common Fe(II) coordination motif, and are believed to use a generally conserved catalytic mechanism **(2, 5, 6)**. This family of enzymes has been studied extensively and much is known about their structure and function but some details of the atomic level structure at the catalytic site are still unclear. This chapter introduces the generally accepted structural and mechanistic details for enzymes in this family and proposes Electron Paramagnetic Resonance (EPR) spectroscopy as a technique for the study of interesting structural characteristics near the non-heme Fe(II) catalytic center.

1.1 NON-HEME FE(II)/α-KG DEPENDENT ENZYME STRUCTURE

All non-heme mononuclear Fe(II) dependent enzymes share structural characteristics that are conserved throughout the family regardless of the cofactor, substrate, or reaction catalyzed **(1-4)**. Figure 1.2 illustrates the "facial triad" Fe(II) coordination motif.

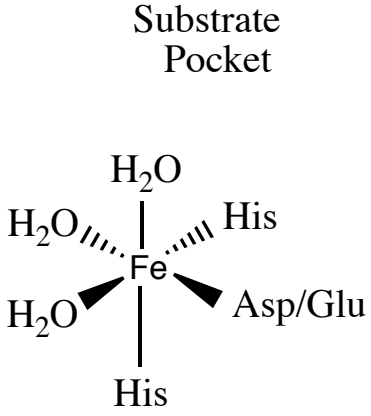

Figure 1.2 The iron center is coordinated by two histidine ligands and one carboxylate that is supplied by either a glutamate or aspartic acid residue making for a "facial triad."

This Fe(II) coordination motif is termed a “facial triad” because three ligands occupy one face of an octahedral complex **(7)**. Two of the ligands are histidyls and are invariably supplied by histidine residues while the third ligand, a carboxylate ligand, can be supplied by either an aspartate or a glutamate residue. Prior to the arrival of the cofactor and primary substrate, the remaining coordination positions are occupied by water ligands. Various crystal structures for enzymes in this family are available and show this Fe(II) binding motif **(8-11)**. Tyrosine hydroxylase (TyrH), a pterin dependent hydroxylase that is responsible for the conversion of L-tyrosine to L-3,4-dihydroxyphenylalanine (L-DOPA), has its His331 residue coordinated trans to the substrate binding pocket (hereafter referred to as “axial”) while His336 and Glu376 are coordinated in the perpendicular plane (hereafter referred to as “equatorial”) **(12)** (see Figure 1.2). Isopenicillin N synthase (IPNS), an enzyme responsible for the production of the antibiotic Isopenicillin N from component amino acids, has His270 in the axial position while His214 is accompanied by Asp216 in equatorial positions **(13)**. The necessity for these endogenous amino acid ligands for proper function has been confirmed with site directed mutagenasis but the mechanistic involvement does not appear to be direct. Instead, it appears that the 2-His-1-Carboxylate motif is important in the proper anchoring of the Fe(II) for further ligation during the catalytic mechanism **(14)**.

Within this enzyme family the class that is dependent on the cofactor α-KG is the largest and is known to involve the most diverse range of substrates **(2)**. In addition to the conserved “facial triad”, enzymes in this class all have a common “jelly roll” structural fold that defines the substrate binding pocket **(15, 16)**. This fold consists of α helices and β strands that provide the necessary protein contacts for stabilization of the substrate near the Fe(II) coordination sphere. In

contrast to the primary substrate, α-KG is directly coordinated to the Fe(II) in a bidentate fashion in two of the three open coordination sites via its C1 carboxylate and C2 keto groups **(2, 4)**. The C5 carboxylate of α-KG is also stabilized by protein contacts supplied by Arg or Lys and an additional Arg residue helps orient the C1 carboxylate. The C2 keto group invariably binds trans to the carboxylate (Asp/Glu) ligand of the "facial triad" while the binding of the C1 carboxylate ligand can be in two different positions: either in the equatorial plane ("in line") cis to both histidine ligands or in the axial position trans to the axial histidine ligand ("off line"). Figure 1.3 illustrates the "in line" and "off line" binding modes.

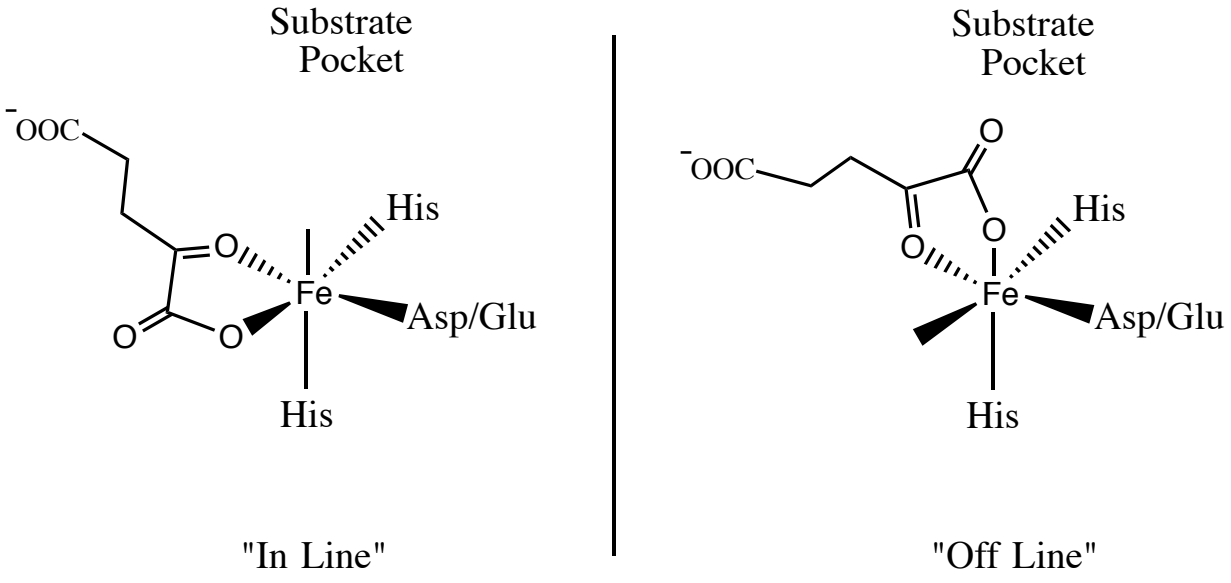

Figure 1.3. The "in line" α-KG binding mode leaves an open coordination site for O_2 that is oriented trans to the axial histidine. The "off line" mode leaves the open site in the equatorial plane oriented trans to the equatorial histidine.

The "in line" binding mode has the sixth coordination site oriented toward the substrate binding pocket trans to the axial histidine ligand. Enzymes that exhibit this α-KG binding mode include Clavaminate Synthase (CAS), involved in the synthesis of a potent β-lactamase inhibitor

clavulanic acid by hydroxylation of deoxyguanidinoproclavaminic acid **(17)** and an enzyme termed FIH, a factor inducing the hypoxia-inducible factor (HIF) by hydroxylation of a c-terminal transactivation domain **(18)**. The "off line" binding mode has the sixth coordination site oriented in the equatorial plane, away from the substrate pocket, trans to the equatorial histidine. Enzymes with this binding mode include carbapenem synthase (CarC), responsible for epimerization and desaturation of (3S,5S)-carbapenem to (5R)-carbapenem in the biosynthesis of carbapenem based antibiotics **(19)**, and Anthocyanidin synthase (ANS), that catalyzes important epimerizations in the synthesis of flavanoids in plants **(20, 21)**. Interestingly, another enzyme deacetoxycephalosporin C synthase (DAOCS), responsible for ring expansion of penicillin N into deacetoxycephalosporin C, exhibits a unique binding mode in which the α-KG chelates the Fe(II) in the same fashion as in the "off line" mode but the substrate binding position is coincident with the position of the C5 carboxylate group of the α-KG **(22)**. This results in either the binding of substrate or α-KG but not both simultaneously. The same general oxidative capacity of enzymes having distinctly different cofactor binding modes is intriguing and will be put in the context of the generally accepted mechanism.

1.2 HYDROXYLASE MECHANISM

Multiple results of oxidations catalyzed by these enzymes are possible including hydroxylation, repair of methylated DNA and RNA, epimerization, and ring manipulation **(2, 3, 23, 24)**. Figure 1.4 lists some of the general reactions catalyzed by α-KG dependent enzymes.

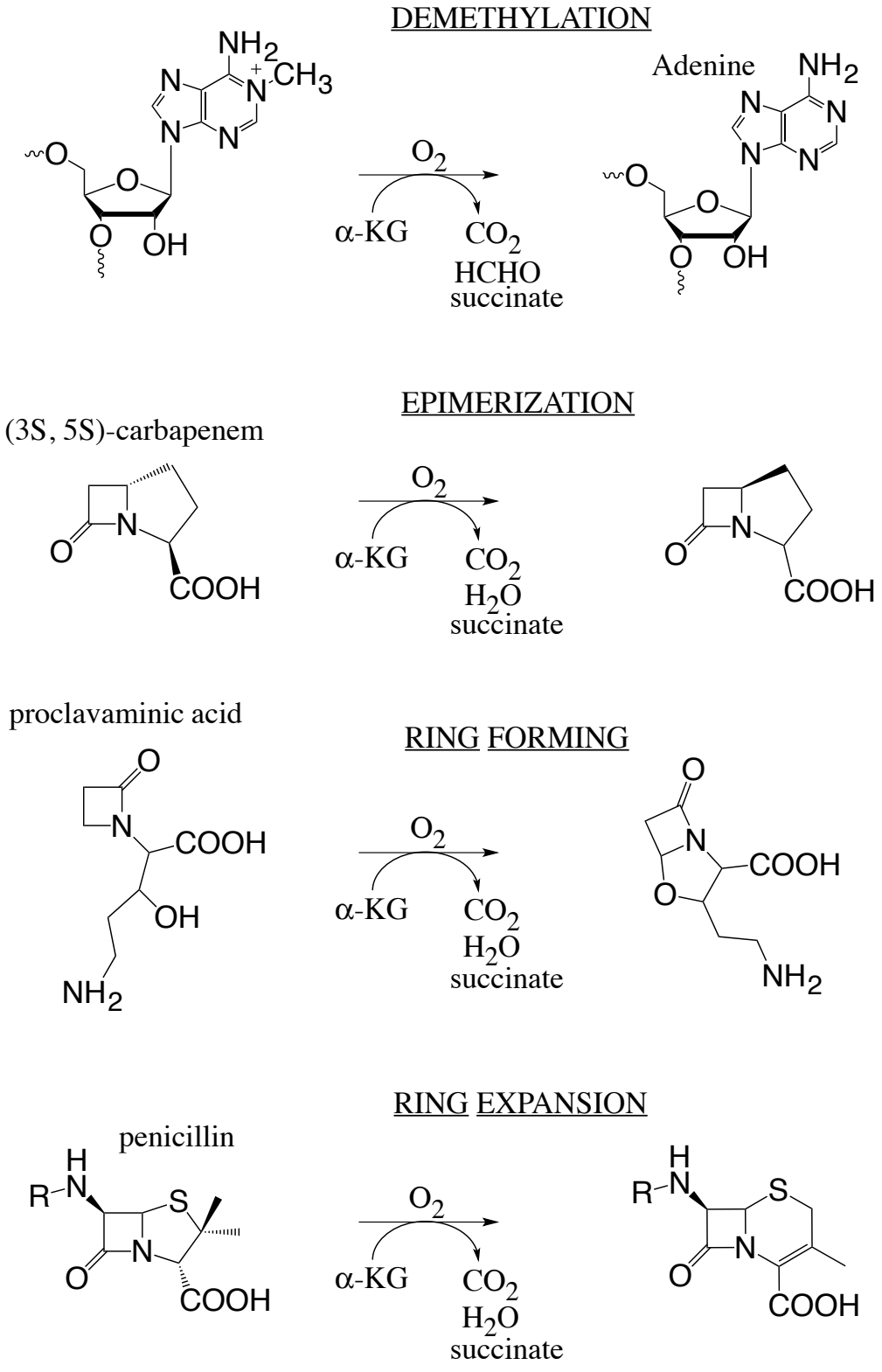

Figure 1.4. The repair of methylated adenine is catalyzed by the DNA repair enzyme AlkB, the epimerization on (3S,5S)-carbapenem is catalyzed by CarC, the ring formation on proclavaminic acid is catalyzed by CAS, and the ring expansion of penicillin is catalyzed by DAOCS.

Although there are a multitude of reactions available, the initial steps in the mechanism remain generally conserved **(1, 5, 6, 25-27)**. Figure 1.5 illustrates the detailed hydroxylase mechanism.

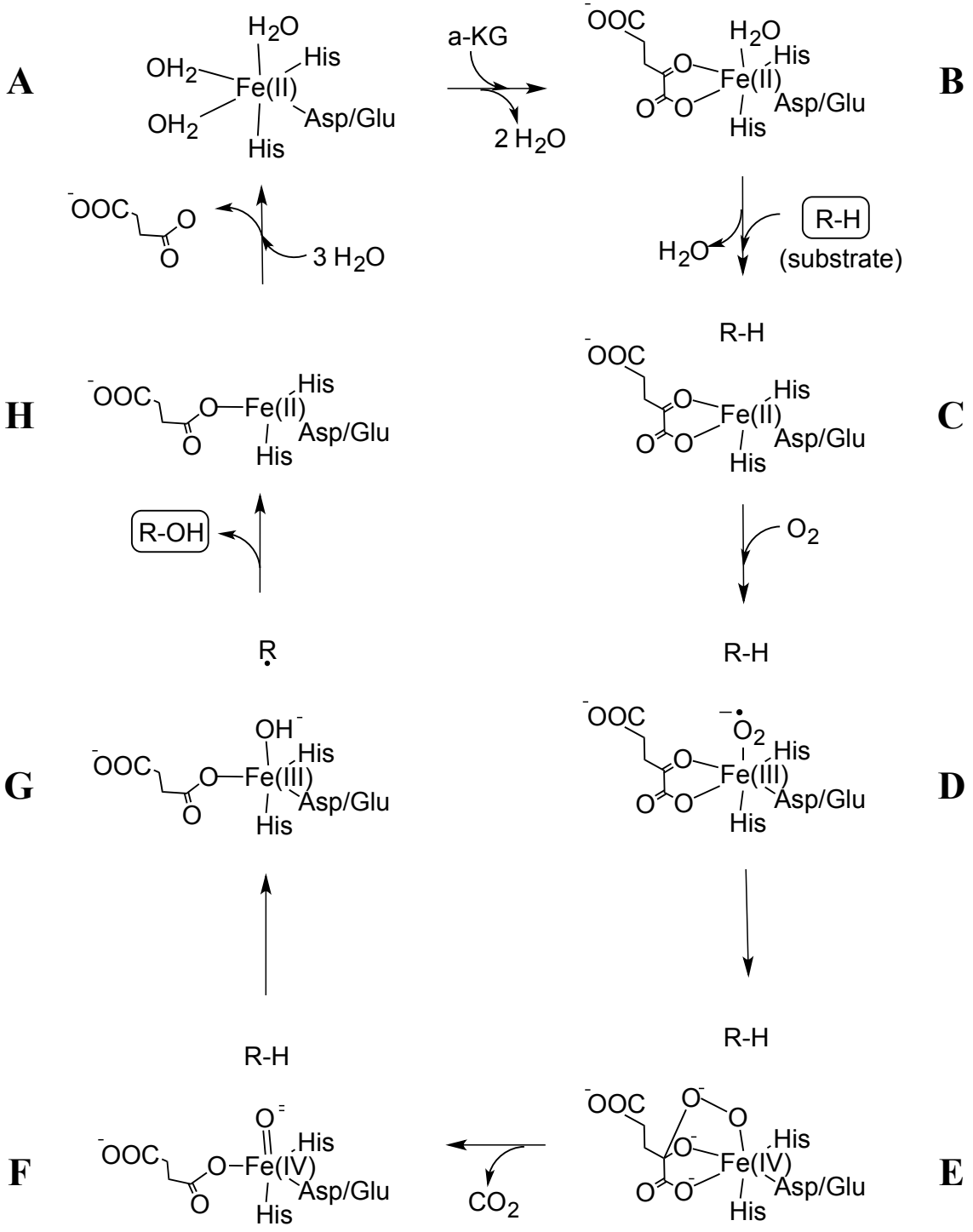

Figure 1.5. The generally accepted mechanism involves the formation of a highly reactive Fe(IV)=O species that abstracts a hydrogen from the primary substrate. The hydroxylation is believed to occur via radical rebound chemistry. This mechanism was first proposed in 1982 by Hanuaske-Abel et al. in a study of inhibitory behavior in prolyl hydroxylase (28). To date, several experimental and computational findings for similar enzymes have supported the proposed intermediates (2, 29).

The facially coordinated Fe(II) has three remaining coordination sites occupied by water molecules prior to chelation by α-KG and arrival of the primary substrate. In the first step, the bidentate chelation of α-KG displaces two water molecules. One representative study involved the use of circular dichroism (CD) to probe metal and α-KG binding in CAS **(30)**. A band at ~8500 cm^{-1} was observed after addition of Fe(II) to apo CAS that represents the chelation of the Fe(II) ion. Appearance of an additional band at ~29,000 cm^{-1} was coincident with treating the protein with α-KG. This signature was assigned to the bidentate chelation by α-KG and the displacement of two water molecules. The next step is displacement of the final water molecule upon arrival of the primary substrate. A herbicide degrading enzyme 2,4-dichlorophenoxyacetate/ α-KG dioxygenase (TfdA) was analyzed with X-Ray absorption spectroscopy to probe the Fe(II) coordination environment during substrate binding **(31)**. Data confirmed a 5 coordinate Fe(II) after treatment of the protein/Fe(II)/α-KG solution with the primary substrate. Although the substrate is not directly bound to the metal ion, it clearly facilitates the displacement of the remaining water in preparation for O_2 arrival. Previous studies had suggested that the O_2 can coordinate the Fe(II) center prior to the arrival of the primary substrate based on the observation of uncoupled α-KG decarboxylation **(32, 33)**. This uncoupled reactivity, however, is slow compared to the characteristic enzymatic behavior. More recent circular dichroism (CD) and magnetic circular dichroism (MCD) studies for CAS and various spectroscopic studies from the Hausinger group have shown that the reactive 5 coordinate active site that binds O_2 is only observed in the presence of α-KG along with the primary substrate **(34-36)**. This is also supported by the observation of six coordinate ferrous iron that is relatively unreactive towards

O_2. Figure 1.5(D-H) illustrates the steps following the arrival of O_2 for the hydroxylase mechanism. After coordination of the O_2 molecule to Fe(II) forming Fe(III)-superoxide, an oxidative attack by the superoxo group at the C2 position on α-KG results in the decarboxylation of α-KG and the heterolytic cleavage of the O-O bond. The product is a highly reactive Fe(IV)=O complex **(35, 37)**. The splitting of oxygen by this process has been well studied both spectroscopically and computationally and the spectroscopic signatures for several of the intermediates have been identified **(25, 38, 39)**. The archetype enzyme taurine hydroxylase (TauD) that catalyzes the degradation of taurine to bisulfite and aminoacetaldehyde was used in one study to observe the Fe(IV)=O complex **(40)**. Freeze-quench Mössbauer spectroscopy showed the accumulation of a species that gives a quadrupole doublet with $\delta = 0.31$ mm/s and $\Delta E_Q = 0.88$ mm/s, characteristic of the Fe(IV)=O complex. In the same study, using stopped flow absorption, the appearance and disappearance of an absorption feature at 318 nm was assigned to the generation and reaction of the Fe(IV)=O species. The assumption that the following steps of the reaction involve the abstraction of hydrogen from the substrate has been generally accepted and confirmed in multiple studies since it was first proposed in 1982 **(1, 28)**. A recent study by the Hausinger group using [^{1}H/^{2}H]-taurine confirmed the Fe(IV)=O species as the hydrogen abstracting intermediate by monitoring the characteristic UV/VIS feature at 318 nm and noticing a 37 fold decrease in decay rate with deuterated taurine **(36)**. Other studies have also shown a large kinetic isotope effect when the target C-H position is labeled with deuterium suggesting that a hydrogen abstraction is the rate determining step **(41, 42)**. More recently, Grzyska et al. observed isotope sensitive O-O stretching modes in resonance Raman (rR) data on TauD protein complexes that suggest the possibility of an additional pathway for the steps

following the generation of the Fe(IV)=O **(36)**. Figure 1.6 illustrates the proposed alternate pathway for the hydroxylation of taurine.

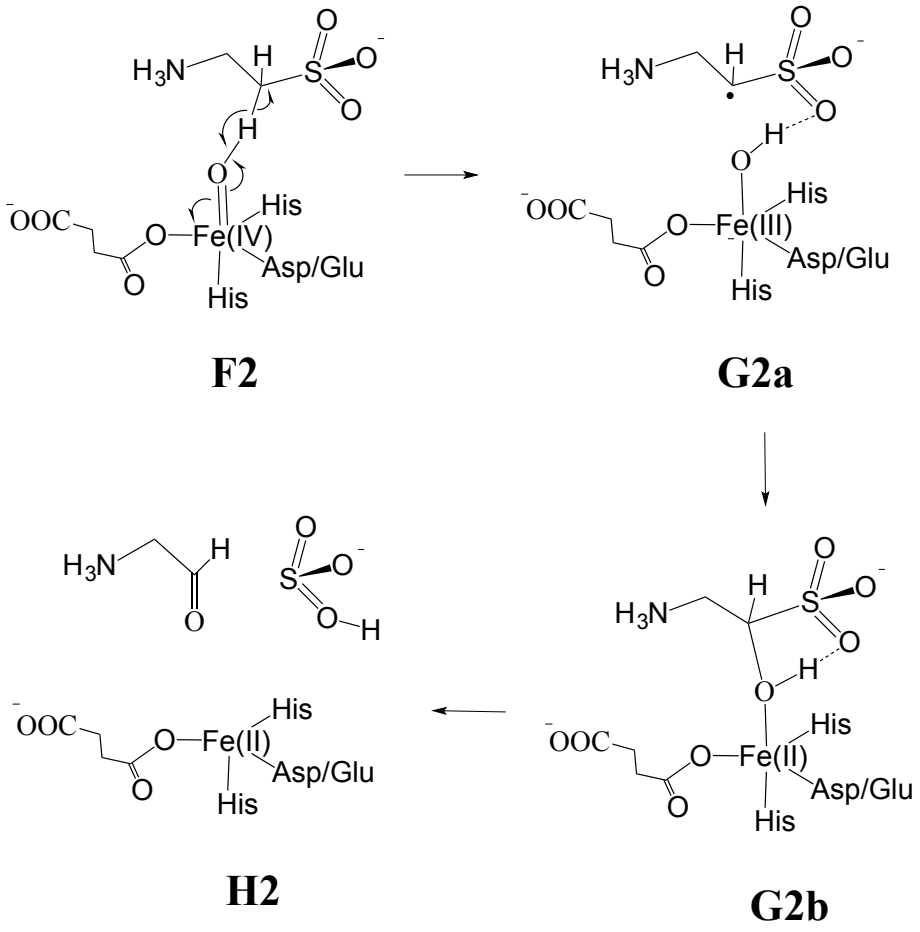

Figure 1.6. Expanding on complex F in Figure 1.5, F2 depicts the attack by the Fe(IV)=O complex on the C1 bound hydrogen on taurine. G2a depicts the stabilizing interaction of the hydroxyl proton on the Fe(III)-OH complex with one of taurine's sulfite oxygens. G2b depicts the direct attack of the hydroxyl oxygen on the C1 radical forming an alkoxide. H2 is the products complex showing the oxidation of the C-OH to a C=O bond that is eventual in the previously described mechanism as being the result of the hydrogen atom leaving as a part of bisulfite **(35)**.

Observation of three isotope sensitive O-O modes in rR spectra following the Fe(IV)=O complex were assigned to key steps in two possible pathways. One being the generally proposed hydrogen abstraction followed by radical rebound chemistry and the other being the formation of a Fe(III)-

O^- complex (Figure 1.6 G2a) and direct attack on the primary substrate (Figure 1.6 G2b). Various computational studies have provided calculated energies involved in the proposed reactions and bonding involved at each step of the mechanism **(6, 38, 43-45)**. One such study calculated the potential energy surface associated with the hydrogen abstraction step carried out by the Fe(IV)=O intermediate in the TauD enzyme complex **(46)**. The calculations suggested that abstraction of the proton at the C1 position on taurine is indeed an energetically challenging and likely rate limiting step but the following hydroxylation step by carbon radical rebound would have a relatively minimal energy barrier. The calculations also suggested that formation of a Fe-O-C alkoxy complex is unlikely because the predicted O-C bond distances are uncharacteristically long (~2.68 Å). In the same study that used stopped-flow absorption to probe the steps leading up to the generation of the Fe(IV)=O species **(40)**, the appearance of a feature at 520 nm in parallel to the disappearance of the Fe(IV)=O signature at 318 nm was assigned to the accumulation of the 4 coordinate Fe(II)-products complex that would consist of the "facial triad" ligands and succinate.

1.3 CONCLUSIONS

The initial "in line" binding of α-KG would result in the orientation of the Fe(IV)=O that is desirable for the mechanism to proceed as described. For the same mechanism to occur with the "off line" mode, there must be either a reorientation of the α-KG prior to oxidative decarboxylation on α-KG or a change in the orientation of the Fe(IV)=O after removal of the resulting CO_2 (see Figure 1.3). Reorientation of α-KG would require conformational flexibility in the surrounding protein that would normally stabilize the position of α-KG. A change in the

orientation of the Fe(IV)=O would suggest that the same chemistry leading to the Fe(IV)=O species takes place in the equatorial plane and is followed by a "ferryl flip" **(9)** when the loss of CO_2 provides an open coordination site. While spectroscopic evidence for the coordination number, nature of bonds to Fe, and the electronic structure of the complex at various steps in the mechanism exists in abundance there is no direct evidence for either of these reorientation steps or the relative orientation of the ligands, most notably the bound O_2. The hydrogen abstraction followed by radical rebound pathway or the proposed direct attack by the Fe(IV)=O on a carbon radical would each require different degrees of specificity of substrate position. Crystallographic data and mutagenasis studies **(1, 2, 4, 5, 7, 8)** can provide insight into the protein structure that defines the substrate binding pocket and can give a general picture of the substrate orientation but do not represent the direct correlation of substrate nuclei to any of the intermediate iron-oxo complexes that would be necessary to support any specific substrate position that might suggest one of the two proposed reaction pathways. Introduction of a new spectroscopic method has provided the ability for direct correlation of substrate nuclei to the Fe(II) complex and a probe for the relative position of directly coordinated ligands. After treatment of anaerobic protein solutions with nitric oxide (NO) a half integer spin Fe-NO complex is formed that is amenable to study with Electron Paramagnetic Resonance (EPR) spectroscopy that also mimics the Fe-O_2 complex native to the functioning enzyme **(47-49)**. With isotopic labeling on the primary substrate, pulsed EPR techniques, and statistical analysis procedures for interpreting data, direct measurements of the position of the substrate and the orientation of coordinated ligands relative to the magnetic axes of the Fe-NO complex are attainable. The next chapter will introduce the

electronic structure of the Fe-NO complex and describe methods for the exploitation of it's properties to gain structural information using EPR experiments.

BIBLIOGRAPHY

BIBLIOGRAPHY

1. Costas, M., M. P. Mehn, M. P. Jensen, and L. Que. 2004. Dioxygen activation at mononuclear nonheme iron active sites: Enzymes, models, and intermediates. Chem. Rev. 104:939-986.

2. Hausinger, R. P. 2004. Fe(II)/alpha-ketoglutarate-dependent hydroxylases and related enzymes. Crit Rev Biochem Mol 39:21-68.

3. Purpero, V., and G. R. Moran. 2007. The diverse and pervasive chemistries of the alpha-keto acid dependent enzymes. J Biol Inorg Chem 12:587-601.

4. McDonough, M. A., C. Loenarz, R. Chowdhury, I. J. Clifton, and C. J. Schofield. 2010. Structural studies on human 2-oxoglutarate dependent oxygenases. Curr Opin Struc Biol 20:659-672.

5. He, P. Q., and G. R. Moran. 2011. Structural and mechanistic comparisons of the metal-binding members of the vicinal oxygen chelate (VOC) superfamily. J Inorg Biochem 105:1259-1272.

6. Ye, S. F., C. Riplinger, A. Hansen, C. Krebs, J. M. Bollinger, and F. Neese. 2012. Electronic Structure Analysis of the Oxygen-Activation Mechanism by Fe-II- and alpha-Ketoglutarate (alpha KG)-Dependent Dioxygenases. Chem-Eur J 18:6555-6567.

7. Hegg, E. L., and L. Que. 1997. The 2-His-1-carboxylate facial triad - An emerging structural motif in mononuclear non-heme iron(II) enzymes. Eur J Biochem 250:625-629.

8. Andreini, C., I. Bertini, G. Cavallaro, R. J. Najmanovich, and J. M. Thornton. 2009. Structural Analysis of Metal Sites in Proteins: Non-heme Iron Sites as a Case Study. J Mol Biol 388:356-380.

9. Zhang, Z. H., J. S. Ren, K. Harlos, C. H. McKinnon, I. J. Clifton, and C. J. Schofield. 2002. Crystal structure of a clavaminate synthase-Fe(II)-2-oxoglutarate-substrate-NO complex: evidence for metal centred rearrangements. Febs Lett 517:7-12.

10. Elkins, J. M., M. J. Ryle, I. J. Clifton, J. C. D. Hotopp, J. S. Lloyd, N. I. Burzlaff, J. E. Baldwin, R. P. Hausinger, and P. L. Roach. 2002. X-ray crystal structure of Escherichia coli taurine/alpha-ketoglutarate dioxygenase complexed to ferrous iron and substrates. Biochemistry-Us 41:5185-5192.

11. O'Brien, J. R., D. J. Schuller, V. S. Yang, B. D. Dillard, and W. N. Lanzilotta. 2003. Substrate-induced conformational changes in Escherichia coli taurine/alpha-ketoglutarate dioxygenase and insight into the oligomeric structure. Biochemistry-Us 42:5547-5554.

12. Fitzpatrick, P. F. 2000. The aromatic amino acid hydroxylases. Adv Enzymol Ramb 74:235-+.

13. Kreisberg-Zakarin, R., I. Borovok, M. Yanko, F. Frolow, Y. Aharonowitz, and G. Cohen. 2000. Structure-function studies of the non-heme iron active site of isopenicillin N synthase: some implications for catalysis. Biophys Chem 86:109-118.

14. Koehntop, K. D., J. P. Emerson, and L. Que. 2005. The 2-His-1-carboxylate facial triad: a versatile platform for dioxygen activation by mononuclear non-heme iron(II) enzymes. J Biol Inorg Chem 10:87-93.

15. Roach, P. L., I. J. Clifton, V. Fulop, K. Harlos, G. J. Barton, J. Hajdu, I. Andersson, C. J. Schofield, and J. E. Baldwin. 1995. Crystal-Structure of Isopenicillin N-Synthase Is the First from a New Structural Family of Enzymes. Nature 375:700-704.

16. Aik, W., M. A. McDonough, A. Thalhammer, R. Chowdhury, and C. J. Schofield. 2012. Role of the jelly-roll fold in substrate binding by 2-oxoglutarate oxygenases. Curr Opin Struc Biol 22:691-700.

17. Zhou, J., M. Gunsior, B. O. Bachmann, C. A. Townsend, and E. I. Solomon. 1998. Substrate binding to the alpha-ketoglutarate-dependent non-heme iron enzyme clavaminate synthase 2: Coupling mechanism of oxidative decarboxylation and hydroxylation. J Am Chem Soc 120:13539-13540.

18. Srinivas, V., X. Zhu, S. Salceda, R. Nakamura, and J. Caro. 1998. Hypoxia-inducible factor 1 alpha (HIF-1 alpha) is a non-heme iron protein - Implications for oxygen sensing. J Biol Chem 273:18019-18022.

19. Clifton, I. J., L. X. Doan, M. C. Sleeman, M. Topf, H. Suzuki, R. C. Wilmouth, and C. J. Schofield. 2003. Crystal structure of carbapenem synthase (CarC). J Biol Chem 278:20843-20850.

20. Turnbull, J. J., J. Nakajima, R. W. D. Welford, M. Yamazaki, K. Saito, and C. J. Schofield. 2004. Mechanistic studies on three 2-oxoglutarate-dependent oxygenases of flavonoid biosynthesis - Anthocyanidin synthase, flavonol synthase, and flavanone 3 beta-hydroxylase. J Biol Chem 279:1206-1216.

21. Welford, R. W. D., I. J. Clifton, J. J. Turnbull, S. C. Wilson, and C. J. Schofield. 2005. Structural and mechanistic studies on anthocyanidin synthase catalysed oxidation of flavanone substrates: the effect of C-2 stereochemistry on product selectivity and mechanism. Org Biomol Chem 3:3117-3126.

22. Oster, L. M., A. C. T. van Scheltinga, K. Valegard, A. M. Hose, A. Dubus, J. Hajdu, and I. Andersson. 2004. Conformational flexibility of the C terminus with implications for substrate

binding and catalysis revealed in a new crystal form of deacetoxycephalosporin C synthase. J Mol Biol 343:157-171.

23. Krebs, C., D. G. Fujimori, C. T. Walsh, and J. M. Bollinger. 2007. Non-heme Fe(IV)-oxo intermediates. Accounts Chem Res 40:484-492.

24. Nam, W. 2007. High-valent iron(IV)-oxo complexes of heme and non-heme ligands in oxygenation reactions. Accounts Chem Res 40:522-531.

25. Solomon, E. I. 2003. Structure/function correlations over non-heme iron enzymes. J Inorg Biochem 96:62-62.

26. Solomon, E. I. 1999. Geometric and electronic structure contributions to function in non-heme iron enzymes. J Inorg Biochem 74:5-5.

27. Abu-Omar, M. M., A. Loaiza, and N. Hontzeas. 2005. Reaction mechanisms of mononuclear non-heme iron oxygenases. Chem. Rev. 105:2227-2252.

28. Hanauskeabel, H. M., and V. Gunzler. 1982. A Stereochemical Concept for the Catalytic Mechanism of Prolylhydroxylase - Applicability to Classification and Design of Inhibitors. J Theor Biol 94:421-455.

29. Mehn, M. P., K. Fujisawa, E. L. Hegg, and L. Que. 2003. Oxygen activation by nonheme iron(II) complexes: alpha-keto carboxylate versus carboxylate. J Am Chem Soc 125:7828-7842.

30. Zhou, J., M. Gunsior, T. R. Holman, E. G. Pavel, C. A. Townsend, and E. I. Solomon. 1998. Circular dichroism (CD) and magnetic circular dichroism (MCD) spectroscopic studies of mono-nuclear non-heme iron enzymes - Clavaminate synthase (CS2) and lipoxygenase (LO) mutants: Correlation to mechanisms & functions. Abstr Pap Am Chem S 216:U143-U143.

31. Cosper, N. J., C. M. V. Stalhandske, R. E. Saari, R. P. Hausinger, and R. A. Scott. 1999. X-ray absorption spectroscopic analysis of Fe(II) and Cu(II) forms of a herbicide-degrading alpha-ketoglutarate dioxygenase. J Biol Inorg Chem 4:122-129.

32. Puistola, U., T. M. Turpeenniemihujanen, R. Myllyla, and K. I. Kivirikko. 1980. Studies on the Lysyl Hydroxylase Reaction .1. Initial Velocity Kinetics and Related Aspects. Biochim Biophys Acta 611:40-50.

33. Holme, E., S. Lindstedt, and I. Nordin. 1982. Uncoupling in the Gamma Butyrobetaine Hydroxylase Reaction by D-Carnitine and L-Carnitine. Biochem Bioph Res Co 107:518-524.

34. Grzyska, P. K., R. P. Hausinger, and D. A. Proshlyakov. 2010. Metal and substrate binding to an Fe(II) dioxygenase resolved by UV spectroscopy with global regression analysis. Anal Biochem 399:64-71.

35. Grzyska, P. K., E. H. Appelman, R. P. Hausinger, and D. A. Proshlyakov. 2010. Insight into the mechanism of an iron dioxygenase by resolution of steps following the Fe-IV=O species. P Natl Acad Sci USA 107:3982-3987.

36. Grzyska, P. K., R. P. Hausinger, and D. A. Proshlyakov. 2009. Resolution of substrate oxygenation steps in a nonheme Fe(II) enzyme. Abstr Pap Am Chem S 238:802-802.

37. Grzyska, P. K., M. J. Ryle, G. R. Monterosso, J. Liu, D. P. Ballou, and R. P. Hausinger. 2005. Steady-state and transient kinetic analyses of taurine/alpha-ketoglutarate dioxygenase: Effects of oxygen concentration, alternative sulfonates, and active-site variants on the fe(IV)-oxo intermediate. Biochemistry-Us 44:3845-3855.

38. Solomon, E. I., T. C. Brunold, M. I. Davis, J. N. Kemsley, S. K. Lee, N. Lehnert, F. Neese, A. J. Skulan, Y. S. Yang, and J. Zhou. 2000. Geometric and electronic structure/function correlations in non-heme iron enzymes. Chem. Rev. 100:235-349.

39. Solomon, E. I., A. Decker, and N. Lehnert. 2003. Non-heme iron enzymes: Contrasts to heme catalysis. P Natl Acad Sci USA 100:3589-3594.

40. Price, J. C., E. W. Barr, B. Tirupati, J. M. Bollinger, and C. Krebs. 2003. The first direct characterization of a high-valent iron intermediate in the reaction of an alpha-ketoglutarate-dependent dioxygenase: A high-spin Fe(IV) complex in taurine/alpha-ketoglutarate dioxygenase (TauD) from Escherichia coli. Biochemistry-Us 42:7497-7508.

41. Hoffart, L. M., E. W. Barr, R. B. Guyer, J. M. Bollinger, and C. Krebs. 2006. Direct spectroscopic detection of a C-H-cleaving high-spin Fe(IV) complex in a prolyl-4-hydroxylase. P Natl Acad Sci USA 103:14738-14743.

42. Decker, A., and E. I. Solomon. 2004. Oxygen intermediates in mononuclear non-heme iron sites: Electronic structure and reactivity. Abstr Pap Am Chem S 227:U1510-U1510.

43. Davis, M. I., A. M. Orville, F. Neese, J. M. Zaleski, J. D. Lipscomb, and E. I. Solomon. 1999. Spectroscopic and theoretical studies of substrate binding to the non-heme iron active site of protocatechuate 3,4-dioxygenase. J Inorg Biochem 74:109-109.

44. Neese, F., and E. I. Solomon. 1999. Electronic structure contributions to reactivity in mononuclear non-heme ferric enzymes. Spectroscopic and theoretical studies. J Inorg Biochem 74:247-247.

45. Ye, S. F., J. C. Price, E. W. Barr, M. T. Green, J. M. Bollinger, C. Krebs, and F. Neese. 2010. Cryoreduction of the NO-Adduct of Taurine:alpha-Ketoglutarate Dioxygenase (TauD) Yields an Elusive {FeNO}(8) Species. J Am Chem Soc 132:4739-4751.

46. Ye, S. F., and F. Neese. 2009. Quantum chemical studies of C-H activation reactions by high-valent nonheme iron centers. Curr Opin Chem Biol 13:89-98.

47. Tierney, D. L., P. E. Doan, H. Huang, P. Martasek, B. S. S. Masters, R. B. Silverman, and B. M. Hoffman. 1999. ENDOR spectroscopic determination of the position and structure of enzyme-bound substrates: holo-nitric oxide synthase. J Inorg Biochem 74:32-32.

48. Arciero, D. M., A. M. Orville, and J. D. Lipscomb. 1985. [O-17]Water and Nitric-Oxide Binding by Protocatechuate 4,5-Dioxygenase and Catechol 2,3-Dioxygenase - Evidence for Binding of Exogenous Ligands to the Active-Site Fe-2+ of Extradiol Dioxygenases. J Biol Chem 260:4035-4044.

49. Hegg, E. L., A. K. Whiting, R. E. Saari, J. McCracken, R. P. Hausinger, and L. Que. 1999. Herbicide-degrading alpha-keto acid-dependent enzyme TfdA: Metal coordination environment and mechanistic insights. Biochemistry-Us 38:16714-16726.

CHAPTER 2

ELECTRON PARAMAGNETIC RESONANCE FOR STUDYING IRON NITROSYL ENZYME COMPLEXES

INTRODUCTION

The mechanisms for enzyme mediated catalysis often involve a transition metal ion coordinated by the appropriate ligands and substrates in the proper orientation that is essential to the desired reactivity **(1, 2)**. In structural studies of enzymes the unique electronic properties of transition metals offer a spectroscopic probe for observation of the ligand and substrate binding **(3)**. Electron Paramagnetic Resonance (EPR) spectroscopy can give access to both structural and electronic structure information for transition metal centered enzyme complexes that have at least one unpaired electron **(4)**. With this combination of information arising from a single technique, insight into the structure-function relationships is accessible. Many paramagnetic complexes exist naturally in functioning enzymes but some of them do not have the electronic structure necessary to allow for robust EPR analysis **(5-7)**. In non-heme Fe(II) dependent enzymes the protein ligated Fe(II) (either low spin S=0 or high spin S=2) and Fe(II)-O_2 (S=1) complexes are EPR silent. Preparation of a Fe(II)-NO complex that has an effective spin of S=3/2 provides the paramagnetic probe necessary for EPR spectroscopy that also closely mimics the structural aspects of the functioning Fe(II)-O_2 complex **(3, 7, 8)**. This chapter presents the electronic properties of the Fe(II)-NO complex in non-heme Fe(II)/α-KG dependent hydroxylases and points out its effectiveness to facilitate EPR analysis. Important EPR techniques that are used in enzyme structural studies will also be introduced.

2.1 FE(II)-NO AS A SPECTROSCOPIC PROBE

Using the notation introduced by Enmark and Feltham **(3)**, the $\{FeNO\}^7$ complex shares 7 electrons between the Fe d orbitals and the NO valence shell resulting in a S=3/2 spin system. Brown et al. **(9)** first proposed that the interaction is best modeled as a S=5/2 Fe(III) antiferromagnetically coupled to a S=1 NO^-. Figure 2.1 illustrates a basic molecular orbital (MO) diagram for the Fe-NO coupling.

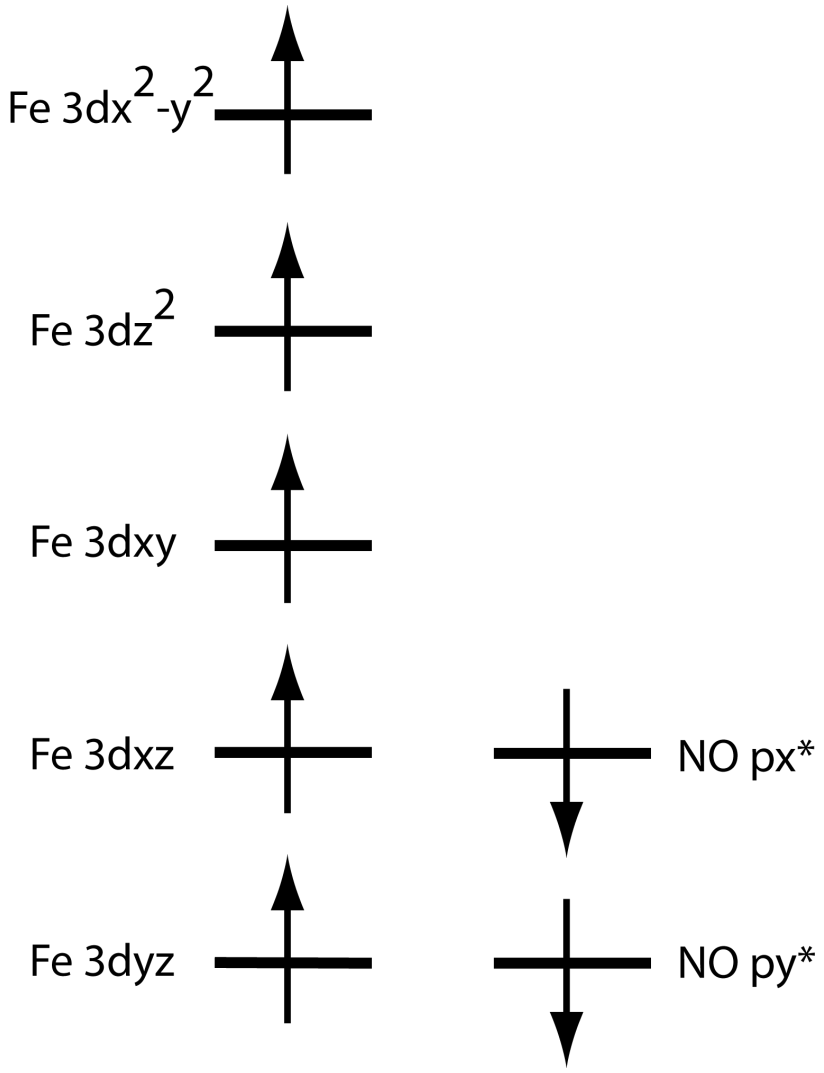

Figure 2.1 Two unpaired electron spins in π antibonding orbitals of NO are antiferromagnetically coupled to two unpaired spins in the Fe $3d_{xz}$ and $3d_{yz}$ orbitals. The Fe $3d_{xy}$, $3d_{x^2-y^2}$, and $3d_{z^2}$ contain the remaining three unpaired electrons.

This picture has been corroborated by Ye et al. in a study where computational methods were used to energetically characterize various spin coupling schemes and visualize the distribution of unpaired spin across a $\{FeNO\}^7$ complex that was prepared in the non-heme Fe(II)/α-KG dependent hydroxylase TauD **(8)**. With Density Functional Theory (DFT) calculations, the most energetically favorable binding motif was confirmed as having 5 electrons in singly occupied Fe 3d orbitals and 2 unpaired electrons in NO π* orbitals. Large spacial overlaps with two Fe based orbitals (d_{xz} and d_{yz}) suggest a partially covalent nature of the antiferromagnetic coupling. The remaining Fe 3d orbitals (d_{xy}, $d_{x^2-y^2}$, and d_{z^2}) contain one unpaired spin each. The isomer shifts in the Mössbauer spectra for TauD samples showed isomer shifts characteristic with high spin Fe(III) lending support to the electronic structure picture predicted by theory. Ye references the previous study by Brown and coworkers **(9)** where XAS, resonance Raman, and MCD were used to experimentally characterize the $\{FeNO\}^7$ complex. Spectroscopic results were interpreted as showing a spin pairing scheme that was between high spin Fe^{2+} antiferromagnetically coupled to NO and high spin Fe^{3+} antiferromagnetically coupled to NO^-. The conclusion was made that Fe^{3+} antiferromagnetically coupled to NO^- is the most likely of the possible spin pairings.

In transition metal ions with multiple unpaired electron spins, a large zero field splitting (ZFS) arises from the coupling of spin and orbital angular momenta. For the $\{FeNO\}^7$ complex, multiple studies have measured the magnitude of the ZFS as ~10-20 cm^{-1} **(3, 8, 9)**. The ZFS can be characterized using the Hamiltonian expression given in Equation 2.1:

$$\hat{\mathrm{H}}_{ZFS} = D(\hat{S}_z^2 - \frac{1}{3}\hat{S}^2) + E(S_x^2 - S_y^2) \qquad \textbf{[2.1]}$$

The largest component of the ZFS tensor (*D*) defines the principal axis (z). The spin operators $\hat{S}_z$, $\hat{S}_x$ and $\hat{S}_y$ describe the projection of the spin angular momentum in the z, x and y directions respectively, and $\hat{S}$ is the overall spin operator. While the largest component of the ZFS (*D*) is quantized along z the degree of deviation from axial symmetry is described by the magnitude of the rhombic term (*E)*. See Appendix A for a derivation of Equation 2.1.

The DFT modeling in the aforementioned study **(8)** also suggests that the unpaired spins are delocalized over the Fe-NO moiety. A separate study by Aquino, F. and Rodriguez, J. **(10)** used spin density functional theory and perturbation theory (SDFT-PT) methodology to calculate the ZFS parameters for a model S=3/2 $\{FeNO\}^7$ system. Like the previous studies, the calculations suggested a significant contribution from NO p_x* and p_y* orbitals to MOs involved in the Fe-N(O) bond. The suggestion was made that the principal component of the ZFS is strongly correlated to the Fe-N(O) bond direction. Their study concluded that the angle between the principal component of the ZFS and the Fe-N(O) bond was only 4.8˚ allowing the principal component of the ZFS to be considered as the Fe-N(O) bond direction. Ye and coworkers used computational methods to optimize the orientation of NO in the TauD enzyme complex **(8)**. Figure 2.2 is taken from the paper by Ye et al. **(8)** that describes this study and shows two relative projections of NO in the TauD complex along with their relative calculated energies.

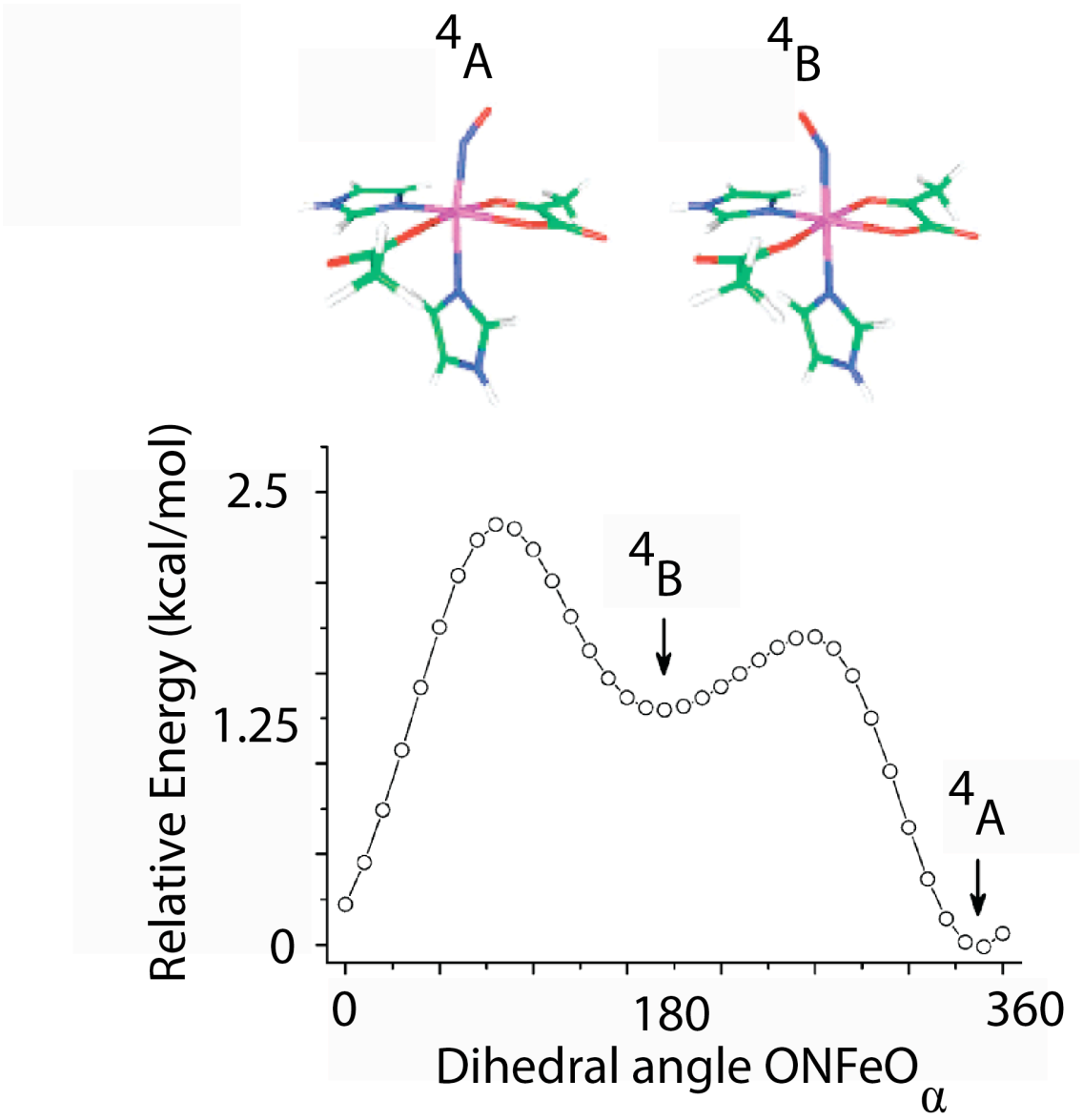

Ye et al., J. Am. Chem. Soc., Vol. 132, No. 13, 2010

Figure 2.2 ^{4}A and ^{4}B represent two different relative projections of the N=O bond onto the coordination plane containing α-KG, Asp, and the equatorial His. The relative energies of the two projections are clearly distinguished. The ^{4}A orientation has the O projected over the α-KG where the ^{4}B orientation has the O projected over the carboxylate group of the Asp ligand **(8)**. (For interpretation of the references to color in this and all other figures, the reader is referred to the electronic version of this thesis.)

Simply changing the relative projection of the N=O bond over the plane perpendicular to the binding of NO results in clearly distinguished calculated potential energy minima.

For non-heme Fe(II)/α-KG dependent hydroxylases where there are "in line" and "off line" α-KG binding modes, the different open coordination sites for NO in the resting Fe(II) complex for each binding mode would make available not only different projections of NO in the complex but entirely different binding modes for NO **(11)** that would give distinctly different ZFS parameters. Calculated and spectroscopically measured *E* values can then be used to distinguish between the different binding modes of NO and provide insight into the relative ligand arrangements of the "in line" and "off line" α-KG binding modes. However, as pointed out by Ye **(8)**, when the ZFS is this large, calculated values of *E* are subject to error. The non zero *E* arises from changes in the smallest components of the ZFS tensor that are only small perturbations on the principal component. Although line broadenings and sometimes splittings from non zero *E* are visible in Mössbauer spectra, determination of the magnitude of *E* from simulation of the data is equally prone to error for the same reasons. Because of this, the ratio of *E/D* is more often used to describe the relative deviation from axiality without knowing the exact values of *E* or *D*. Determination of finite details from absolute magnitudes of *E/D*, however, is admittedly unreliable.

For the $\{FeNO\}^7$ complex, if different orientations of NO result in different ZFS parameters, the different orientations would also produce characteristic line broadenings or splittings in CW EPR spectra **(9, 12)**. Values of the ratio of *E/D* can be determined by simulation of spectra and information on the orientation of the NO ligand can be ascertained by comparison with theoretical predictions. Because of the range of specific EPR techniques that are each

complementary in structural studies **(5, 7)**, the direct correlation of the *E/D* measurements to structural measurements is possible. The following sections will discuss the use of EPR to correlate structure and function for $\{FeNO\}^7$ enzyme complexes.

2.2 CONTINUOUS WAVE EPR OF FE(II)-NO

The interaction of the unpaired spins in the $\{FeNO\}^7$ complex with microwave radiation in an external applied magnetic field can first be visualized with a simple energy level diagram. Figure 2.3 illustrates the electron spin states as a function of an externally applied magnetic field.

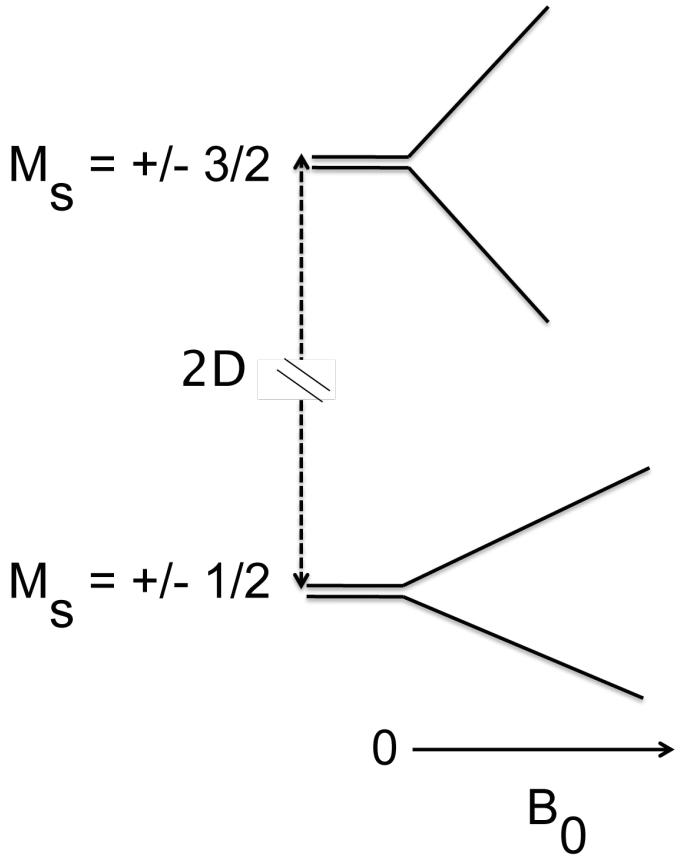

Figure 2.3 The Kramer's doublets are separated by twice the magnitude of the ZFS in the absence of a B_0 field. When the B_0 field is turned on the individual spin states become non degenerate and separate in energy linearly as a function of field strength.

The M_S=+/-1/2 and M_S=+/-3/2 Kramers doublets are separated by twice the magnitude of the ZFS (2*D*) before application of an external magnetic field **(9, 10)**. To record an EPR spectrum a sample is continuously irradiated with a fixed microwave frequency while the strength of an externally applied magnetic field is varied. EPR transitions are observed when resonant absorption of the microwaves causes transitions between spin states. The $\{FeNO\}^7$ complex **(3)** has an EPR spectrum characteristic of this S=3/2 spin system with *D* much larger than X-Band energies (> 0.3 cm^{-1}) **(4)**. Figure 2.4 illustrates a typical EPR spectrum for a $\{FeNO\}^7$ complex with purely axial ZFS (*E/D*=0) at liquid helium temperatures (T=4 K).

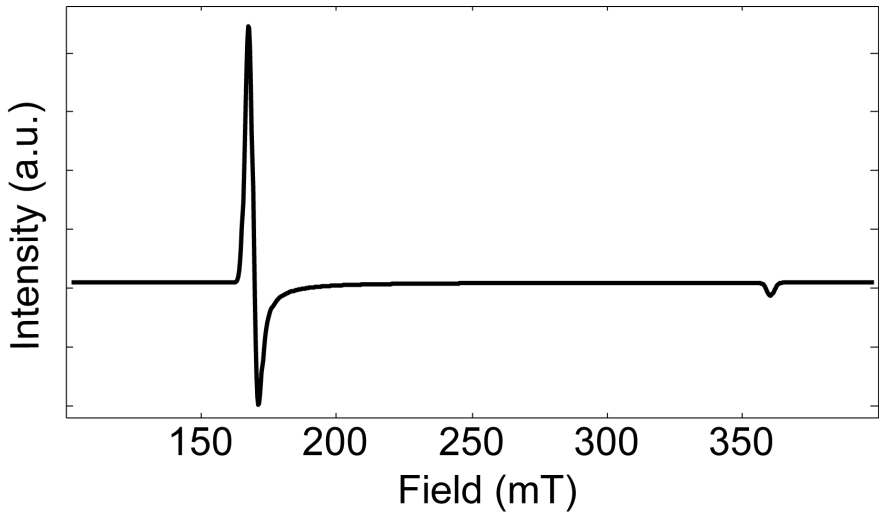

Figure 2.4 The EPR spectrum for frozen (T=4 K) samples of $\{FeNO\}^7$ complexes are characteristic of an S=3/2 spin system with large, axial, ZFS.

The highly anisotropic spectrum with principal effective g values of $g_{\perp} \approx 4$ and $g_{\parallel} \approx 2$ can be calculated by solving for the eigenvalues of the Hamiltonian matrix that was built using Equation 2.3. (See Appendix A for calculating eigenvalues from Equation 2.3.) Equation 2.3 has the form:

$$\hat{\mathrm{H}}_{EPR} = \hat{\mathrm{H}}_{ZFS} + g\beta \underset{\sim}{B}_0 \bullet \underset{\sim}{\hat{S}} \qquad \textbf{[2.3]}$$

The $\hat{\mathrm{H}}_{ZFS}$ is described in Equation 2.1 defines the principal magnetic axes of the spin system because D is much larger (~10-20cm^{-1}) than the energies used in X-Band EPR (~0.3 cm^{-1}). The second term is the electron Zeeman term that describes the interaction of the unpaired electron spins with the magnetic field vector (B_0). In the Zeeman term, the remaining constants are the electron g factor, the Bohr magneton (β_e), and the spin vector operator ($\hat{\mathrm{S}}$). B_0 and $\hat{\mathrm{S}}$ are expressed as vectors so that their projection in the principal axis system can be described. For S=1/2 paramagnetic centers the g factor can also be expressed as a tensor that couples the spin magnetic moment to the B_0 vector. For these systems, the effects of spin-orbit coupling are reflected in the g tensor but for EPR of transition metal ions with S >1/2 the contribution from spin-orbit coupling is folded into the ZFS Hamiltonian and the electron Zeeman term describes the "spin only" part of the electrons' angular momenta. The concept of an "effective g value" associated with each magnetic field position in an EPR spectrum is instead used to describe the orientations of B_0 with respect to the principal axes of the ZFS that are being observed at a specific field value **(13)**. The effective g value can be calculated as a simple proportionality constant with Equation 2.4.

$$g = \frac{h\nu}{\beta B_0} \qquad \textbf{[2.4]}$$

where *h* is Planck's constant and ν is the microwave frequency. The orientation of the principal axis of the spin system to the B_0 vector that corresponds to each effective g value (g_{eff}) can be calculated with Equation 2.5.

$$g_{eff}^2 = \sqrt{g_{\|}^2 \cos^2\theta + g_{\perp}^2 \sin^2\theta} \qquad \textbf{[2.5]}$$

The angle θ describes the relation of the principal component of the ZFS tensor to the direction of the external magnetic field, $g_{\|}$ is the value of g that corresponds to alignment of the principal axis of the ZFS tensor with the B_0 vector, and $g_{\perp}$ is the value of g that corresponds to alignment of the perpendicular axes (*x* and *y*) of the ZFS with the B_0 vector. The observation of a broad anisotropic EPR spectrum with absorption spanning from $g_{\perp} \simeq 4$ to $g_{\|} \simeq 2$ is a result of the anisotropy in the ZFS together with the low temperatures used in the experiments (4 K). Any sample containing the $\{FeNO\}^7$ complexes at 4 K will be frozen and all possible orientations of the ZFS tensor with respect to the external magnetic field will be represented in the solid samples. The use of low temperatures is necessary to aid in the observation of the EPR spectrum. A ratio of Boltzman populations can be used to describe the relationship between the difference in spin state populations and the temperature (Equation 2.6).

$$\frac{N_\alpha}{N_\beta} \propto e^{\frac{-\Delta E}{k_B T}}$$

[2.6]

The intensity of the EPR lines is directly proportional to the ratio of the spin population in the α (N_α) spin state to the spin population in the β (N_β) spin state. Because the ratio is inversely proportional to the temperature (T), lowering the temperature will increase the intensity of the EPR lines. The remaining constants are k_B, the Boltzman constant, and ΔE, the separation in energy between the spin states.

For the axial case pictured in Figure 2.4 the large magnitude of the ZFS (~10-20 cm^{-1}) makes the spin states pure M_S=+/-1/2 and M_S=+/-3/2 states. Excitations within the M_S=+/-1/2 manifold are observed but excitations between the Kramers doublets are inaccessible at the energy of X-Band EPR experiments (~0.3 cm^{-1}). When the ZFS deviates from axial symmetry (non zero *E/D*), the rhombic term (*E*) will now contribute to the eigenvalues for operation with the $\hat{S}_x$ and $\hat{S}_y$ spin operators and the $g_\perp = 4$ feature will be broadened or split to an extent that is proportional to the magnitude of *E/D*. Figure 2.5 shows two calculated EPR spectra for a $\{FeNO\}^7$ complex to illustrate the effects of non zero *E/D* on the EPR spectrum.

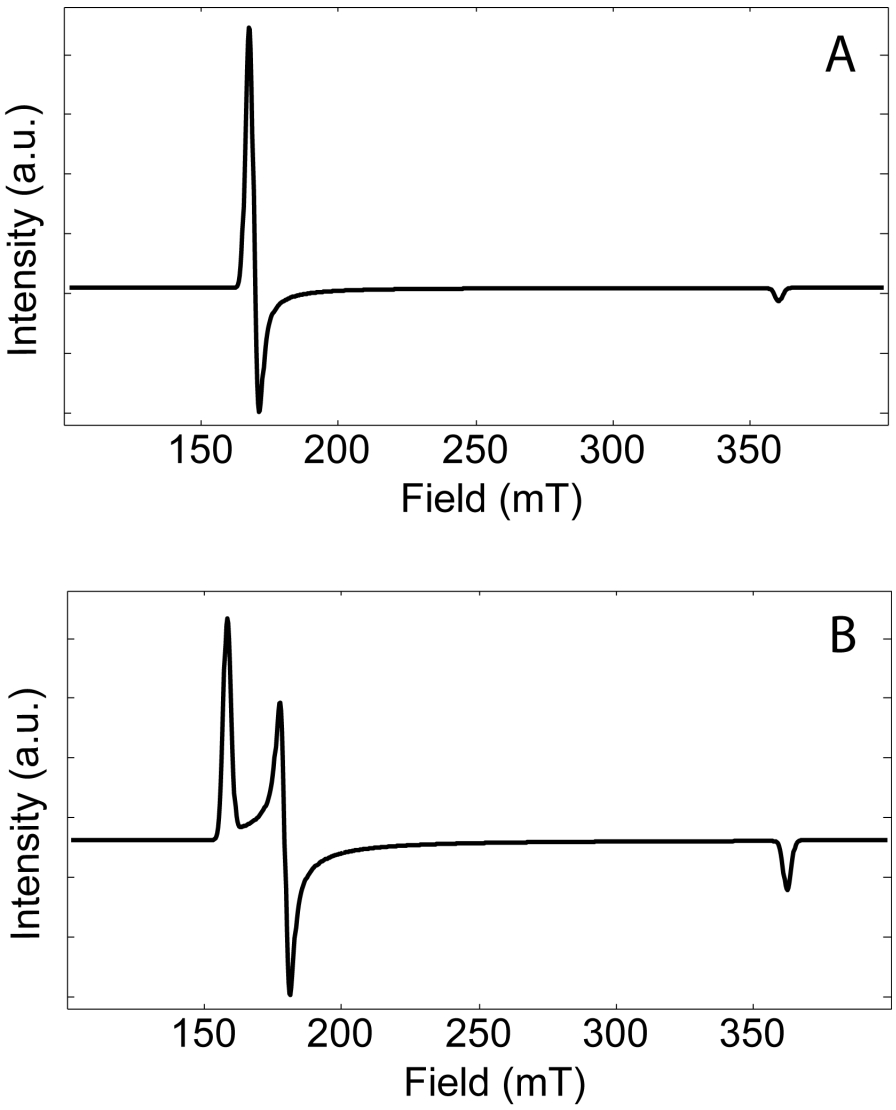

Figure 2.5 (A) EPR spectrum for a purely axial ZFS, D=10 cm^{-1} and E/D=0. **(B)** EPR spectrum for D=10 cm $^{-1}$ and E/D=0.04. Smaller values for E/D can manifest as a simple line broadening.

Simulation of CW EPR spectra can allow for accurate measurement of E/D in most cases but the characterization of the magnitude of $|D|$ is not possible at X-Band. The magnitude of D is usually borrowed from other experimental or theoretical work **(8, 10)**. When interpreting EPR spectra the value of E is usually expressed as a E/D ratio because it can quantify the degree of deviation from axial symmetry without relying on the exact values of E or D.

Because *D* is directed nearly coincident with the Fe-N(O) bond **(10)**, the utility in CW EPR for $\{FeNO\}^7$ complexes lies in measuring the *E/D* ratio to use it for suggesting relative degrees of deviations in NO binding in enzyme complexes. Exact location of the bond, however, is not discernible with CW EPR. Also not visible in CW EPR of these complexes are the spectral effects of interactions with bound or neighboring magnetic nuclei. The inhomogeneously broadened absorption lines mask any hyperfine structure in the EPR spectrum. Pulsed EPR experiments can be used to resolve these interactions and derive Hamiltonian parameters that describe magnetic interactions between the $\{FeNO\}^7$ center and its ligands. This information can be used to suggest the position of the Fe-N(O) bond in the coordination complex or measure the position of key nuclei near the $\{FeNO\}^7$ complex to allow for the direct investigation of structure-function relationships. The following sections will discuss nuclear hyperfine interactions (HFI) and nuclear quadrupole interactions (NQI) and introduce pulsed EPR techniques that can be used to measure the position of specific nuclei coupled to the $\{FeNO\}^7$ paramagnetic center of enzyme complexes.

2.3 ^{2}H NUCLEAR HYPERFINE COUPLINGS AND QUADRUPOLE INTERACTION

Since protons (^{1}H) are often the target of key steps in the non-heme Fe(II) dependent hydroxylation mechanism **(11)**, substitution of a specific ^{1}H with a ^{2}H on the primary substrate is a useful technique in resolving an individual electron-nuclear interaction to visualize the position of that ^{1}H near the spin center **(14)**. The characterization of the interaction of ^{2}H nuclei with unpaired electron spins using EPR can first be predicted with a simple energy level diagram and

three new terms in Hamiltonian expression given in Equation 2.3. Figure 2.6 is an energy level diagram for coupling of an S=1/2 spin system to I=1 nuclei.

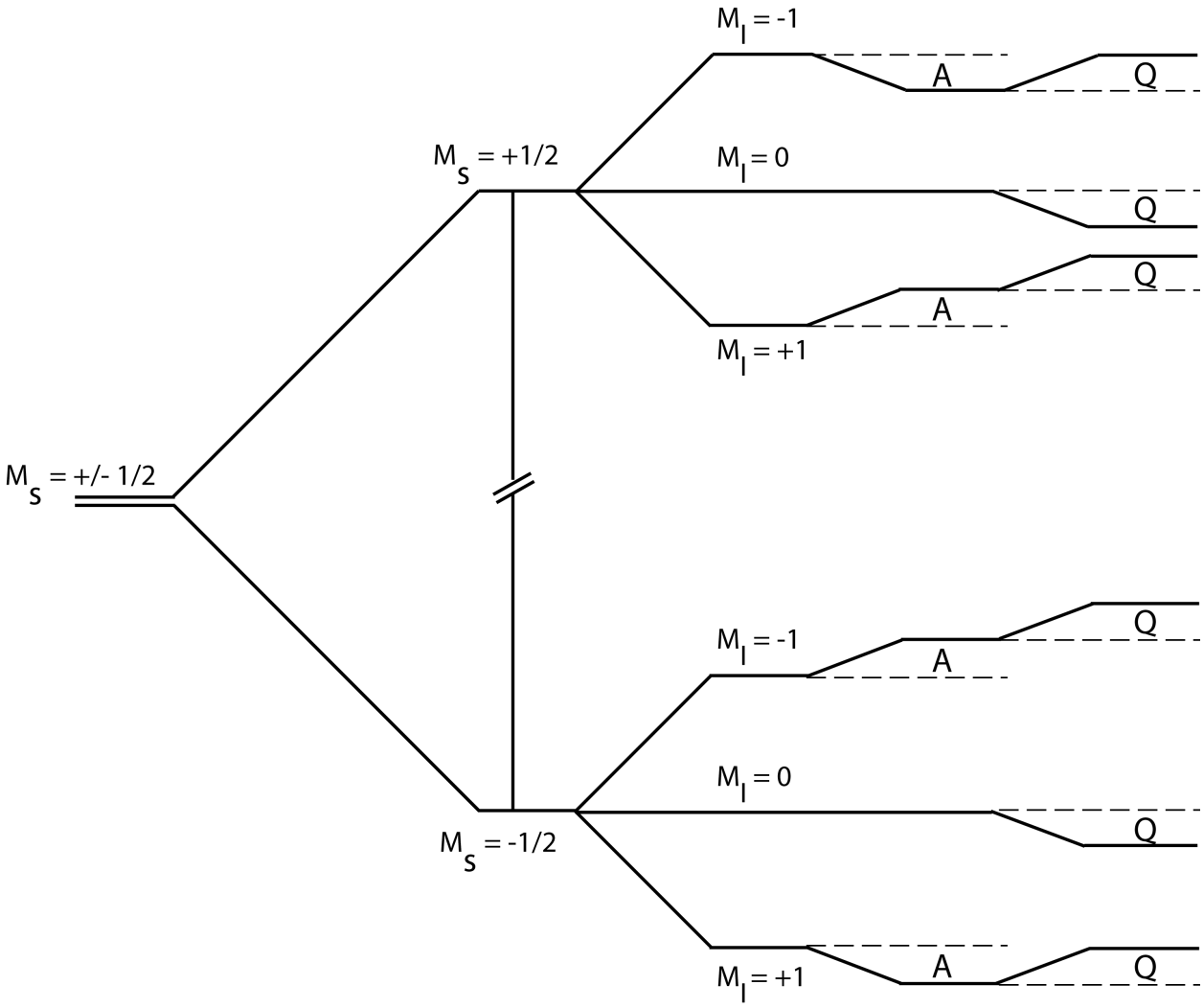

Figure 2.6 The energy level diagram represents a picture of hyperfine and quadrupole effects on spin state energies for one orientation of the spin system resulting from the coupling to I=1 nuclei. The gaps between the solid and dotted lines labeled as "A" are the shifting of the spin state energies by hyperfine couplings. The gaps between the solid and dotted lines labeled as "Q" are the shifting of the spin state energies by interaction with the quadrupole moment and electric field gradient at the coupled nucleus.

The Hamiltonian expression that can be used to calculate the energy of the nuclear spin states is given in Equation 2.7:

$$\hat{\mathrm{H}}_{nuclear} = -g_n \beta_n \underset{\sim}{B}_0 \bullet \underset{\sim}{\hat{I}} + \hat{S} \bullet A \bullet \hat{I} + \hat{I} \bullet Q'' \bullet \hat{I} \qquad \textbf{[2.7]}$$

The first term is the nuclear Zeeman term that accounts for the interaction of the nuclear magnetic moment with the magnetic field. Î is the nuclear spin operator, g_n is the nuclear g value, and β_n is the nuclear magneton. B_0 and Î are expressed as vectors so that their projection in the principal axis system can be defined. The second term accounts for the HFI of the electronic and nuclear magnetic moments. ***A*** is the HFI tensor and is more completely expressed as Equation 2.8:

$$A = R^{-1}(\alpha,\beta,\gamma)\begin{pmatrix} a_{iso} - T(1-\rho) & 0 & 0 \\ 0 & a_{iso} - T(1+\rho) & 0 \\ 0 & 0 & a_{iso} + 2T \end{pmatrix} R(\alpha,\beta,\gamma)$$

[2.8]

The HFI consists of scalar (a_{iso}) and dipolar (T) coupling and is related to the principal axes of the ZFS tensor by the rotation matrix $R_{(\alpha,\beta,\gamma)}$. Any deviation from axial symmetry is described by the ρ term. Equation 2.9 illustrates the form of $R_{(\alpha,\beta,\gamma)}$.

$$R(\alpha,\beta,\gamma) = \begin{pmatrix} \cos\beta\cos\gamma & \cos\alpha\sin\gamma + \sin\alpha\sin\beta\cos\gamma & \sin\alpha\sin\gamma - \cos\alpha\sin\beta\cos\gamma \\ -\cos\beta\sin\gamma & \cos\alpha\cos\gamma - \sin\alpha\sin\beta\sin\gamma & \sin\alpha\cos\gamma + \cos\alpha\sin\beta\sin\gamma \\ \sin\beta & -\sin\alpha\cos\beta & \cos\alpha\cos\beta \end{pmatrix}$$

[2.9]

The final term is necessary for nuclei having a nuclear spin I ≥ 1 and accounts for any shifting of nuclear spin state energies by the nuclear quadrupole moment and electric field gradient at the nucleus. ***Q″*** is the NQI tensor and can be more completely expressed as Equation 2.10:

$$Q'' = R^{-1}(\alpha',\beta',\gamma')\frac{e^2Qq/h}{4I(2I-1)}\begin{pmatrix} -(1-\eta) & 0 & 0 \\ 0 & -(1+\eta) & 0 \\ 0 & 0 & 2 \end{pmatrix}R(\alpha',\beta',\gamma')$$

[2.10]

The NQI is defined by the nuclear quadrupole moment (Q) and the electric field gradient at the nucleus (q). The constant e is the charge of an electron, h is planck's constant, and I is the nuclear spin. Again, a rotation matrix $R_{(\alpha',\beta',\gamma')}$ is used to relate the NQI tensor to the principal axes of the ZFS tensor. Any deviation from axial symmetry is described in this case by the η term.

2.4 ELECTRON SPIN ECHO ENVELOPE MODULATION (ESEEM)

A pulsed EPR technique called Electron Spin Echo Envelope Modulation (ESEEM) **(15)** is useful in resolving weak HFI and NQI when the inhomogeneously broadened absorption lines mask any fine structure in the EPR spectrum **(5, 16)**. The following explanation of the ESEEM experiment is translated from the chapter titled "Electron Spin Echo Envelope Modulation" written by John McCracken in the book "Handbook of Electron Spin Resonance: Volume 2" edited by Charles P. Poole, Jr. and Horacio A. Farach.

In an ESEEM experiment, instead of applying constant microwave (m.w.) irradiation while varying the magnetic field to find EPR transitions (CW EPR), m.w. pulses are applied

while maintaining a constant magnetic field. EPR transitions are resonantly excited and spin relaxation after the pulses are switched off is sensitive to inhomogeneities in the local magnetic field such as those caused by HFI and NQI. To visualize the ESEEM effect, consider a two pulse Hahn Echo sequence ($\pi/2$ - τ - π - τ - echo) applied to a S=1/2 spin system having HFI with I=1/2 nuclei. Figure 2.7 illustrates the Hahn Echo sequence **(17)**, Figure 2.8 illustrates the nuclear spin states resulting from the HFI, and Figure 2.9 offers a spin vector picture to relate Figures 2.7 and 2.8.

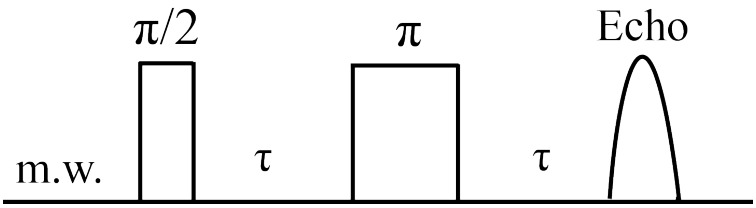

Figure 2.7. Two microwave pulses are applied and the spin echo amplitude is recorded as a function of the time spacing between the pulses (τ).

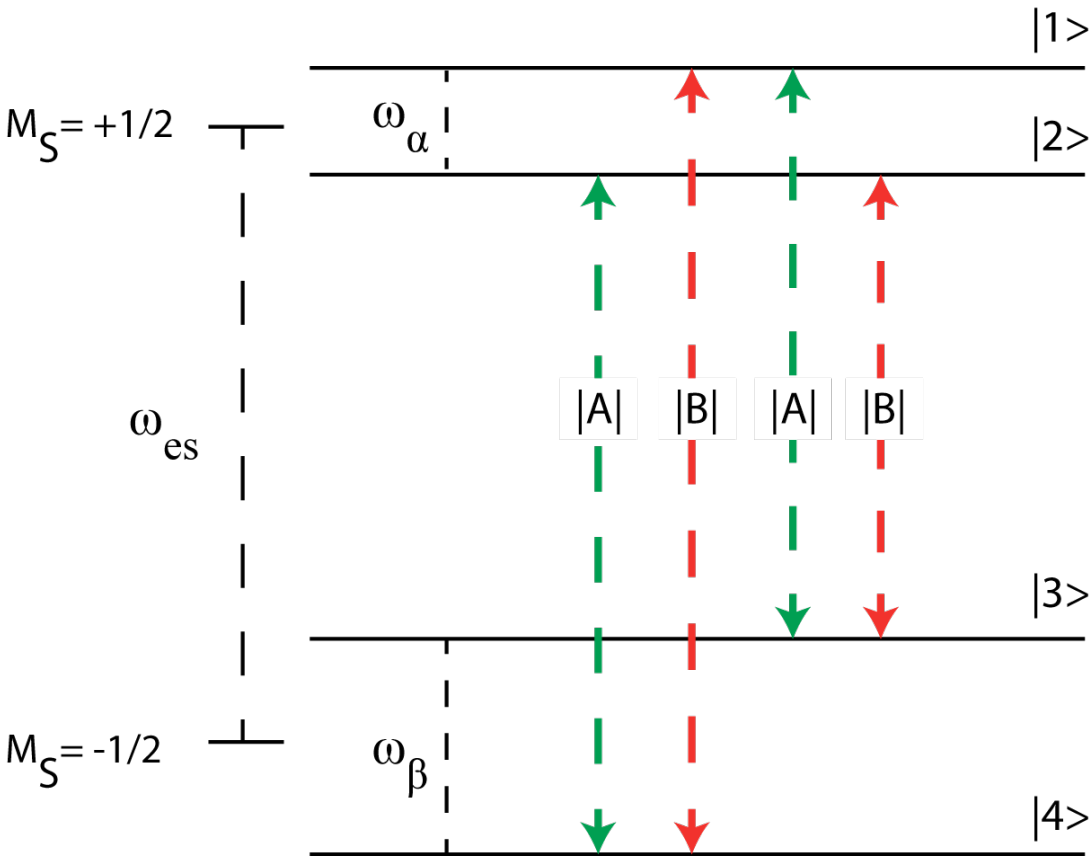

Figure 2.8. The energy level diagram consists of spin states described by the Hamiltonian expression in Equation 2.3. In Figure 2.11, states |1>, |2>, |3>, and |4> can be mixtures of pure M_I +/- 1/2 spin states. Although only four transitions are pictured for ease of visualization, it is important to note that a multitude of spin states exist and many transition pathways are available.

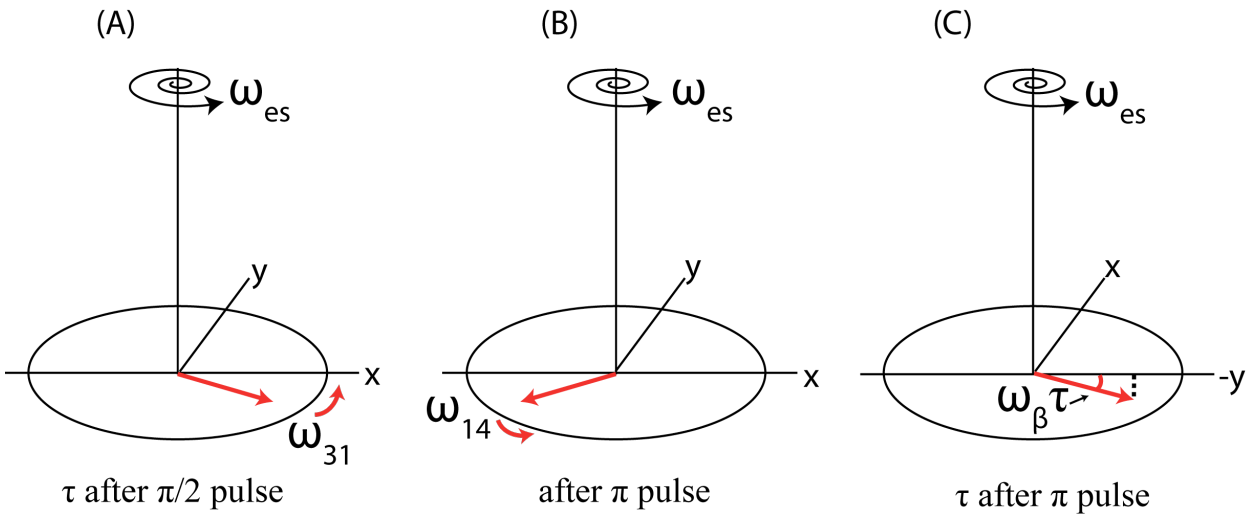

Figure 2.9. The red arrow is the net magnetization vector of the spin population that was excited from state |3> to state |1> by the π/2 pulse and state |1> to state |4> by the π pulse.

In a rotating frame (Figure 2.9) defined by the microwave frequency (ω_{es}), the resonant m.w. pulses excite all four of the transitions pictured in Figure 2.8. The first, π/2, pulse torques the spin magnetization vectors through 90˚ placing the vectors in the *x* and *y* plane. During the free precession time (τ) following the first pulse, the spin vectors begin to fan out in the x and y plane. The population of spins that are excited from state |3> to state |1>, for example, will precess at a frequency (ω_{31}) corresponding to the transition from state |3> to state |1>. Because this frequency is smaller than ω_{es}, this population of spins will fall behind the rotating frame (Figure 3.12A) developing a phase angle [(ω_{31} - ω_{es})τ] to the x axis. The second, π, pulse torques the spin vectors 180˚ about the *y* axis so that the vectors are now precessing in the opposite sense. Of the spins that were precessing at ω_{31}, a sub population will be driven by the π pulse from state |1> to state |4> instead of back to state |3>. This sub population that "branched" to a new transition will now precess at ω_{14} which is larger than ω_{es} and begin to catch up to the

rotating frame. At time τ these branching spins will be a projection onto the detection axis, $\cos[(\omega_{31}-\omega_{14})\tau]$, and interfere with the formation of the spin echo. If τ is steadily increased, interference with the echo formation will occur at the frequency difference $|\ \omega_{31}-\omega_{14}\ |=\omega\beta$ that gave rise to the phase angle $(\omega\beta)\tau$ (Figure 3.12C). While only one transition is discussed, all possible transitions and branching scenarios take place so that the echo will be modulated at $\omega\beta$ and ω_α. The amplitude of the echo plotted as a function of τ for the transitions pictured in Figure 2.11 can be calculated using Equation 2.11:

$$E_{mod}(\tau)= |A|^4 +|B|^4 +|A|^2|B|^2[2\cos\omega_\alpha\tau\ + 2\cos\omega\beta\tau - \cos(\omega_\alpha - \omega\beta)\tau - \cos(\omega_\alpha + \omega\beta)\tau] \quad \textbf{[2.11]}$$

where $|A|^4$ and $|B|^4$ are the square of the transition probabilities for the "non branching" spins and $|A|^2|B|^2$ is the product of the transition probabilities for the "branching" spins. The amplitude will be modulated at ω_α and $\omega\beta$ as well as the two combination frequencies $(\omega_\alpha - \omega\beta)$ and $(\omega_\alpha + \omega\beta)$. In order for the ESEEM to be observed, there must be sufficient probability that all transitions are possible so "branching" can occur. This can be the case when either or both: 1) the HFIs are weak, and 2) anisotropy in the HFI sufficiently mixes the nuclear spin states. Using the Hahn Echo sequence **(17)**, not only are there sum and difference frequencies in the spectra but, if there are multiple coupled nuclei, the E_{mod} is a product of all frequencies at once. Also, superimposed on the E_{mod} in Equation 2.10 is an exponential decay function owed to spin relaxation processes. Electron spin-spin relaxation effects govern the rate of decay and their relatively short time scale hinder frequency resolution. To alleviate some of these issues, the

ESEEM experiment can instead be performed with three π/2 pulses. Figure 2.10 shows a sequence for the 3 pulse version of the ESEEM experiment.

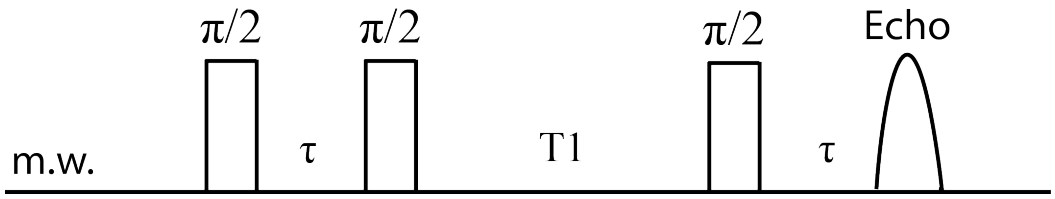

Figure 2.10 Three π/2 microwave pulses are applied and the spin echo amplitude is recorded as a function of the time spacing (T1). The echo amplitude is modulated at the hyperfine frequencies. The utility in 3 pulse ESEEM is the longer relaxation times afforded by dependence on spin-lattice relaxation (T_1) and that the time spacing τ can be tuned to suppress the Larmor frequencies owed to certain nuclei that may interfere with the modulations of interest.

The echo amplitude is recorded as a function of T1 and τ is held constant. The τ can be cleverly chosen as a "suppression τ" that will minimize the unwanted contribution of specific nuclei to the ESEEM spectrum. Also, the decay function for the 3 pulse sequence is governed by electron spin-lattice relaxation, electron cross relaxation, and nuclear spin-spin relaxation. The time scale for these relaxation effects are typically much longer than electron spin-spin relaxation and allow for recording of a longer range of T1 values resulting in increased frequency resolution. Figure 2.11 shows an example of an ESEEM time trace and the corresponding Fourier transformation to the frequency domain for the coupling of an S=1/2 spin system to I=1/2 nuclei.

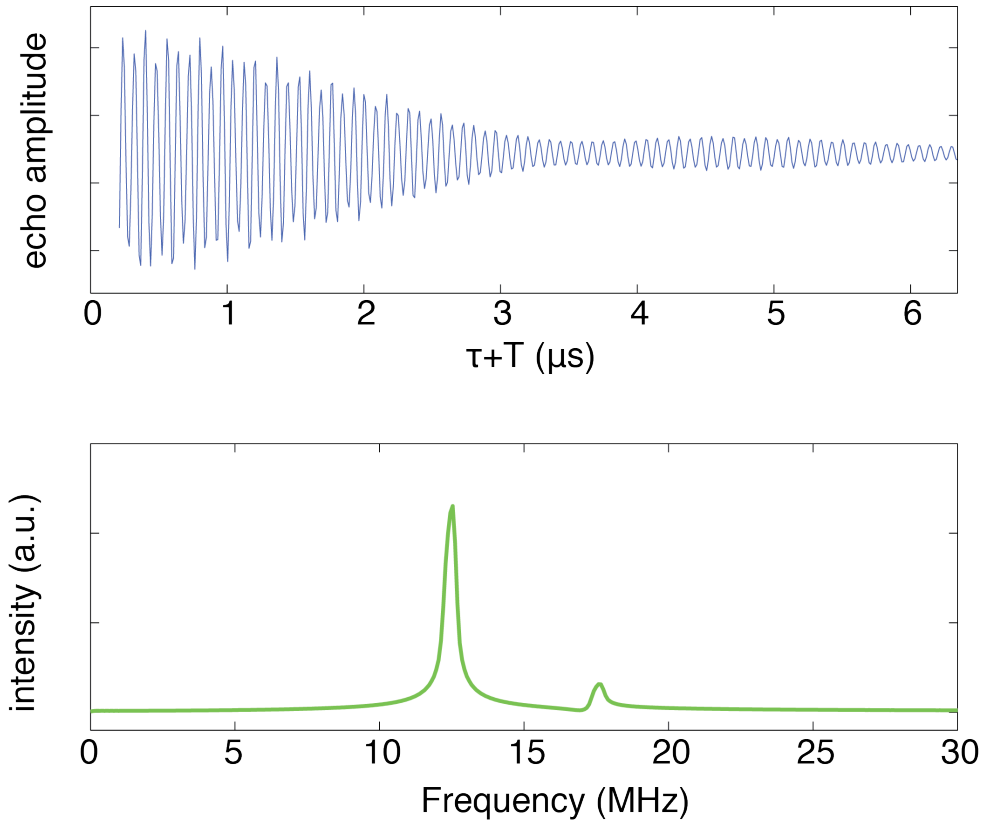

Figure 2.11 3 pulse ESEEM time domain and frequency spectrum for the S=1/2 spin system coupled to a proton with a_{iso}= 5 MHz and T= 0.25 MHz.

ESEEM frequency spectra are a map of frequencies corresponding to the differences in nuclear spin state energies that arise from HFI and NQI. Now that the origin of ESEEM has been presented, Figure 2.14 displays idealized 3 pulse ESEEM spectra for the coupling of an S=1/2 spin system with I=1 ^{2}H nuclei (Figure 2.6 and Equation 2.6) to illustrate how the variables in Equations 2.8 and 2.10 are reflected in the line shapes.

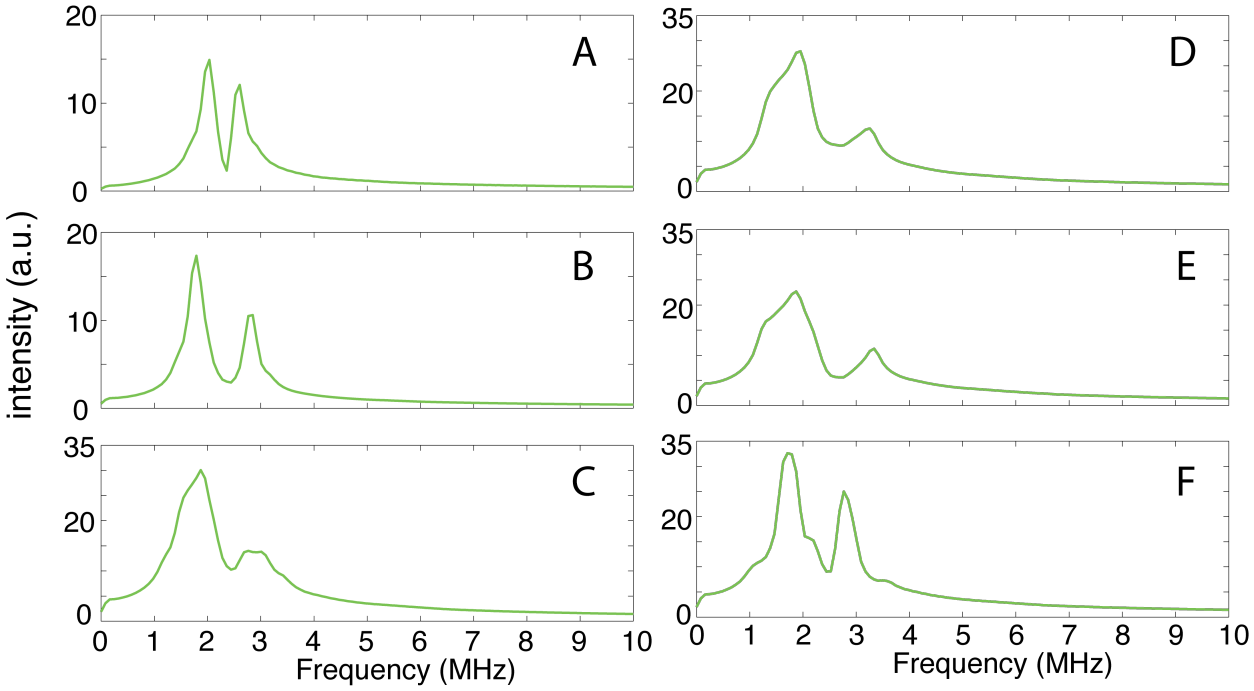

Figure 2.12 Each spectrum represents the modification of a single parameter from Equations 2.8 and 2.10. (A-B) represents an increase in a_{iso} from 0.5 MHz to 1.0 MHz, (B-C) a change in T from 0.25 MHZ to 0.5 MHz, (C-D) a change in β_{HF} from 0 to 1.04 rad, (D-E)a change in e^2qQ/h from 0.2 MHz to 0.4 MHz, (E-F) a change in β_{NQI} from 0 to 1.04 rad. The line shapes and amplitudes are important in describing the isotropic coupling, dipolar distance, and tensor orientations for the spin coupling.

2.5 ^{2}H ESEEM RESOLVED IN RATIO SPECTRA

In $\{FeNO\}^7$ enzyme complexes a multitude of magnetic nuclei are interacting with the unpaired electron spins and will each have a unique interaction that will contribute to ESEEM **(5, 16)**. The ESEEM time trace will be a product of all the hyperfine frequencies. To study the interaction with any individual nucleus, multiple enzyme samples can be prepared differing only by isotopic substitution of a nucleus of interest and the ratio of time domain ESEEM spectra for each sample can be taken to isolate the modulations from one individual interaction. A substituted ^{2}H nucleus can be resolved by collecting ESEEM for samples that differ only by a specific ^{2}H and taking the

ratio of the individual time traces **(14)**. Modulations from protons and nitrogens are filtered out in the division and, without a counterpart in one of the time traces, the ^{2}H modulations are left behind. Fourier transform of the ratio gives a frequency peak centered at the ^{2}H Larmor frequency. This procedure will be applied in chapters 3 and 4. From this information, using Equations 2.8 and 2.10 in simulations of the data can reveal dipolar distances and tensor orientations that will be used to draw structural conclusions.

For $\{FeNO\}^{7}$ enzyme complexes, significant anisotropy in the ZFS broadens the EPR spectrum **(9)**. A single ESEEM experiment at one magnetic field strength does not excite all possible spin transitions. The observation of the interaction of the unpaired electrons with nuclei is limited to a subset of orientations of the ZFS tensor in each experiment **(18)** (see Equation 2.5). Simultaneous analysis of ESEEM data collected at multiple field positions spanning the EPR spectrum is necessary to reconstruct the full energy profile of the spin states.

2.6 HYPERFINE SUBLEVEL CORRELATION (HYSCORE) TO STUDY PROTONS

While isotopic labeling and ratios of ESEEM spectra can provide the resolution of specific hyperfine interactions in $\{FeNO\}^{7}$ enzyme complexes **(14)**, the multitude of protons in real enzymes represent a wealth of information that is lost in the ratio spectra **(5)**. Figure 2.14 shows an energy level diagram for HFI of a S=1/2 spin system with I=1/2 nuclei.

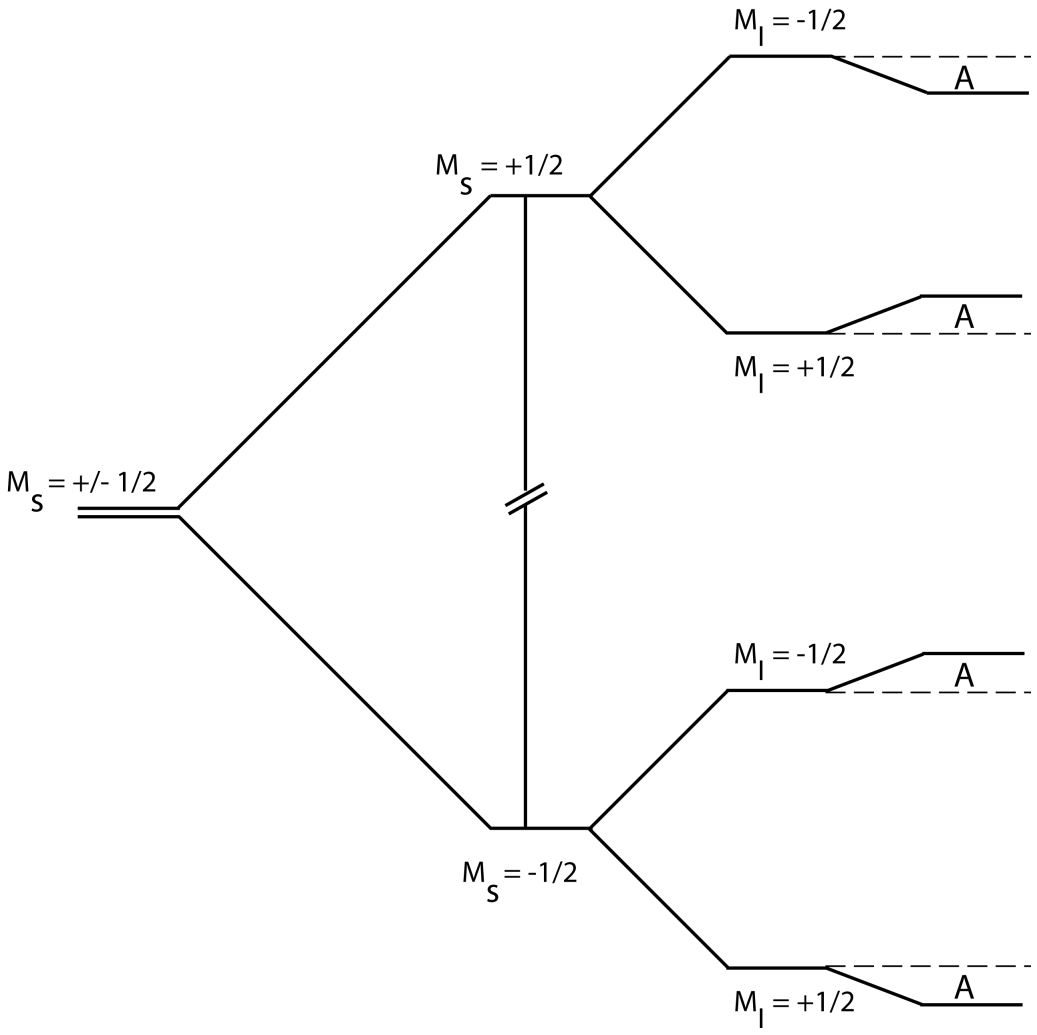

Figure 2.13 The energy level diagram represents a picture of spin state energies for one orientation of the spin system resulting from the coupling to I=1/2 nuclei. The difference between the solid and dotted lines labeled as "A" are the shifting of the spin state energies by HFI.

The Hamiltonian expression in Equation 2.7 is condensed to only the nuclear Zeeman and HFI terms since protons are I=1/2 and don't have a quadrupole moment. The following introduction to the HYSCORE experiment is also translated from the chapter titled "Electron Spin Echo Envelope Modulation" written by John McCracken in the book "Handbook of Electron Spin Resonance: Volume 2" edited by Charles P. Poole, Jr. And Horacio A. Farach.

Figure 2.14 shows a 4 pulse HYSCORE sequence.

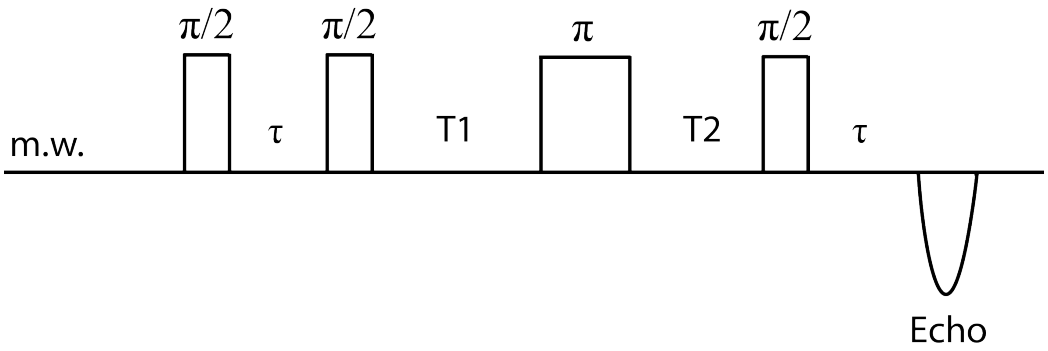

Figure 2.14 The HYSCORE pulse sequence inserts an extra π pulse between the second and third π/2 pulses. Recording the spin echo as a function of time spacings T1 and T2 simultaneously results in a two dimensional array that can be Fourier transformed to give a two dimensional frequency spectrum in which cross peaks are correlations of the same nuclear coupling between the α and β spin manifolds.

With the addition of the π pulse between the second and third π/2 pulses in the 3 pulse ESEEM sequence, coherences between the α and β spin manifolds are created such that populations of spins are encoded with frequencies corresponding to both spin manifolds at the same time. A symmetric two dimensional array of ESEEM as a function of T1 and T2 can be constructed in which cross peaks in a contour plot of the frequency amplitudes represent correlations between hyperfine frequencies in different electron spin manifolds that are owed to the same nuclear coupling. Figure 2.15 illustrates a simple HYSCORE spectrum for the S=1/2 and I=1/2 spin system discussed earlier.

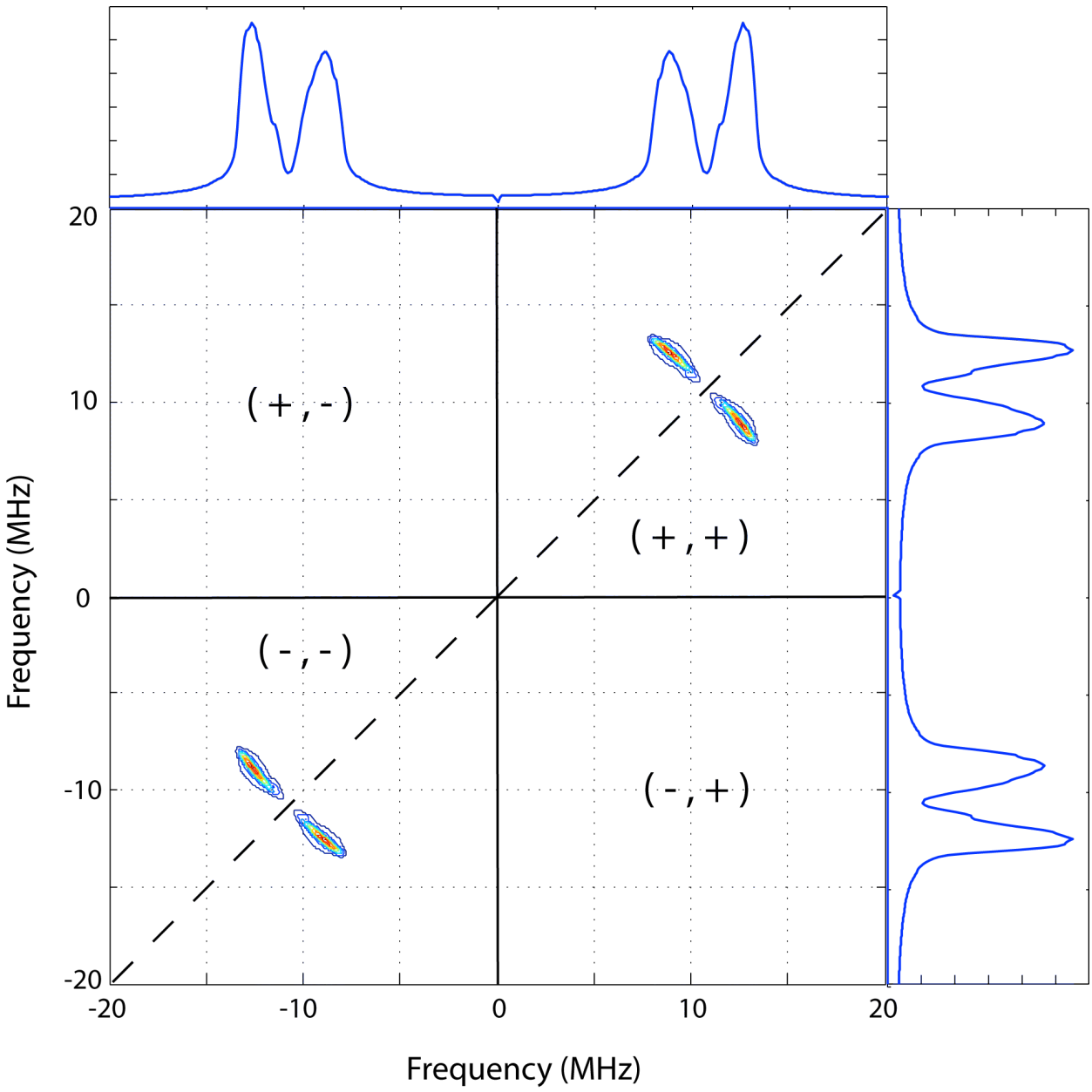

Figure 2.15 The four quadrant HYSCORE spectrum is the result of two dimensional Fourier transform. Each quadrant has a mirror image through the origin making for only two unique quadrants. Correlation peaks are created for frequencies owed to the same coupling in different spin manifolds.

The cross peaks are split about the point on the diagonal dashed line (Figure 2.15) that is the intersection of the nuclear Larmor frequency from each axis. Cross peaks can highlight the positions and shapes of the one dimensional ESEEM line features owed to unique couplings and

nuclei with different Larmor frequencies can be more easily resolved. The shapes of the cross peaks will be influenced by parameters from Equations 2.8 and 2.10 in a similar fashion to what is shown in Figure 2.12 for the one dimensional ESEEM spectra. Application of HYSCORE to the study of enzyme complexes will be detailed in chapters 3 and 4.

The utility in using HYSCORE to study $\{FeNO\}^7$ enzyme complexes is the enhanced resolution of HFI with protons on the directly coordinated ligands and, in some cases, on the nearby substrate. HYSCORE is essential for assigning ESEEM to specific couplings because of the substantial overlap of ^1H and ^{14}N spin echo modulation components. This is the only way that information in broadened spectral lines can be recovered using spin echo modulations. As with ESEEM, $\{FeNO\}^7$ enzyme complexes must be studied with HYSCORE at multiple field strengths to reconstruct the full picture of the nuclear spin state energies due to orientation selection in the individual spectra **(18)**.

2.7 CONCLUSIONS

The use of NO as a surrogate to O_2 in preparation of Fe(II) centered enzyme complexes provides a means for robust structural analysis of the catalytic center using EPR spectroscopy **(3, 9, 14)**. While CW EPR can be used to characterize the electronic structure and suggest the nature of NO binding for the $\{FeNO\}^7$ complex, ESEEM and HYSCORE can be used to measure the orientation of directly coordinated ligands and the position of any substrates bound near the $\{FeNO\}^7$ enzyme complex **(5, 16)**. Using CW EPR, ESEEM, and HYSCORE experiments together to study the same enzyme complex, ligand binding modes and structure-function

relationships can be correlated. The following two chapters will detail the application of these EPR techniques to the structural investigation of two non-heme Fe(II)/α-KG dependent hydroxylases, Taurine Hydroxylase (TauD) and Xanthine Hydroxylase (XanA).

BIBLIOGRAPHY

BIBLIOGRAPHY

1. Costas, M., M. P. Mehn, M. P. Jensen, and L. Que. 2004. Dioxygen activation at mononuclear nonheme iron active sites: Enzymes, models, and intermediates. Chem. Rev. 104:939-986.

2. Krebs, C., D. G. Fujimori, C. T. Walsh, and J. M. Bollinger. 2007. Non-heme Fe(IV)-oxo intermediates. Accounts Chem Res 40:484-492.

3. Enemark, J. H., and R. D. Feltham. 1974. Principles of Structure, Bonding, and Reactivity for Metal Nitrosyl Complexes. Coordin Chem Rev 13:339-406.

4. Gupta, R., D. C. Lacy, E. L. Bominaar, A. S. Borovik, and M. P. Hendrich. 2012. Electron Paramagnetic Resonance and Mossbauer Spectroscopy and Density Functional Theory Analysis of a High-Spin Fe-IV-Oxo Complex. J Am Chem Soc 134:9775-9784.

5. Prisner, T., M. Rohrer, and F. MacMillan. 2001. Pulsed EPR spectroscopy: Biological applications. Annu Rev Phys Chem 52:279-313.

6. Hendrich, M. P., and P. G. Debrunner. 1989. Integer-Spin Electron-Paramagnetic Resonance of Iron Proteins. Biophys J 56:489-506.

7. Gaffney, B. J. 2009. Epr of Mononuclear Non-Heme Iron Proteins. Biol Magn Reson 28:233-268.

8. Ye, S. F., J. C. Price, E. W. Barr, M. T. Green, J. M. Bollinger, C. Krebs, and F. Neese. 2010. Cryoreduction of the NO-Adduct of Taurine:alpha-Ketoglutarate Dioxygenase (TauD) Yields an Elusive {FeNO}(8) Species. J Am Chem Soc 132:4739-4751.

9. Brown, C. A., M. A. Pavlosky, T. E. Westre, Y. Zhang, B. Hedman, K. O. Hodgson, and E. I. Solomon. 1995. Spectroscopic and Theoretical Description of the Electronic-Structure of S=3/2 Iron-Nitrosyl Complexes and Their Relation to O-2 Activation by Nonheme Tron Enzyme Active-Sites. J Am Chem Soc 117:715-732.

10. Aquino, F., and J. H. Rodriguez. 2009. Accurate Calculation of Zero-Field Splittings of (Bio)inorganic Complexes: Application to an {FeNO}(7) (S=3/2) Compound. J Phys Chem A 113:9150-9156.

11. Hausinger, R. P. 2004. Fe(II)/alpha-ketoglutarate-dependent hydroxylases and related enzymes. Crit Rev Biochem Mol 39:21-68.

12. Diebold, A. R., C. D. Brown-Marshall, M. L. Neidig, J. M. Brownlee, G. R. Moran, and E. I. Solomon. 2011. Activation of alpha-Keto Acid-Dependent Dioxygenases: Application of an

{FeNO}(7)/{FeO2}(8) Methodology for Characterizing the Initial Steps of O-2 Activation. J Am Chem Soc 133:18148-18160.

13. Pilbrow, J. R. 1978. Effective G-Values for S = 3/2 and S = 5/2. J Magn Reson 31:479-490.

14. Muthukumaran, R. B., P. K. Grzyska, R. P. Hausinger, and J. McCracken. 2007. Probing the iron-substrate orientation for taurine/alpha-ketoglutarate dioxygenase using deuterium electron spin echo envelope modulation spectroscopy. Biochemistry-Us 46:5951-5959.

15. Mims, W. B. 1972. Envelope Modulation in Spin-Echo Experiments. Phys Rev B-Solid St 5:2409-&.

16. Calle, C., A. Sreekanth, M. V. Fedin, J. Forrer, I. Garcia-Rubio, I. A. Gromov, D. Hinderberger, B. Kasumaj, P. Leger, B. Mancosu, G. Mitrikas, M. G. Santangelo, S. Stoll, A. Schweiger, R. Tschaggelar, and J. Harmer. 2006. Pulse EPR methods for studying chemical and biological samples containing transition metals. Helv Chim Acta 89:2495-2521.

17. Hahn, E. L., and D. E. Maxwell. 1952. Spin-Echo Measurements of Nuclear Spin-Spin Coupling. Phys Rev 85:762-762.

18. Blinder, S. M. 1960. Orientation Dependence of Magnetic Hyperfine Structure in Free Radicals. J Chem Phys 33:748-752.

CHAPTER 3

STRUCTURAL INVESTIGATION OF THE CATALYTIC CENTER OF TAURINE HYDROXYLASE WITH CW EPR, ESEEM, AND HYSCORE

INTRODUCTION

Taurine Hydroxylase (TauD) is the archetype enzyme for the family of non-heme Fe(II)/ α-KG dependent dioxygenases **(1)**. When a $\{FeNO\}^7$ complex is prepared at TauD's catalytic center, the spectroscopic properties of the relatively well ordered coordination arrangement are the most ideal for the application of pulsed EPR studies of enzymes in this family. This chapter details the application of CW EPR, ESEEM, and HYSCORE experiments to the $\{FeNO\}^7$ complex prepared at the catalytic center of TauD samples for measurement of structural characteristics. The interpretation of the data not only supports and adds to previous structural findings for TauD but suggests the efficacy of these EPR techniques for making structural observations of the catalytic center of other Fe(II) dependent enzymes using the $\{FeNO\}^7$ complex as a spectroscopic probe.

3.1 TAURINE HYDROXYLASE

TauD was first reported in 1997 **(2)** as an α-KG dependent dioxygenase encoded by the tauABCD gene cluster of *E. coli*. The genes tauA, tauB, and tauC were responsible for the expression of a transport complex for uptake of taurine, but TauD's 30% sequence identity with a previously isolated α-KG dependent 2,4-dichlorophenoxyacetate dioxygenase (encoded by the tfdA gene) and the subsequent observation of a dependence on Fe(II) and α-KG led to its assignment to the non-heme Fe(II) and α-KG dependent dioxygenase class. In *E. coli* TauD is

responsible for the conversion of taurine to aminoacetaldehyde and bisulfite (HSO_3^-) for providing a sulfur source **(2)**. This enzyme is one of the most well studied members of the α-KG dependent dioxygenase family due to its relative abundance, stability, and available crystallographic data **(3-5)**. Since 1997 TauD has been shown to exhibit all of the characteristics that are now considered standard for the bulk of mononuclear non-heme Fe(II) /α-KG dependent dioxygenases including the "jelly roll" tertiary structure and the "facial triad" Fe(II) coordination motif **(1)**. Crystal structures for TauD exist with reasonable degrees of resolution **(3, 4)** and show similarity to high resolution crystal structures for other members of this enzyme family **(6)**. Figure 3.1 shows pictures of the catalytic center of TauD as rendered in two different crystallographic studies.

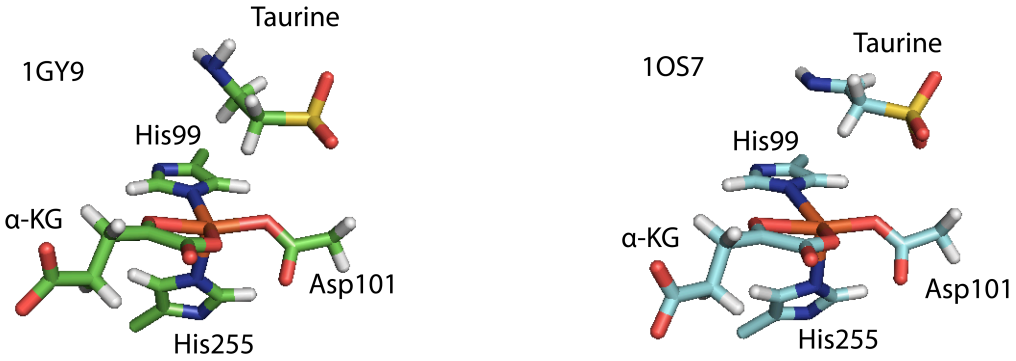

Figure 3.1. Two of the crystal structures for TauD that have been reported are the 1GY9 **(3)** and 1OS7 **(4)** structures. Both are absent of O_2 or NO making the Fe(II) center five coordinate. Other than slight tilts in the binding orientations of the His ligands and a rotation of the taurine molecule the two structures are reasonably similar.

Much of what is known both theoretically and experimentally about the general details of the mechanisms for enzymes in this family has been learned by using TauD as a subject **(7-10)**.

TauD's robust nature and relative simplicity of substrate make it ideal for the refining of experimental and theoretical analysis techniques that can prove valuable when studying other relatively more complex or less characterized members of this family. Figure 3.2 shows a generally agreed upon mechanism for TauD **(11, 12)**.

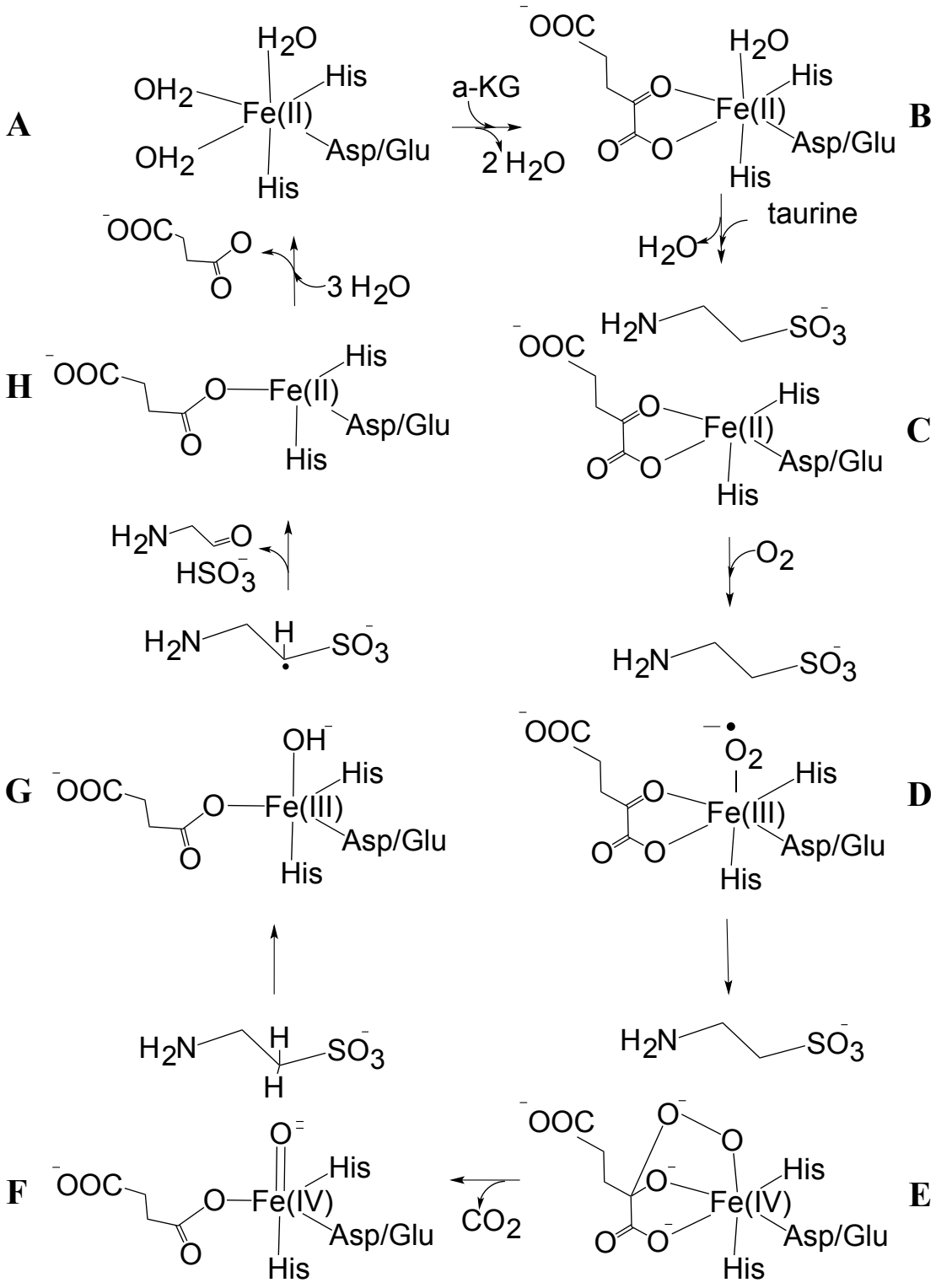

Figure 3.2. Studies on the mechanism of TauD have formed the basis for much of what is generally accepted for non heme Fe(II)/aKG dependent hydroxylases. The hydrogen abstraction (F-G) and hydroxyl rebound (G-H) steps have recieved a great deal of theoretical study and recently some of the intermediates have been observed spectroscopically **(10-16)**.

In chapter 1 (Figure 1.6) it is pointed out that some details of the hydroxylation steps pictured in Figure 3.2 are subject to multiple interpretations after more recent spectroscopic findings by Grzyska and coworkers **(17)**. This more recent assertion is that the mechanism for hydroxylation of taurine can involve a direct attack by the Fe(IV)=O species at the C1 position on taurine. For this to take place instead of the more commonly accepted pathway for hydroxylation (Figure 3.2), it is likely necessary that taurine is closer to the Fe(IV)=O species to allow for competition with the more energetically favorable pathway of hydrogen abstraction followed by radical rebound **(7, 18)**. Sub Å resolution of taurine's position is desirable for a structural study to lend to energetic arguments.

3.2 PURPOSE

The wealth of quantitative structural and mechanistic information available for TauD have made possible the inference of various relationships between its structure and proposed mechanism but most of these studies do not represent a direct correlation of the two. Crystal structures for TauD are for anaerobic crystals that are five coordinate as opposed to the six coordinate Fe(II) center that is native to the functioning enzyme **(3, 4)**. In addition, the placement of a small molecule such as taurine in the substrate binding pocket is subject to considerable error at the resolution of the known crystal structures. A previous study by Muthukumaran et al. **(19)** used ESEEM to make direct measurements of the position of taurine's C1 and C2 deuterons near the six coordinate Fe(II) center using an $\{FeNO\}^7$ complex as a spectroscopic probe. A NO molecule was manually modeled into a TauD crystal structure to give the measurements visual context. The analysis of the data was carried out using visual fitting of line shapes in ESEEM

spectra collected near the $g_{\perp}$=4 and $g_{\parallel}$=2 regions of the EPR spectrum. While the measurements generally agree with previous structural data, the frequency amplitudes were not fit and the data set did not include many of the orientations of the spin system that would be observed with experiments at field positions between the $g_{\perp}$=4 and $g_{\parallel}$=2 regions. Analyzing the frequency amplitudes as a function of the orientation of the spin system would yield significant additional information **(20)**. In addition, the study does not include statistical support for the "best" set of parameters obtained with manually fitting the line shapes in the ESEEM spectra. To date, direct measurements of the position and orientation of the His ligands that are coordinated to Fe(II) center of non-heme Fe(II) dependent enzymes are not available. While structural changes can be inferred for coordination of the α-KG and arrival of the taurine during the catalytic mechanism, the direct effect of α-KG and taurine on the coordinated ligands has not been measured.

The purpose of the experimental work detailed in this chapter is to 1) Continue the previous study by Muthukumaran et al. **(19)** with a more complete ESEEM analysis, lend statistical support to the "best" set of parameters used to fit the data, and provide an energy optimized crystal structure for comparison. 2) Use HYSCORE to directly observe the position and orientation of the coordinated His ligands and evaluate their position and orientation as a function of taurine and α-KG.

With this information the position of taurine can be directly correlated to the Fe(II) complex with the resolution needed to aid in the understanding of it's involvement in the mechanism, the orientation of the His ligands in the reactive enzyme complex can be measured,

and the structural importance of taurine and α-KG in preparing the active site for reaction can be studied.

3.3 EXPERIMENTAL

Sample preparation. The chemicals used in preparation were purchased from Sigma Aldrich. The taurine deuterated at both the C1 and C2 positions was purchased from C/D/N Isotopes. The C1 deuterated taurine was provided by J.C. Price and M. Bollinger. TauD protein was expressed and purified by the Hausinger group. Piotr Grzyska performed the anaerobic preparation of the frozen TauD samples by first suspending TauD apoprotein in degassed 20 mM Tris buffer at pH=8.0 that was then treated with degassed solutions of Fe(II), taurine, and α-KG such that the final concentrations were: 1.5 mM TauD protein, 1.5 mM Fe(II), 6.0 mM taurine and 6.0 mM α-KG. The solutions were then treated with NO by filling the headspace of the sealed sample vial with NO gas and lightly swirling the solution. Upon the observation of the solution changing to a yellow color, the solution was quickly transferred anaerobically to an EPR tube with a syringe and frozen in liquid nitrogen. Additional samples were prepared in an identical fashion but were either treated with deuterated or per deuterated taurine in place of taurine, prepared without taurine, prepared without α-KG, or without α-KG and taurine.

CW EPR experiments. CW EPR spectra were collected on a Bruker ESP300E X-Band EPR spectrometer operating at 9.47 GHz. A model ST4102 probe was used and the temperature was maintained at 4 K using an Oxford Instruments ESR-900 liquid helium flow system. Helium flow was adjusted manually to maintain constant temperature. All EPR spectra were collected over a 300 mT range centered at 250 mT, with a modulation amplitude of 1 mT, a modulation

frequency of 100 KHz, and at a power and video gain appropriate to each sample (judged by saturation of the EPR signal and signal to noise ratio of the spectrum at the optimum power). Spectra were averaged as necessary. Spectra were fit using the "esfit" function in the EasySpin software package **(21)** to determine the ZFS parameters and the line width parameters.

ESEEM experiments. ESEEM spectra were collected using a Bruker E680 X band spectrometer using a model ER4118-MD-X-5-W1 probe with a 5 mm dielectric resonator. An Oxford instruments model ITC-503 temperature controller and CF-935 liquid helium flow system was used to maintain a constant temperature of 4 K during ESEEM measurements. Data was collected using a three pulse stimulated echo sequence that consisted of three 16ns $\pi/2$ (90°) microwave pulses as follows ($\pi/2$ - τ - $\pi/2$ - T1 - $\pi/2$). The time spacing τ was fixed and the spin echo was integrated as a function of T1. Data sets consisted of 512 points and were collected with a four step phase cycling procedure: (+,+,+), (-,+,+), (+,-,+), and (-,-,+) to remove unwanted echoes and baseline offsets. Plots of integrated echo amplitude vs. time spacing (T1) were baseline corrected, treated with a Hamming window, zero filled to 1024 points, and cosine Fourier transformed to observe the frequency spectrum. Data sets were collected every 20 mT starting with 170 mT and ending at 330 mT.

Deuterium ESEEM. Identical ESEEM experiments were carried out on samples made with taurine, C1 deuterated taurine, and taurine deuterated at the C1 and C2 positions. Three different ratios of the normalized time domain data were taken to filter out unwanted ^{1}H and ^{14}N modulations and isolate the ESEEM from the C1 and C2 deuterons alone as well as the C1 and C2 deuterons together. To isolate the ^{2}H ESEEM from the C1 deuteron, time domain ESEEM data collected for the TauD samples having C1-^{2}H-taurine were divided by corresponding data

collected for TauD samples having taurine. To isolate the ^{2}H ESEEM from the C2 deuteron, time domain ESEEM data collected for the TauD samples having taurine deuterated at the C1 and C2 positions were divided by corresponding data collected for TauD samples having C1-^{2}H-taurine. To isolate the ^{2}H ESEEM from the C1 and C2 deuterons together, time domain ESEEM data collected for the TauD samples having taurine deuterated at the C1 and C2 positions were divided by corresponding data collected for TauD samples having taurine. The ratio ESEEM data were baseline corrected, treated with a Hamming window, zero filled to 1024 points, and cosine Fourier transformed to observe the frequencies owed to the ^{2}H couplings.

Fitting ESEEM data. The ESEEM spectra obtained with the ratios were dominated by a peak centered at the deuterium Larmor frequency. The data points that defined the peak were isolated and compared to their corresponding points in simulated spectra. The simulated spectra were calculated with the EasySpin software package **(21)** running in MATLAB (See Appendix D for the MATLAB scripts used to calculate the spectra). The time domain data and simulated time domain spectra were processed in an identical fashion. The differences between the experimentally obtained ^{2}H ESEEM line shapes and the simulated line shapes were analyzed by calculating a χ^2 value for each spectrum using Equation 3.1:

$$\chi^2 = \sum_i \frac{\left(y_i^{data} - y_i^{simulation}\right)^2}{\sigma_i^2} \qquad \textbf{[3.1]}$$

During the optimizations the data points in each spectra were weighted according to an estimated variance (σ_i) judged by a ratio of the amplitude of the largest "noise" peak in a spectral region

distant from the deuterium Larmor frequency to the amplitude of the ^{2}H ESEEM peak. Due to orientation selection effects in the individual ESEEM spectra the fits that resulted in the best reproduction of the entire data set were observed when fitting multiple spectra in parallel that spanned the EPR spectrum as opposed to localized in one field region. The optimizations were carried out with routines native to MATLAB that used fitting algorithms to iteratively vary specific Hamiltonian parameters while calculating the spectra and a χ^2 from comparison to the data until χ^2 was at a minimum. Various algorithms were used including Nelder/Mead simplex **(22)**, genetic algorithm **(23)**, and simulated annealing **(24)** to fit up to six spectra in parallel. In many cases, calculating χ^2 while varying multiple parameters allows for more than one local minimum to exist. The global minimum can be most successfully found with a global optimization algorithm that uses a heuristic search method, such as simulated annealing. This algorithm allows for the successive polling of new parameter sets that may more closely resemble previous parameter sets that were "less fit" as opposed to rejection of any "less fit" parameter set. The probability (P_i) that any parameter set (i) is accepted as the starting parameter set in successive generations of the optimization is given by:

$$P_i = \frac{1}{1 + \exp^{\left(\frac{\Delta}{T_i}\right)}} \qquad \textbf{[3.2]}$$

T_i is calculated using:

$$T_i = \frac{T_0}{\log(K_i)} \qquad [3.3]$$

Where K_i is the annealing parameter (usually the iteration number) and Δ is:

$$\Delta = \chi_i^2 - \chi_{Best}^2 \qquad [3.4]$$

This means that even a "less fit" parameter set has a non zero probability of being accepted for the basis of the next generation. As the iteration number increases and the temperature parameter decreases the probability of accepting a "less fit" parameter set decreases. In this way simulated annealing can avoid being stuck in a potentially false local minimum at the beginning of the optimization and pursue a different nearby minimum that may be the global minimum. As the optimization proceeds, it is less likely that the algorithm will leave the current minimum. See Appendix C for more about the simulated annealing fitting algorithm. The spectra with isolated C1 ^{2}H modulations and the spectra with isolated C2 ^{2}H modulations were subjected to the fitting procedure. The spectra containing both C1 and C2 ^{2}H modulations were simulated using these findings and not subjected to fitting.

The Hamiltonian model presented in chapter 2 was used to calculate the simulated spectra. The parameters that were varied by the fitting algorithm were the dipolar coupling strength (T in Equation 2.8), the β_{HF} angle relating the principal axes of the ***A*** tensor to the ZFS tensor, the magnitude of the NQI (e^2qQ/h), the β_{NQI} angle relating the principal axes of the ***Q"*** tensor to the ZFS tensor, and the γ_{NQI} angle relating the ^{2}H-C bonds to an axis defined by the

plane containing the Fe, N, and ^{2}H nuclei (see D_X in Figure 3.3). The dipolar distance (r) was calculated using the point dipole approximation, Equation 3.3:

$$T = \frac{g_e \beta_e g_N \beta_N}{r^3} \qquad \textbf{[3.5]}$$

When describing the orientation of the ***A*** tensor for ^{2}H to the principal axis of the axial ZFS tensor it is only necessary to specify the β_{HF} angle. When the ZFS is purely axial, different projections of the ***A*** tensor onto the equatorial plane are indistinguishable. Because the HFI is purely dipolar (a_{iso}=0) and the electric field gradient that interacts with the ^{2}H quadrupole moment is arising from the electrons in the ^{2}H-C σ bond, the ***A*** and ***Q"*** tensors are also axial (ρ=0 in Equation 2.8 and η=0 in Equation 2.10). The β_{NQI} angle is necessary to describe the orientation of the ***Q"*** tensor (^{2}H-C bond) in relation to the principal axis of the axial ZFS. As discussed in chapter 2 the principal axis of the ZFS that defines the magnetic axis used for reference in EPR studies is nearly coincident with the Fe-N(O) bond **(25)**. In this study, the principal axis of the ZFS and the direction of the Fe-N(O) bond are considered synonymous on the basis of the previous theoretical work **(25)**. Figure 3.3 illustrates the physical meanings of the Euler angles.

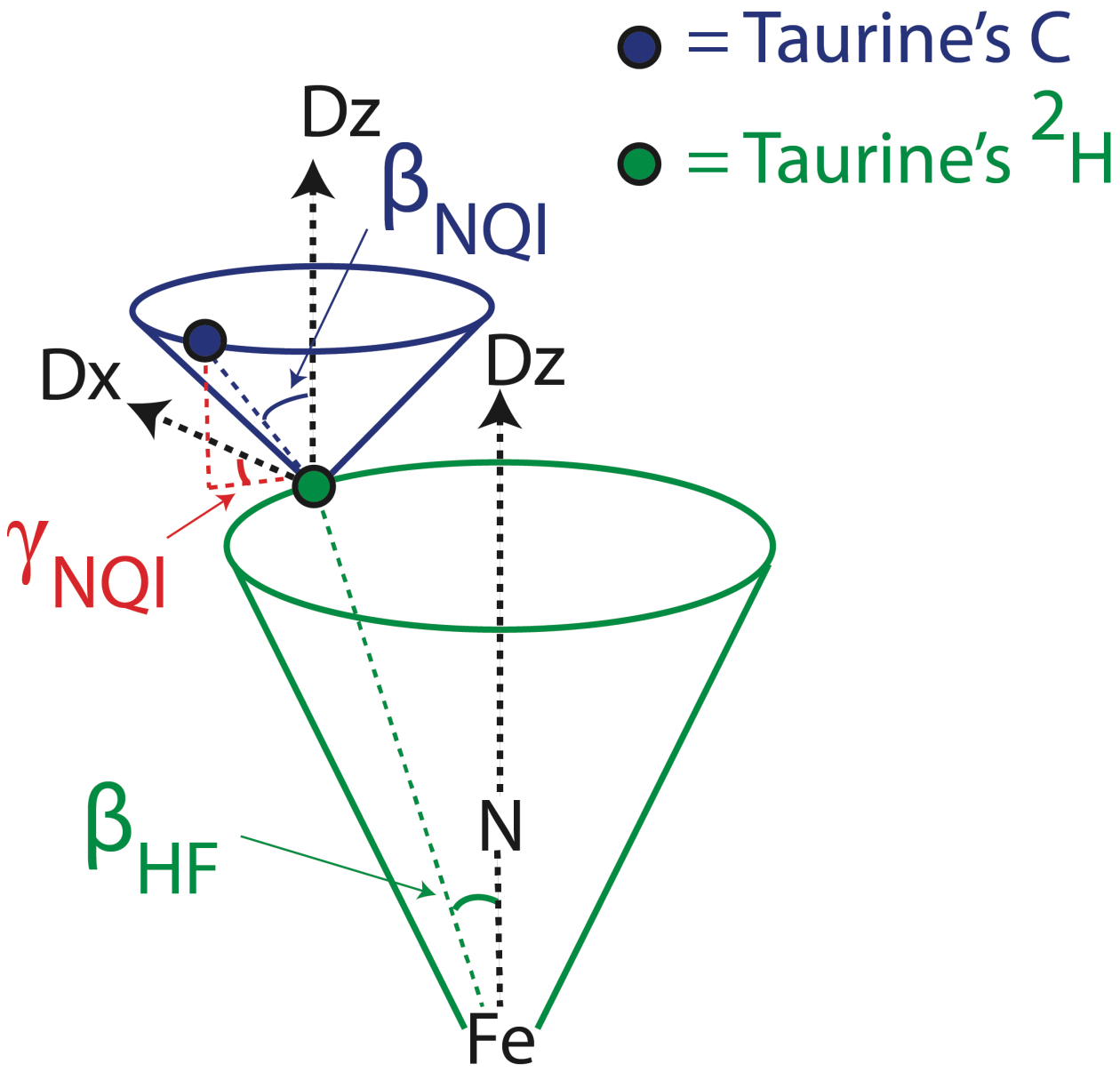

Figure 3.3. The green cone represent the range of γ_{HF} that would be indistinguishable in the analysis of the ESEEM results when the ZFS is axial. Because the HFI and NQI are also axial, all γ_{NQI} angles would be indistinguishable as well. However, if the plane containing the projection of the HFI vector, the N of NO and Fe is made to define the D_X axis, the γ_{NQI} can be used to define the projection of the NQI tensor in reference to the projection of the HFI tensor. This reduces the blue cone describing the direction of the ^{2}H-C bond to a single orientation.

Although the axial ZFS makes definition of γ_{NQI} ambiguous in the ZFS tensor, the relationship between the ***A*** and ***Q"*** tensors is important because it affects the EPR transition probabilities that

determine the ESEEM amplitudes. When the orientations of the principal axes of the ***A*** and ***Q"*** tensors to the principal axis of the ZFS have been established, the γ_{NQI} angle can allow for the estimation of the relative orientation of the ^{2}H-C bond in the principal axis system of the HFI. With the combination of β_{HF}, β_{NQI}, and γ_{NQI} taurine's orientation relative to the magnetic axes of the $\{FeNO\}^7$ complex can be inferred. The interpretation of the Euler angles and the structural implications will be discussed in the context of the results in the discussion section.

Further statistical analysis was performed once the "best" set of parameters was obtained from the optimizations in order to estimate the standard deviation (σ) in each parameter. Because the parameters are covariant, σ was calculated from a covariance matrix. First, a Jacobian matrix ($J_{n\ x\ m}$) can be constructed consisting of m rows corresponding to the number of data points being compared in the calculation of χ^2 and n columns corresponding to the number of parameters being varied:

$$J_{n\times m}=\begin{pmatrix} \frac{\partial f(y_1)}{\partial p_1} & \cdots & \frac{\partial f(y_1)}{\partial p_n} \\ \vdots & \ddots & \vdots \\ \frac{\partial f(y_m)}{\partial p_1} & \cdots & \frac{\partial f(y_m)}{\partial p_n} \end{pmatrix} \qquad \textbf{[3.6]}$$

where f is the function used to calculate χ^2 and p_n are the individual parameters that were varied in the optimization. Each y_m is a point in the data set that is being compared to the corresponding point in the simulation. Each term in the Jacobian matrix is defined as,

$$\frac{\partial f(y_m)}{\partial p_n} = \frac{\left(f(p_n + dx_n) - f_{best}\right)_m + \left(f(p_n - dx_n) - f_{best}\right)_m}{2dx_n} \quad \textbf{[3.7]}$$

The covariance matrix can be calculated from the Jacobian matrix by taking the inverse of the product of the Jacobian ($J_{n\ x\ m}$) with its transpose ($J'_{n\ x\ m}$) and multiplying by the χ^2 for the parameter set being evaluated (χ^2_{best}) divided by the difference between the number of data points (m) and the number of variable parameters (n):

$$Cov = \frac{\chi^2_{best}}{m-n}\left(J^T_{n\times m} * J_{n\times m}\right)^{-1} \quad \textbf{[3.8]}$$

After solving for the eigenvalues of the covariance matrix, the standard deviations in each Hamiltonian parameter (σ_n) are the square roots of the corresponding diagonal terms. The 95% confidence interval for each Hamiltonian parameter p_n is defined as the range from $2\sigma_n$ below to $2\sigma_n$ above the "best" value. See Appendix C for more explanation of the simulated annealing algorithm. Appendix D contains the MATLAB code used to calculate the covariance matrix and the standard deviations and gives a comparison of multiple methods for statistical analysis of the parameters.

HYSCORE experiments. HYSCORE spectra were collected using the same instrumentation and conditions as the ESEEM experiments. A four pulse sequence was used consisting of three 16 ns π/2 microwave pulses and one 32 ns π microwave pulse between the second and third π/2 pulses. The pulses were separated by three time spacings as follows (π/2 - τ - π/2 - T1 - π - T2 - π/2). A spin echo was integrated over a time width centered at τ after the fourth pulse as a function of

both T1 and T2. The time spacing τ was chosen to suppress modulations from matrix protons. Data sets were 128 x 128 point square matrices consisting of 128 different T1 points for each of the 128 T2 points. The data sets were recorded with a four step phase cycling procedure to remove unwanted echoes and baseline offsets. For visualization of the two dimensional frequency spectrum each row and column of the square matrix was baseline corrected, treated with a hamming window, zero filled to 512 points separately. The entire matrix was subjected to two dimensional Fourier transformation. HYSCORE spectra for the TauD sample treated with α-KG and taurine were collected at 10 mT increments spanning the EPR spectrum (170 - 330 mT). For the samples containing C1 deuterated taurine, C1 and C2 deuterated taurine, or the samples missing either taurine or α-KG HYSCORE spectra were collected at six field positions (170, 190, 240, 280, 300, and 320 mT). The data were interpreted by simulation using the EasySpin software package **(21)** operating in MATLAB. Hamiltonian parameters were refined by manual adjustment from an initial set of parameters that were inferred from ESEEM and crystallographic data. The parameters that were varied when simulating the HYSCORE spectra were the isotropic HF coupling (a_{iso} in Equation 2.8), the dipolar coupling strength (T in Equation 2.8), and a β_{HF} Euler angle relating the principal axes of $\boldsymbol{A}$ tensor to the ZFS tensor (Fe-N(O) bond). Isotropic HF coupling (a_{iso}) arises from a non zero probability of unpaired spin density at the coupled nucleus. The directly coordinated His ligands can share some of the unpaired spin by way of direct coordination to the paramagnetic $\{FeNO\}^7$ complex so a_{iso} was considered when interpreting the HYSCORE data.

Optimizations of the 1GY9 crystal structure with Avogadro. The crystal structure used for comparison was the 2.5 Å resolution 1GY9 structure **(3)**. One of the reasons it was chosen was

its close similarity to the 1GVG structure **(6)** (1.54 Å resolution) for CAS that was obtained with NO as a surrogate to O_2. A geometry optimization was performed using the Avogadro software package **(26)**. A theoretical model of the NO and taurine positions was generated by adding a bound NO to the Fe(II) center of the 1GY9 crystal structure and, while holding the position of the surrounding protein and Fe(II) center constant, the positions of taurine and NO were energy minimized together using the Unified Field approximation (UF). In UF theory all fundamental forces are represented together as a unified "field" that can be used to quantify local interactions. The optimization is dependent on the assumption that the crystal structure was more accurate in modeling the protein side chains and Fe(II) center than it was the position of taurine. An additional optimization of taurine's position in the 1GY9 crystal structure **(3)** without NO was performed by Rahul Banerjee under the supervision of Dr. Robert Cukier using Dock6 software **(27)** and is available in Appendix B.

3.4 RESULTS

CW EPR. The CW EPR spectra of the various TauD samples are characteristic of large axially symmetric ZFS with principal effective g values of $g_{\perp}=4$ and $g_{\parallel}=2$. Figure 3.4 shows experimental and simulated CW EPR spectra for the various TauD samples that were studied.

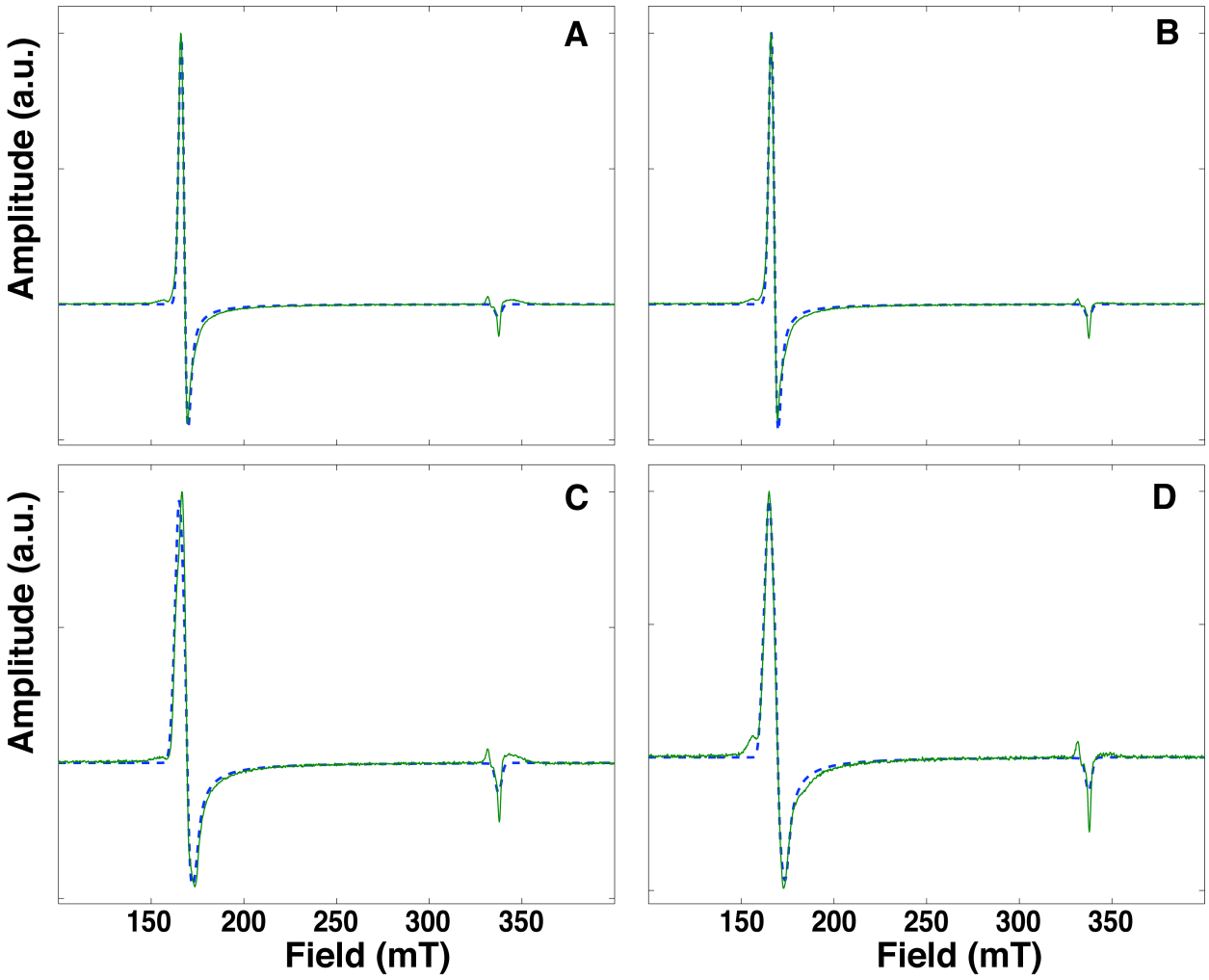

Figure 3.4. The experimental EPR spectra (in green) were fit (blue dashed line) with the "esfit" function in the EasySpin software package **(21)**. In each case D = 10 cm^{-1}. The TauD samples that had (A) α-KG and taurine or (B) ^{2}H-taurine were fit to an axial model with E/D = 0 and a line width parameter lwpp= 3.21 mT. The TauD samples that were (C) missing taurine or (D) missing α-KG showed additional line broadening and were also fit to a model with E/D = 0 but a line width parameter lwpp= 4.7 and 4.9 mT respectively.

The samples that were treated with α-KG and either ^{1}H or ^{2}H taurine gave identical EPR spectra (Figure 3.4A,B) having a sharp featureless line at $g_{\perp}$=4 indicating little variability in the axiality of the ZFS tensor. For modeling these spectra, D was assumed to be ≥ 10 cm^{-1} on the basis of

previous studies and theoretical predictions **(8, 25)**. *E/D* was assumed to be 0. The minor broadening of the $g_{\perp}$=4 feature was modeled with a simple line width parameter, lwpp=3.21 mT.

The $g_{\perp}$=4 feature in the EPR spectra for the samples that were missing α-KG or taurine showed additional broadening (lwpp= ~4.8 mT). This is likely due to a small variability in NO binding. Conformational flexibility of the coordinated ligands had previously been suggested for the non-heme Fe(II) active site in the absence of substrate or cofactor **(1, 13)** and could account for the observed line broadening. This minor additional broadening can be modeled with introduction of a relatively small *E/D* value, *E* or *D* strain, or by increasing the line width parameter each having the same effect on the spectrum. Without clear line splitting, the individual contributions of a small *E/D*, *E* strain, or *D* strain to the slight broadening cannot be determined separate from each other. For this reason, the broadening was accounted for with a lwpp and any *E/D*, *E* strain, and *D* strain were assumed to be immeasurable. Instead, relative magnitudes of the lwpp were used to assume relative degrees of conformational flexibility. An additional sample was analyzed that was missing both α-KG and taurine. Figure 3.5 is the CW EPR spectrum for the TauD sample having been treated with NO in the absence of α-KG and taurine.

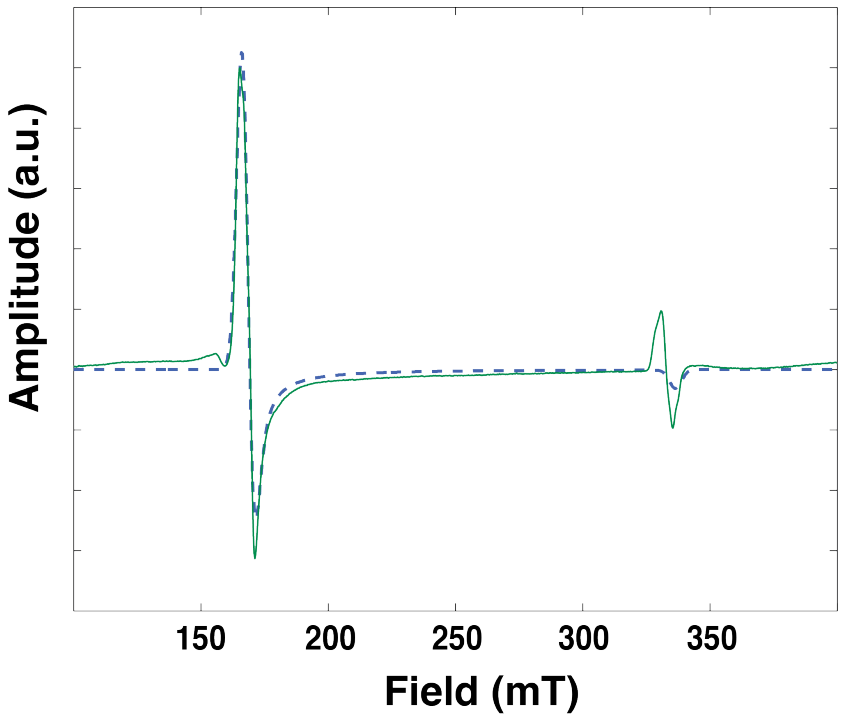

Figure 3.5. The experimental EPR spectrum for the sample missing α-KG and taurine (in green) was fit (blue dashed line) with the "esfit" function of the EasySpin software package **(21)**. Again the D = 10 cm^{-1}. The lwpp in this case was 4.8 mT.

The enhancement of the line broadening (lwpp=4.8 mT) from what was observed in the samples having α-KG and taurine was similar to what was observed when either α-KG or taurine were missing while the other was present. The additional broadening in this case is also attributed to a slight variability in the NO binding allowed by the slight conformational flexibility that accompanies the absence of α-KG and taurine.

Deuterium ESEEM. Figure 3.6 shows the frequency domain ESEEM ratio spectra along with their fits for the isolation of the ESEEM signal owed to the ^{2}H at the C1 position on taurine.

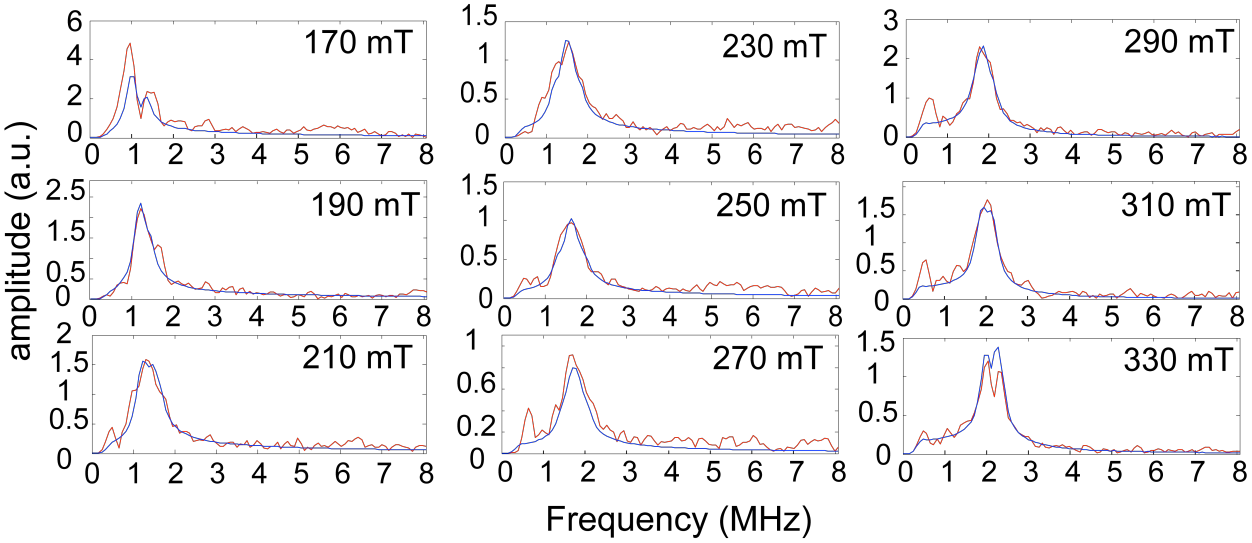

Figure 3.6. The experimental data (red) for the measurement of the C1 ^{2}H position were fit (blue) by using the simulated annealing algorithm in the MATLAB global optimization toolbox. The parameters used to calculate the simulated spectra (blue) were: T=3.86 Å, β_{HF}=26˚, e^2qQ/h=0.22 MHz, β_{NQI}=52˚, and γ_{NQI}=155˚.

Table 3.1 highlights some of the results of the fitting procedure for the C1 ^{2}H coupling.

χ^2 / min χ^2	r (Å)	β_{HF} (˚)	e^2qQ/h (MHz)	β_{NQI} (˚)	γ_{NQI} (˚)
1	3.85	26.4	0.22	51.6	154.6
1.2	3.85	26.4	0.22	51.6	25.4
1.8	3.85	33.8	0.27	14.3	137.5
1.8	3.85	33.8	0.27	167.3	40.1

Table 3.1 Four parameter sets tested by the simulated annealing algorithm that have similar χ^2 values are listed. The χ^2 values for each parameter set were normalized to the lowest χ^2 value.

Table 3.2 lists the "best" parameter set that resulted in the fits in Figure 3.6 with the 95% confidence intervals (+/- 2σ) calculated from a covariance matrix.

Hamiltonian parameters	"best" value	95% Conf. Interval
r (Å)	3.86	3.65-4.14
β_{HF} (˚)	26.4	21.3-31.4
e^2qQ/h (MHz)	0.22	0.09-0.35
β_{NQI} (˚)	51.6	34.6-68.6
γ_{NQI} (˚)	154.6	102.9-206.5

Table 3.2. The 95% confidence interval was calculated as +/- 2σ. The σ for each parameter is the square root of the corresponding diagonal term in the covariance matrix. See Appendix D for the procedure used in calculating σ.

The fitting procedure was most successful with the frequency domain data. The division of the time domain data in the region beyond T1= 3000 ns introduces considerable noise that masks any ^{2}H modulations that would be visible in this region. Fitting of the time domain ratio data would not only be more exhaustive due to more data points being needed to define the modulations but would only be able to draw information from the first ~3000 ns of modulations (see time domain spectra in Figure 3.6). While reproducing the frequency amplitudes from only the initial modulation depths can be accurate, frequency resolution is greatly hindered. The width and shape of the peak in the frequency spectrum is not only defined adequately with fewer data points (less exhaustive fitting) but may provide a more reliable picture of the nuclear spin state energies.

The ratio ESEEM data set that isolated the ^{2}H modulations from the C2 deuteron was subjected to the same fitting and statistical analysis procedure. Figure 3.7 shows fits for four of the nine field positions at which spectra were collected.

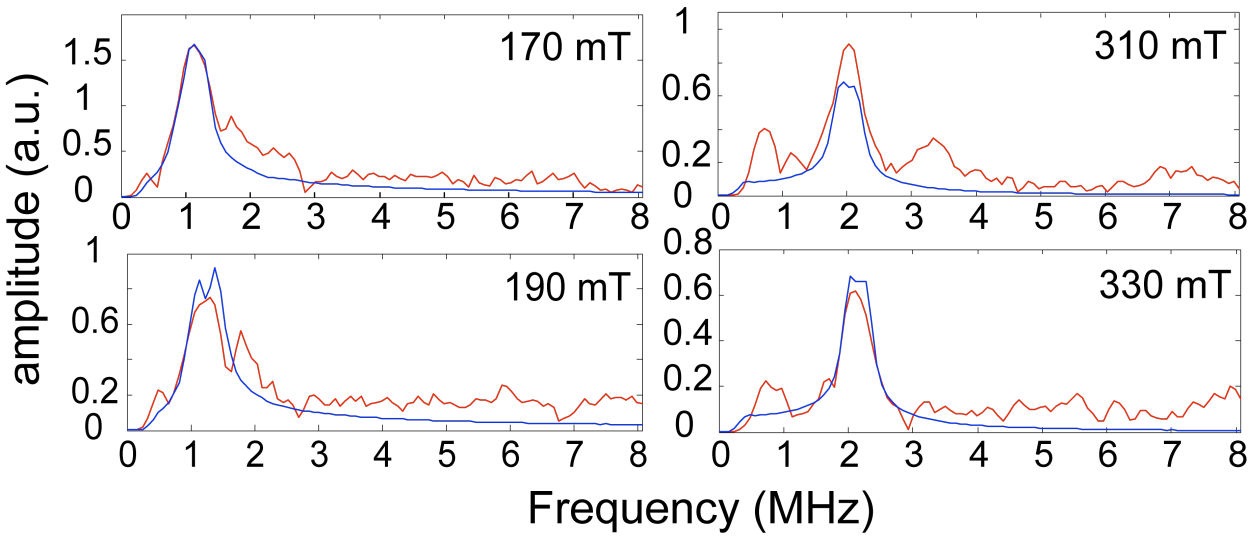

Figure 3.7. The experimental data (red) for the measurement of the C2 ^{2}H position were fit (blue) by using the simulated annealing algorithm in the MATLAB global optimization toolbox. The parameters used to calculate the simulated spectra (blue) were: T=4.66 Å, β_{HF}=37˚, $e^{2}qQ/h$=0.22 MHz, β_{NQI}=106˚, and γ_{NQI}=143˚.

The signal to noise ratio was much lower and the divisions were less successful due to the longer distance interaction with the C2 deuteron. ESEEM amplitude drops off as ~ $1/r^{6}$ so the distance range that is likely for the C2 deuteron (> 4 Å) **(3, 4, 19)** would result in much lower amplitudes of the frequency peaks and difficulty resolving the peaks above the noise level. Regardless, at the ends of the EPR spectrum (170 mT, 190 mT, 310 mT, and 330 mT) where the peak amplitudes are expected to be greatest the divisions isolated clear peaks at the deuterium Larmor frequency that were able to be fit.

Table 3.3 highlights some of the results of the fitting procedure for the C2 ^{2}H coupling.

χ^2 / min χ^2	r (Å)	β_{HF} (˚)	e^2qQ/h (MHz)	β_{NQI} (˚)	γ_{NQI} (˚)
1	4.66	37.2	0.22	106.0	143.2
1.13	4.66	37.2	0.22	85.9	36.7
1.18	4.66	37.2	0.22	85.9	143.2
1.89	4.75	29.8	0.23	63.0	40.1

Table 3.3 Four parameter sets tested by the simulated annealing algorithm that have similar χ^2 values are listed. The χ^2 values for each parameter set were normalized to the lowest χ^2 value.

Table 3.4 lists the "best" parameter set that resulted in the fits in Figure 3.7 with the 95% confidence intervals (+/- 2σ) calculated from a covariance matrix.

Hamiltonian parameters	"best" value	95% Conf. Interval
r (Å)	4.66	4.40-4.99
β_{HF} (˚)	37.2	24.8-49.7
e^2qQ/h (MHz)	0.22	-0.11-0.56
β_{NQI} (˚)	106.0	43.4-168.5
γ_{NQI} (˚)	143.2	48.7-235.0

Table 3.4. The 95% confidence interval was calculated as +/- 2σ. The σ for each parameter is the square root of the corresponding diagonal term in the covariance matrix. See Appendix D for the procedure used in calculating σ.

The ratio ESEEM data that contained the ^{2}H modulations from the C1 and C2 deuterons together were not fit but were simulated using the parameters obtained from fitting the previous two data sets. Figure 3.8 shows the comparison spectra.

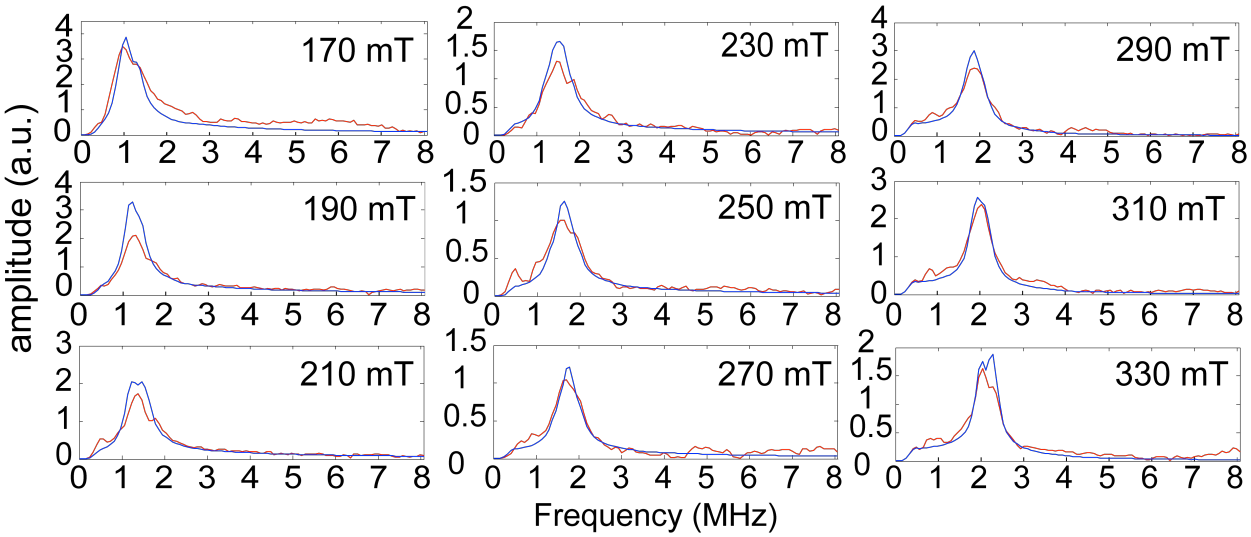

Figure 3.8. The experimental ESEEM spectra (red) that isolated the modulations from the C1 and C2 deuterons in the same spectrum were simulated (blue) using the parameter sets listed in Tables 3.2 and 3.4.

The ratio spectra were dominated by modulations owed to the C1 ^{2}H but the correct amplitudes and line shapes are only accounted for by an additional coupling consistent with the parameters for the C2 ^{2}H (Table 3.4). The greatly enhanced signal to noise ratio is simply a product of the enhanced ^{2}H contribution to the ESEEM signal when there is coupling to two ^{2}H nuclei.

HYSCORE. The cross peaks in the HYSCORE spectra collected for the TauD samples that were prepared with taurine and α-KG were consistent with couplings to at least two unique pairs of protons. Figures 3.9 shows six representative HYSCORE spectra with simulated cross peaks for one of the unique couplings.

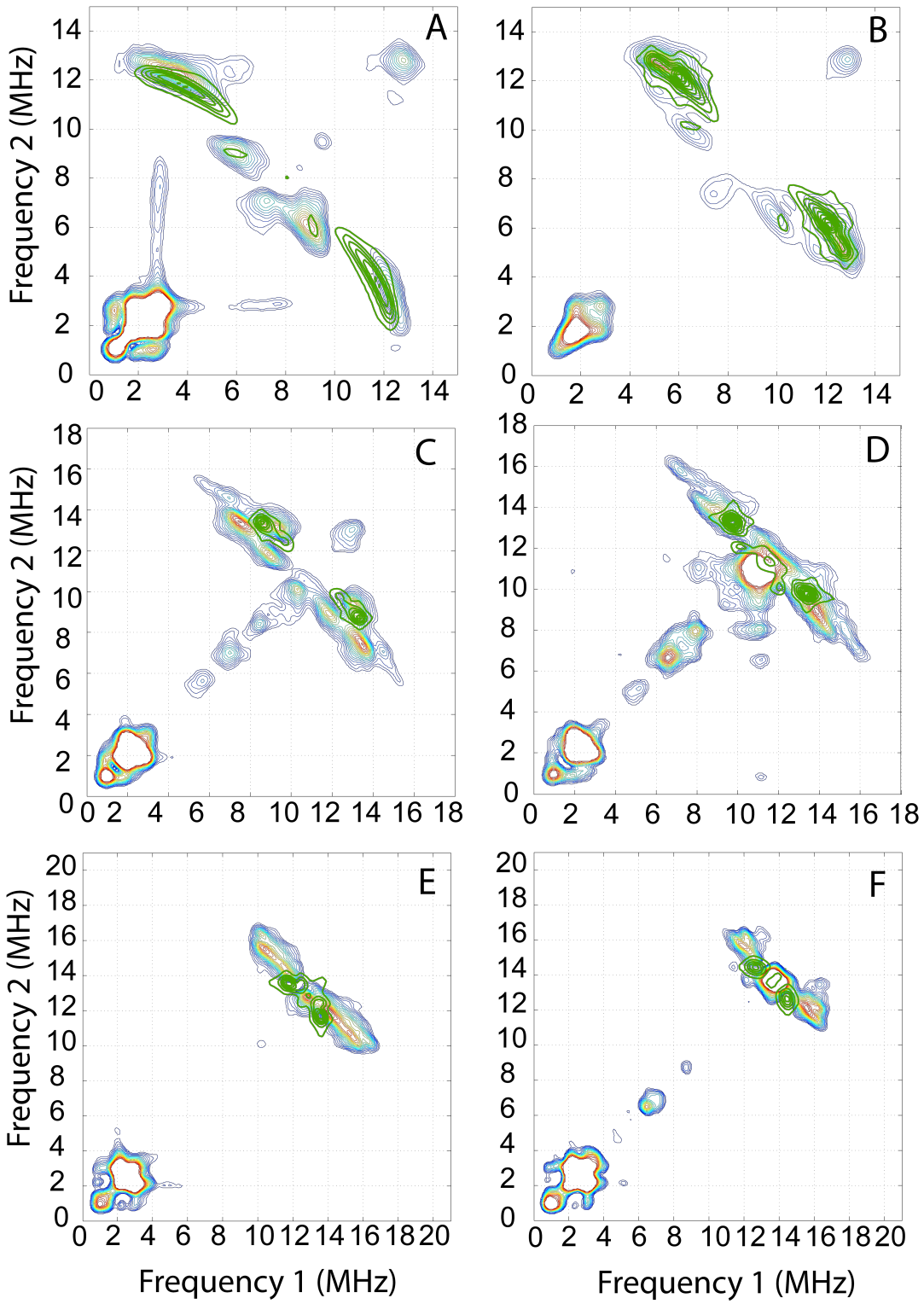

Figure 3.9. HYSCORE collected at (A) 170 mT. (B) 190 mT (C) 240 mT (D) 260 mT (E) 300 mT (F) 320 mT. The green represents the simulation of cross peaks with the parameters consistent with the protons on the equatorially coordinated His ligand: a_{iso}= 0.4 MHz, r=3.2 Å, and β_{HF}=90.8˚.

The broad arcing cross peaks near the intersection of ~3.5 MHz and ~12 MHz in Figure 3.9A (170 mT) that move to tight spots at the intersection of ~13 MHz and ~16 MHz in Figure 3.9F (320 mT) are characteristic of couplings with protons oriented nearly perpendicular to the principal axis of the ZFS (β_{HF}= ~90˚). This is consistent with the positions of the protons on the equatorially bound His ligand (His99 in Figure 3.1) predicted in the crystal structures 1GY9 and 1OS7 **(3, 4)**. The Hamiltonian parameters used to simulate these cross peaks are listed in Table 3.6. Figure 3.10 shows six representative HYSCORE spectra with simulated cross peaks for the other unique couplings.

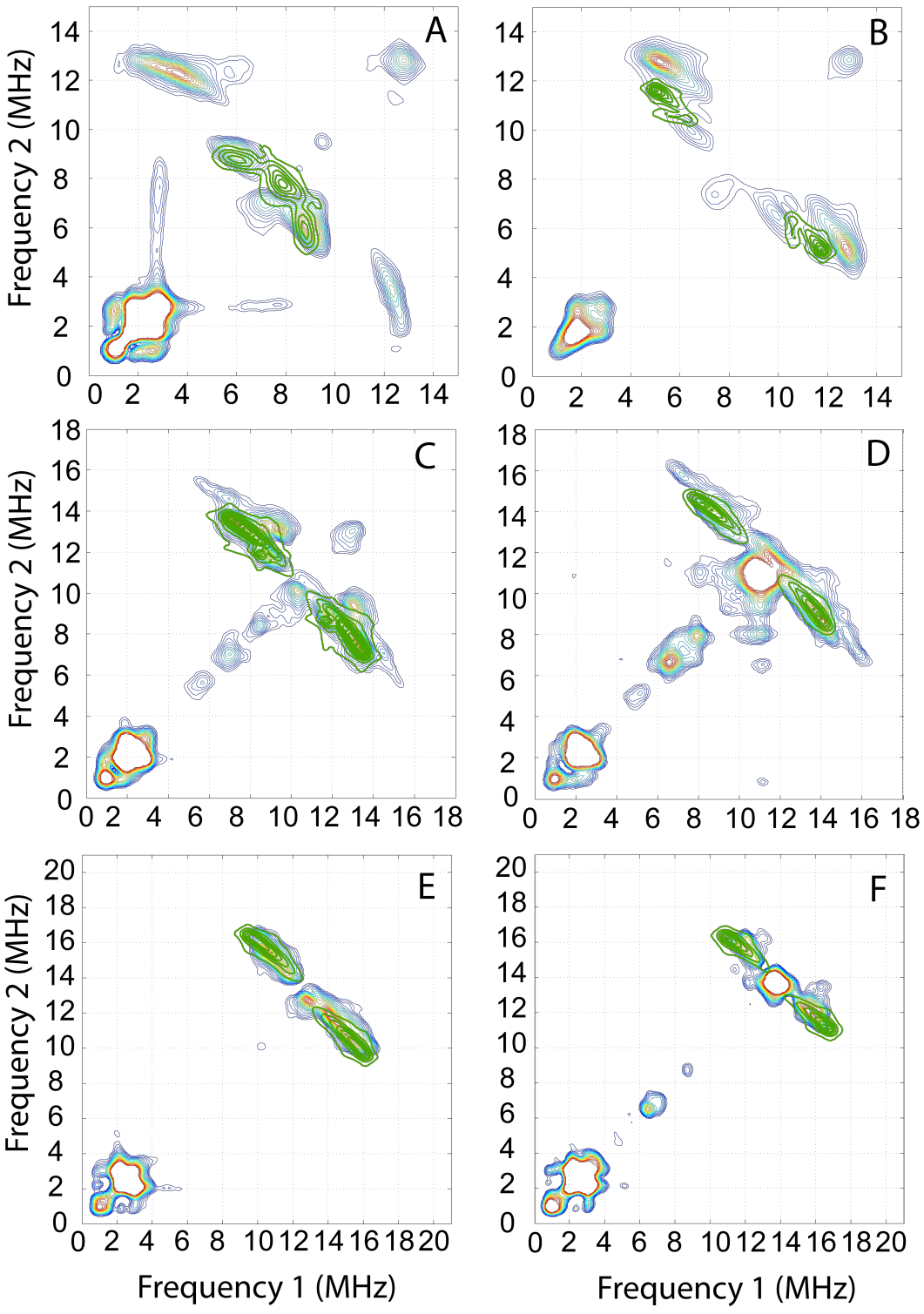

Figure 3.10. HYSCORE collected at (A) 170 mT. (B) 190 mT (C) 240 mT (D) 260 mT (E) 300 mT (F) 320 mT. The green represents the simulation of cross peaks with the parameters consistent with the protons on the axially coordinated His ligand: a_{iso}= 0.4 MHz, r=3.2 Å, and β_{HF}=140.5˚.

The shapes of the cross peaks near the intersection of ~6 MHz and ~9 MHz in Figure 3.10A (170 mT) that move to arcs near the intersection of ~12 MHz and ~16 MHz in Figure 3.10F (320 mT) are characteristic of weak isotropic coupling a_{iso}= ~0.4 MHz, a dipolar coupling of T= ~2.4 MHz, and β_{HF}= ~140˚. These measurements are consistent with the positions of the protons on the axially bound His ligand (His255 in Figure 3.1) predicted in the crystal structures 1GY9 and 1OS7 **(3, 4)**. The Hamiltonian parameters used to simulate these cross peaks are listed in Table 3.6. The protons on taurine are also expected to contribute to the HYSCORE. Figure 3.11 shows the simulation of cross peaks using parameters for the taurine protons consistent with the ^{2}H ESEEM measurements in Table 3.5.

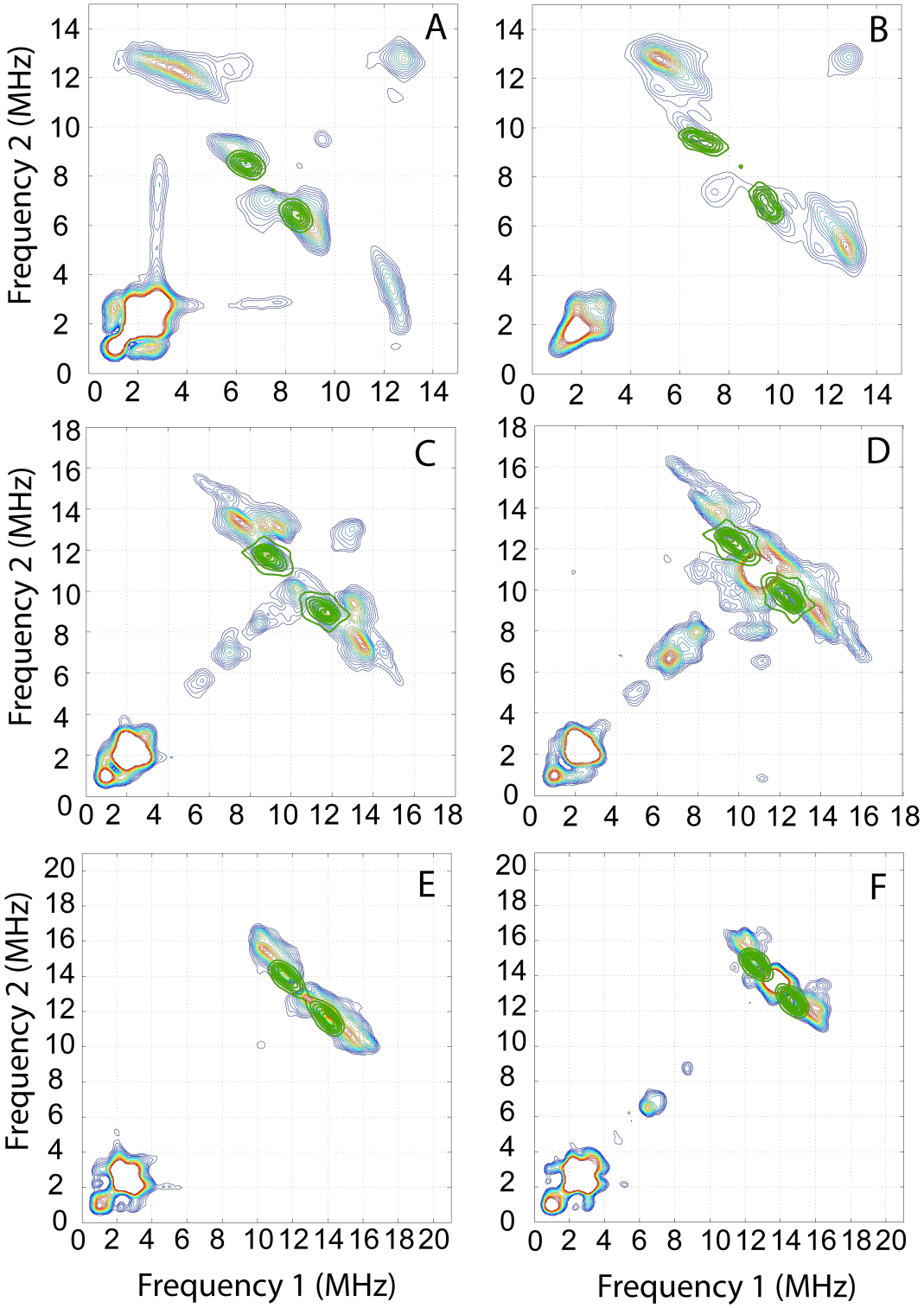

Figure 3.11. HYSCORE collected at (A) 170 mT. (B) 190 mT (C) 240 mT (D) 260 mT (E) 300 mT (F) 320 mT. The green represents the simulation of cross peaks with the parameters consistent with the protons on taurine: C1 ^{1}H - a_{iso}= 0 MHz, r=3.86 Å, and β_{HF}=26˚ and C2 ^{1}H - a_{iso}= 0 MHz, r=4.66 Å, and β_{HF}=37˚ (Table 3.5).

The cross peaks predicted with simulations using parameters consistent with taurine's protons are not clearly defined in the data. The expected positions of the cross peaks overlap with cross peaks owed to the axial His protons. Although some intensity in those areas of the spectra can be attributed to the taurine protons, the interactions with taurine's protons are not clearly resolved.

Table 3.5 lists the Hamiltonian parameters used to simulate the cross peaks in Figures 3.9, 3.10, and 3.11.

	Equatorial His protons	**Axial His protons**	**C1 ^{1}H**	**C2 ^{1}H**
a_{iso} (MHz)	0.4	0.4	0	0
r (Å)	3.2 , 3.4	3.3 , 3.4	3.86	4.66
β_{HF} (˚)	90.8	140.5	26.4	37.2

Table 3.5. When simulating the cross peaks owed to couplings with protons on the His ligands and taurine, three parameters were considered variable: The isotropic HF coupling constant (a_{iso}), the dipolar distance (r) relating the ^{1}H dipole to the spin center, and the angle relating the principal axis of the HFI tensor to the direction of the Fe-N(O) bond (β_{HF}).

The HYSCORE data collected at each of the 18 field positions can be visualized separately but are most instructive when visualized as a sum. Each spectrum is orientation selective but the set of spectra as a whole contains all orientations. Figure 3.12A-C are the result of adding spectra calculated at 18 different field values spanning the EPR spectrum. The sum spectra are labeled with the trajectory of the maximum amplitude of the corresponding experimental cross peaks (dashed line). Figure 3.12 is a graphical representation of the relative shapes of the corresponding experimental cross peaks.

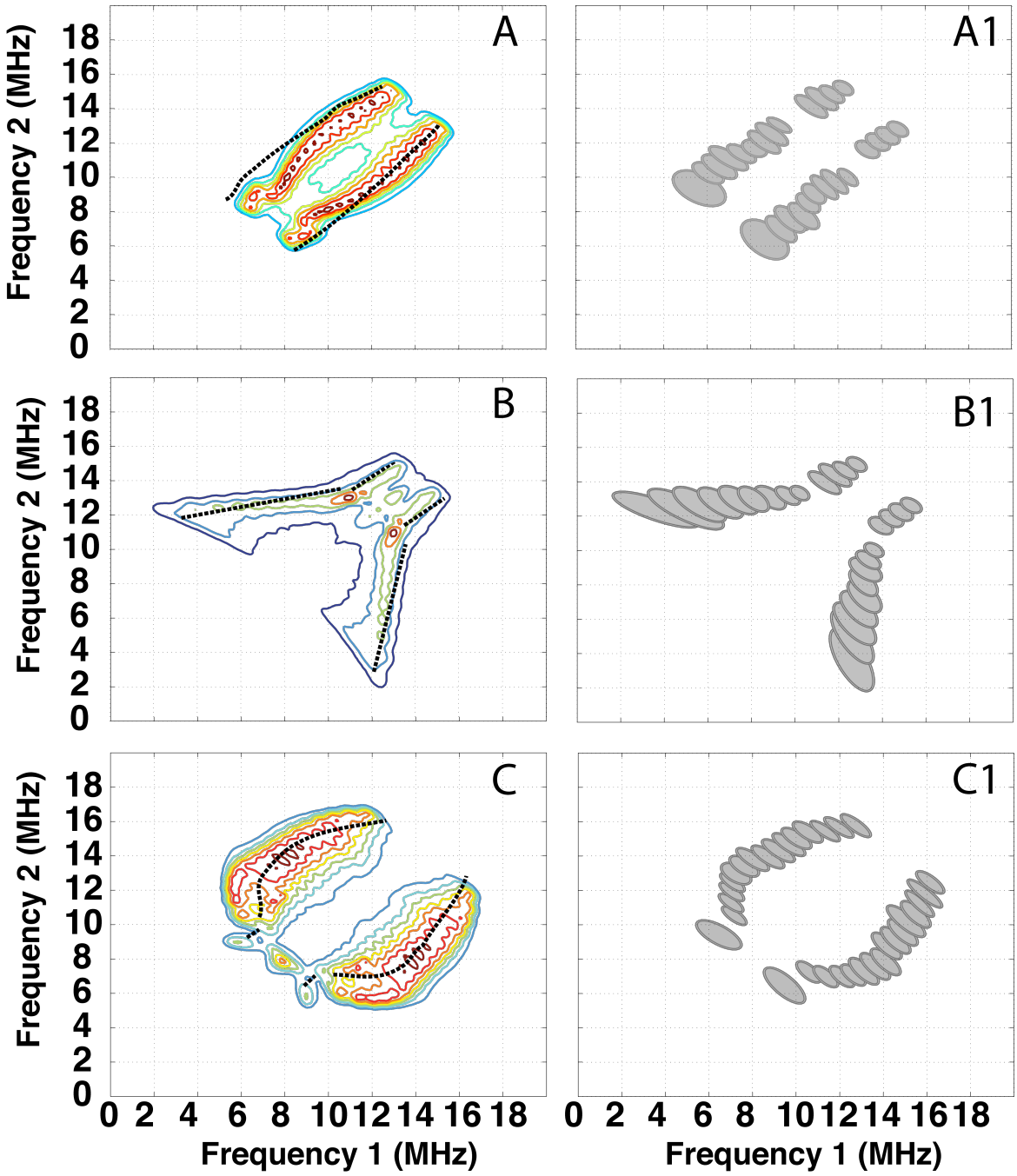

Figure 3.12. The results of adding HYSCORE spectra calculated for 18 different field positions (every 10 mT from 170 mT - 330 mT) is shown in A, B, and C for the parameters from Table 3.5 consistent with (A) the taurine protons, (B) the protons on the equatorially coordinated His ligand, and (C) the protons on the axially coordinated His ligands respectively. The dashed lines are the trajectory of the maximum amplitude of cross peaks in the experimental HYSCORE spectra across the 18 field positions. The pictures A1, B1, and C1 are derived from cross peaks in the experimental spectra. The sets of cross peaks that, when visualized over the 18 experimental spectra, formed the contours similar to the simulated contours.

The behavior of the cross peaks as a function of field strength is characteristic of the relative strengths of the isotropic (a_{iso}) and dipolar (T) HF couplings as well as the orientation of the $\boldsymbol{A}$ tensor with respect to the principal axes of the ZFS. The cross peaks centered at the frequency intersection of ~3.5 MHz and ~12 MHz in Figure 3.9A that move to spots near the intersection of ~13 MHz and ~16 MHz in Figure 3.9F were simulated as isotropic and dipolar coupling to two ^{1}H nuclei that are oriented perpendicular to the Fe-N(O) bond ($\beta_{HF} = 91^{\circ}$). In contrast, the tight spots in Figure 3.10A at the intersection of ~6 MHz and ~9 MHz that moved to broader arcs at the intersection of ~12 MHz and ~16 MHz in Figure 3.10F were simulated as isotropic and dipolar coupling to two protons oriented at $\beta_{HF} = 140^{\circ}$ from the Fe-N(O) bond. These two sets of protons that have similar isotropic and dipolar coupling strengths but have dipolar vectors that are approximately 50˚ out of plane from each other are the protons on the equatorially and axially bound His ligands of the "facial triad" **(28)**. Simulation of HYSCORE spectra using the positions of taurine's protons predicted by the ^{2}H ESEEM findings produce cross peaks that start at the intersection of ~7 MHz and ~9 MHz in Figure 3.11A and move to the intersection of ~13 MHz and ~15 MHz in Figure 3.11F. The cross peaks owed to the taurine protons overlap with the cross peaks from the His protons at many field positions but the trajectories and shapes of the cross peaks shown in Figure 3.12A and 3.12C can allow for distinction of the two sets of couplings. Figure 3.13 shows comparisons of three spectra for the samples having protons on taurine with the spectra for the samples having deuterons on taurine.

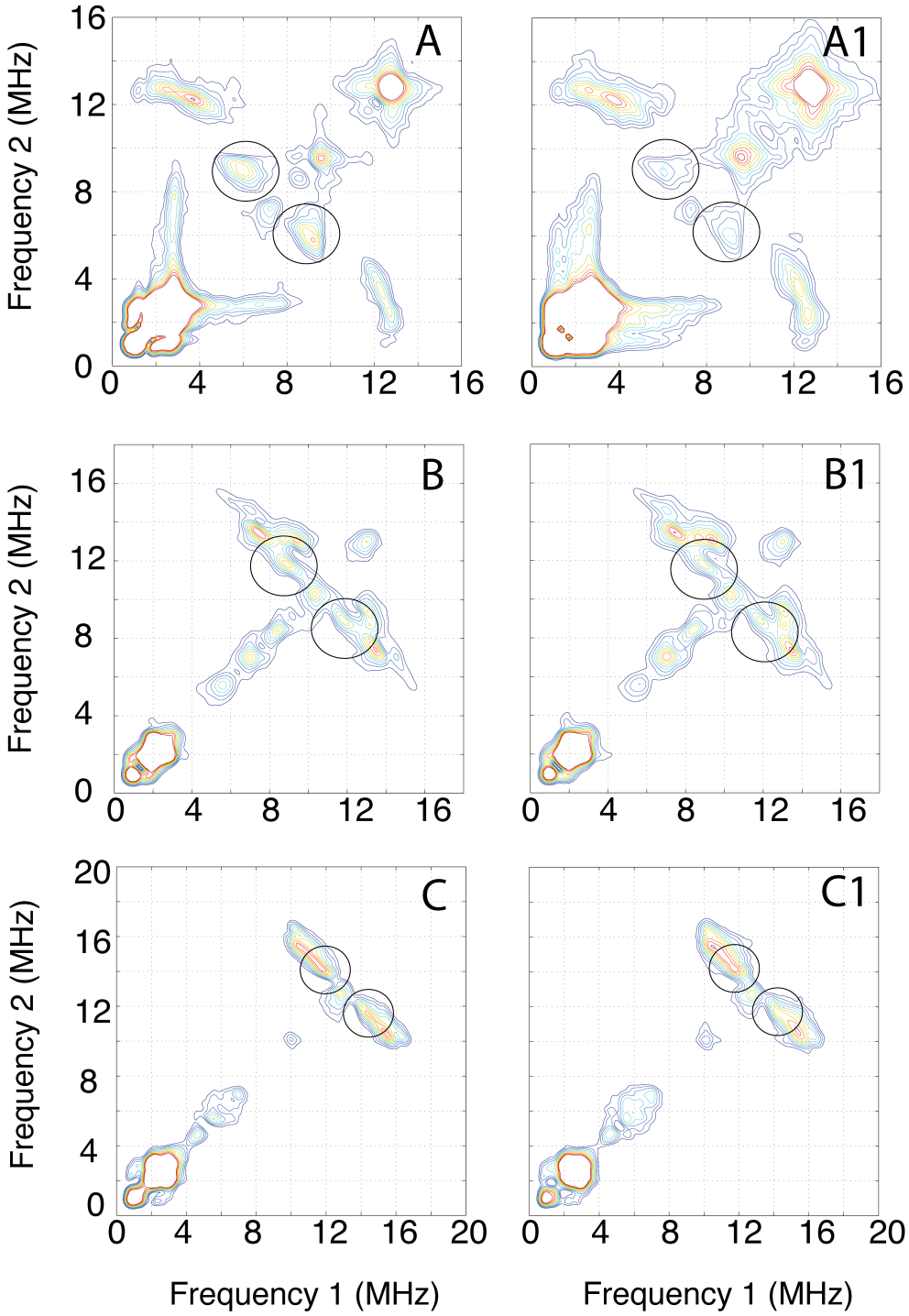

Figure 3.13. HYSCORE spectra collected for the TauD samples having [^{1}H]-taurine at (A) 170 mT (B) 240 mT and (C) 300 mT. The corresponding spectra in A1, B1 and C1 were collected for the TauD samples having C1,C2-[^{2}H]-taurine (A1) 170 mT (B1) 240 mT and (C1) 300 mT. A unique set of cross peaks that could be attributed to the protons on taurine did not vanish but intensity in the spectral regions where the cross peaks are expected was slightly less.

Spectra collected for the TauD samples having the C1 and C2 protons on taurine replaced with deuterons show only a slight decrease in intensity of the cross peaks in the positions where the taurine ^{1}H couplings would be.

HYSCORE spectra were also collected at six field positions for the TauD samples that were missing taurine and α-KG. Figure 3.14 shows the comparison of three spectra for the sample having taurine and α-KG with spectra for the sample missing taurine.

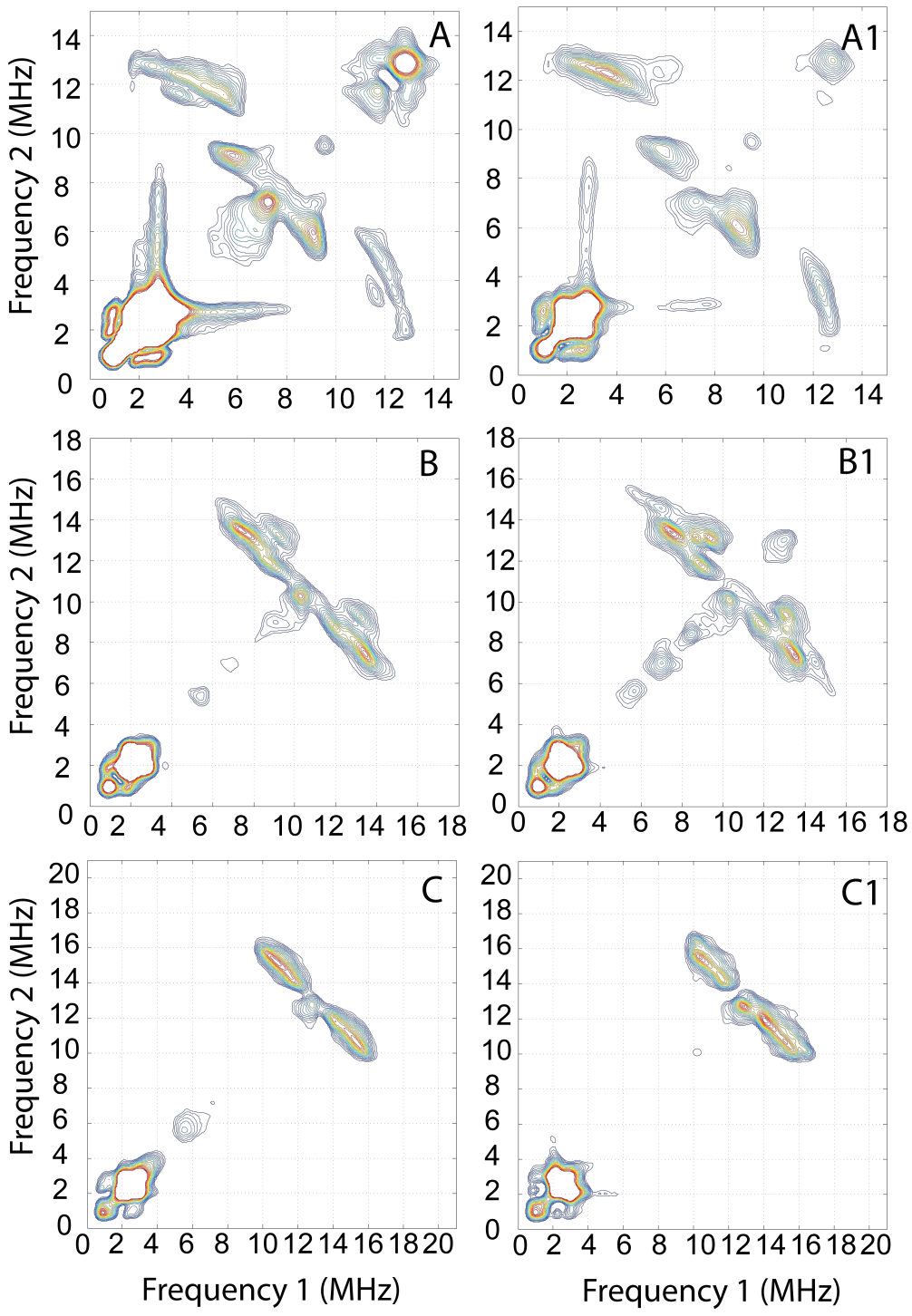

Figure 3.14. HYSCORE collected at (A) 170 mT. (B) 240 mT (C) 300 mT for the TauD sample having α-KG but missing taurine. The corresponding A1, B1, and C1 spectra were also collected at (A1) 170 mT (B1) 240 mT and (C1) 300 mT for the TauD sample having α-KG and taurine. Unique cross peaks that could be attributed to the taurine protons did not vanish but slightly enhanced dispersion of the cross peaks suggests a slight conformational flexibility in the absence of taurine.

The cross peak positions are nearly identical but the distribution of intensity throughout the area of the cross peaks is enhanced when taurine is missing. This is the result of slight conformational flexibility that is afforded when taurine is not present allowing for a slight variability in the position and orientation of the coordinated ligands. Figure 3.15 shows the comparison of the spectra for the sample having taurine and α-KG with the spectra for the sample missing α-KG.

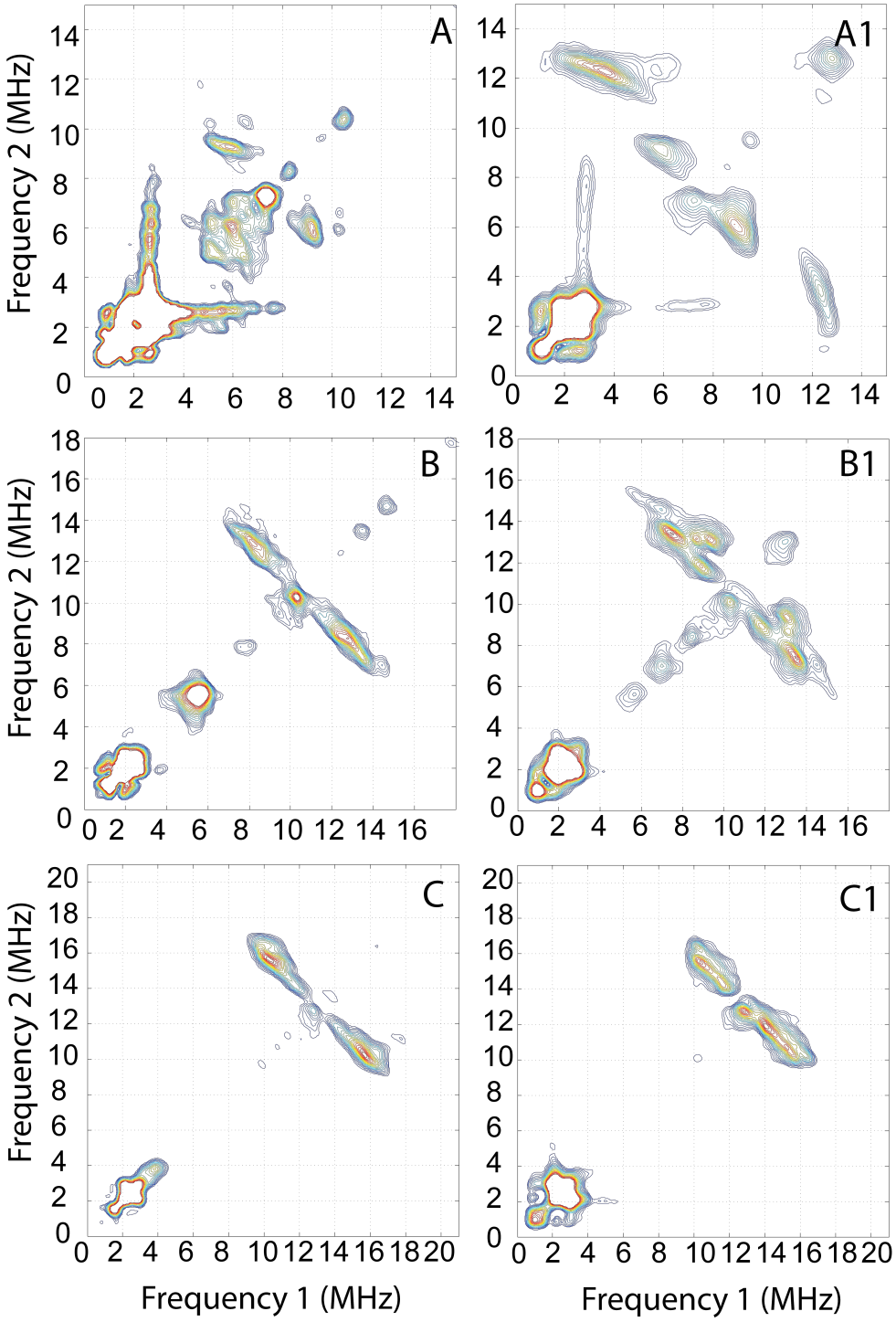

Figure 3.15. HYSCORE collected at (A) 170 mT. (B) 240 mT (C) 300 mT for the TauD sample having taurine but missing α-KG. The corresponding A1, B1, and C1 spectra were also collected at (A1) 170 mT (B1) 240 mT and (C1) 300 mT but for the TauD sample having taurine and α-KG. The disappearance of broad arcs in (A) and intensity of certain cross peaks in (B) and (C) that correspond to equatorially positioned protons suggests a significant alteration of the equatorial coordination when α-KG is missing.

The consistent loss of cross peaks owed to the couplings with protons that are oriented roughly perpendicular to the Fe-N(O) bond suggests that the direction of the bond relative to the orientations of the coordinated His ligands in the complex is variable when α-KG is not present. The effects are most noticeable in the spectra collected at the lower field positions where orientations perpendicular to the Fe-N(O) bond are being observed. The implications of this will be covered in the discussion section.

Optimization of 1GY9. Avogadro software **(26)** predicted a new position of taurine in the 1GY9 crystal structure. Figure 3.16 shows a picture of the TauD active site as predicted by UF optimization in Avogadro.

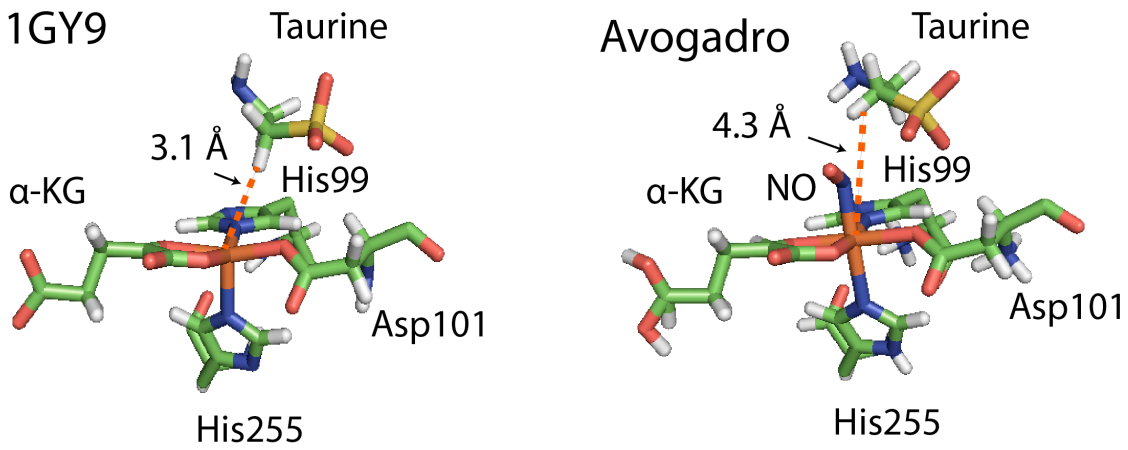

Figure 3.16. The Avogadro software uses Unified Field (UF) theory to position the NO and taurine in the most energy optimized position in the TauD active site. During the optimization the residues that encompass the substrate binding pocket are included but have been omitted in these pictures for easier visualization of the taurine and NO positions.

This optimization includes the coordinated NO. The position of taurine is moved away from the $\{FeNO\}^7$ complex as compared to the 1GY9 crystal structure. The NO may play a role in this

but, importantly, the optimization is also accounting for interactions with protein contacts that stabilize the taurine in the functioning enzyme. With the NO included the angles relating the position of the protons to the direction of the Fe-N(O) bond can also be estimated to compare with the ESEEM and HYSCORE measurements that are also referenced to the Fe-N(O) bond (See chapter 2.1). The taurine position generated by Avogadro will be presented in the discussion of the ESEEM results for comparison.

3.5 DISCUSSION

CW EPR. The CW EPR spectra for TauD samples represent an axial ZFS and a single binding mode for NO. When either taurine or α-KG are not present the additional broadening of the line is likely the result of a slight variability in NO binding allowed by a slight variability in the coordination arrangement. Any significantly different NO binding modes would likely have resulted in a measurable broadening or even splitting of the $g_{\perp}$=4 feature due to deviations in *E/D* **(8, 29)**. This suggests that a small degree of orientation flexibility is allowed but the most energetically favorable binding of NO remains the same even without α-KG or taurine. The EPR spectrum for the sample missing both α-KG and taurine also shows a single species lending to the assertion that TauD maintains a highly favored single binding mode for NO regardless of taurine and α-KG **(8, 30)**. Interestingly, the HYSCORE data suggest a significant change in the relative coordination of the NO ligand to the equatorially bound His ligand when α-KG is not present (Figure 3.15). This could mean that the binding "mode" for NO may not be synonymous with the "position" of NO in the coordination arrangement. Based on the previous study by Ye et al. **(8)**, the "mode" as it is discussed here would describe the relative projection of the N=O bond

in the complex while the "position" would be in reference to the specific ligand that is coordinated trans to the bound NO. When α-KG is present, the "in line" arrangement of TauD **(1, 3, 4, 8)** forces a single position for NO binding that is trans to His255 and cis to His99. When α-KG is not present, there are two positions for NO to bind that would result in the Fe-N(O) bond being oriented trans to one His ligand, cis to the other His ligand, and cis to the Asp ligand. Because the electronic structure of the $\{FeNO\}^7$ complex may depend only on the relative ligand arrangements **(8, 30)**, the CW EPR may not be sensitive to the exact position of NO as long as the relative ligand arrangements remain the same. The HYSCORE, on the other hand, would be sensitive to the different "positions" of NO because the protons on the equatorial His ligand will now have a different relationship to the Fe-N(O) bond and, because the Fe-N(O) bond defines the principal axis of the ZFS, the β_{HF} angles will assume new values for these couplings. The CW EPR data alone may only suggest that the NO is bound in the "mode" that has it trans to one of the His ligands regardless of the exact position in the complex. Without HYSCORE, only the suggested relative "modes" of NO binding are discernible but not the exact "positions."

Deuterium ESEEM. The previous study by Muthukumaran et al. **(19)** measured the position of the C1 and C2 deuterons and the orientation of the taurine molecule near the $\{FeNO\}^7$ complex of TauD by manually fitting line shapes in ESEEM ratio spectra collected at four field positions. Two spectra were located near the $g_{\perp}$=4 and two near the $g_{\parallel}$=2 region of the EPR spectrum. The study used a model identical to the one described in an ENDOR study by Yang et al. **(31)** to measure the distance between an electron dipole located at the Fe of the $\{FeNO\}^7$ complex and nearby ^2H dipoles. Tensor orientations were used to position the ^2H in relation to the magnetic

axes of the $\{FeNO\}^7$ complex by calculating effective g values to weight the HFI and NQI tensor components. Euler angles translated the tensor orientation to the principal axis system that was defined by the effective g tensor. The principal axis of the g tensor was assumed to be near coincident with the Fe-N(O) bond. The measurements were generally consistent with the crystal structures for TauD **(3, 4)**. However, by fitting only line shapes in the ESEEM spectra, measurement of the dipolar distance (*r*) and the orientation of the ***A*** tensor can be unreliable. The frequency amplitudes are strongly correlated to the strength of the dipolar coupling and the projection of the ***A*** tensor in the principal axis system, two key descriptors of the structural relationship between the ^2H dipole and the spin center. The profile of frequency amplitudes as a function of the orientation of the spin system provides a complete analysis of the ***A*** tensor orientation. In addition, the manual modeling of the position of NO and assumptions made for the optimum positioning of taurine that were used to put the ESEEM results in the context of crystallography are not directly supported with experimental data. The orientation of NO in the complex is important because it provides the axes of reference for the tensor orientations measured with ESEEM (See chapter 2).

In the present study, the positions of taurine and NO in the 1GY9 crystal structure that was used for comparison **(3)** were energy optimized using Avogadro software **(26)** (Figure 3.16). The estimated orientation of NO used for comparison is supported by energy optimization. It is convenient for this study that the theoretical findings of Ye et al. **(8)** and Aquino and Rodriguez **(25)** that were not available for the previous ESEEM study by Muthukumaran et al. have since been reported and the predictions made using Avogadro are consistent. In performing the optimization of 1GY9, the assumption that the crystal structure's prediction of the protein

structure and the position of Fe is accurate while taurine's position is not can be assumed because of similarity of protein arrangement between multiple TauD structures where the taurine position differs **(3, 4)**. Also, high resolution crystal structures for other enzymes in the non-heme Fe(II)/α-KG dependent enzyme family **(6)** show similar Fe(II) coordination and active site protein arrangements. For the ESEEM analysis, instead of using effective g values, the actual S=3/2 spin system with large ZFS (~10 cm^{-1}) was considered as the reference for interactions with the ^{2}H nuclei. Spectra were collected at enough field positions to observe all orientations of the spin system and the complete profile of the frequency amplitudes were fit with a heuristic searching algorithm that compared the entire data set to calculated simulations in parallel. This not only provides efficient and complete correlation of line shapes and amplitudes to the Hamiltonian parameters that describe the HFI and NQI but provides statistical support for the "best" set of parameters.

To measure the distance of the ^{2}H from the $\{FeNO\}^{7}$ complex using ESEEM the analysis can be simplified by the point dipole approximation **(31)** in which the unpaired electrons are localized to a single point in the complex. The distances measured in the crystal structures are in relation to the Fe center while the EPR measurements are in reference to the actual spin center. As discussed in chapter 2, multiple studies suggest a degree of delocalization of unpaired spin across the Fe-N(O) bond. This means that the point dipole approximation is not entirely accurate and spin projection considerations may be necessary. Considering this, when interpreting the ESEEM measurements it should be noted that the measurement may be referenced to an average position of the unpaired spin across the Fe-N=O moiety. Figure 3.17 illustrates the Avogadro

optimized crystal structure with ^{1}H measurements now referenced to the N in addition to the Fe center.

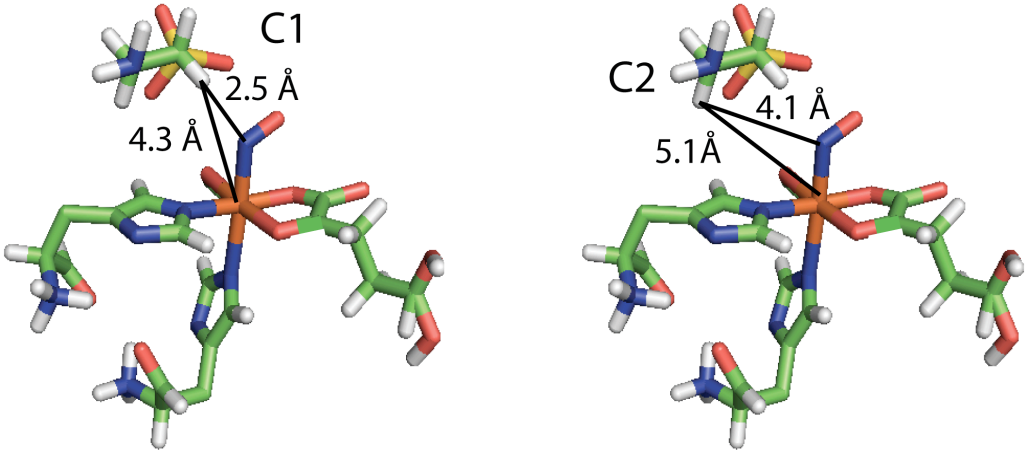

Figure 3.17. The unpaired spin density in the $\{FeNO\}^{7}$ complex is not localized at the Fe center. The actual distance measurements for the C1 (3.86 Å) and C2 (4.66 Å) deuterons made with ESEEM are slightly shorter than the ^{1}H-Fe distances but longer than the ^{1}H-N distances.

If the actual spin center is localized somewhere between the Fe and N **(8, 29)**, the distances measured with ESEEM (3.86 Å for the C1 ^{2}H and 4.66 Å for the C2 ^{2}H) would be an effective distances to a point between the Fe and N. The β_{HF} angles would take on a new meaning as well. Moving the spin center toward the N would increase the effective β_{HF} measured with ESEEM. The simple electronic structure model for the TauD $\{FeNO\}^{7}$ complex in Figure 2.1 was derived from studies by the Solomon group **(29)** and was corroborated by Neese and coworkers **(8)**. This model suggest that the d_{xy}, $d_{x^2-y^2}$, and d_{z^2} orbitals contain the unpaired spins and the unpaired spin density is suggested to favor the Fe. By localizing a point dipole approximately at the Fe

center, analysis of the data is greatly simplified and may introduce only minor discrepancies with the ESEEM results. Figure 3.18 offers a picture of taurine's position relative to the $\{FeNO\}^7$ complex of TauD predicted by ESEEM compared with the structure predicted with the Avogadro software.

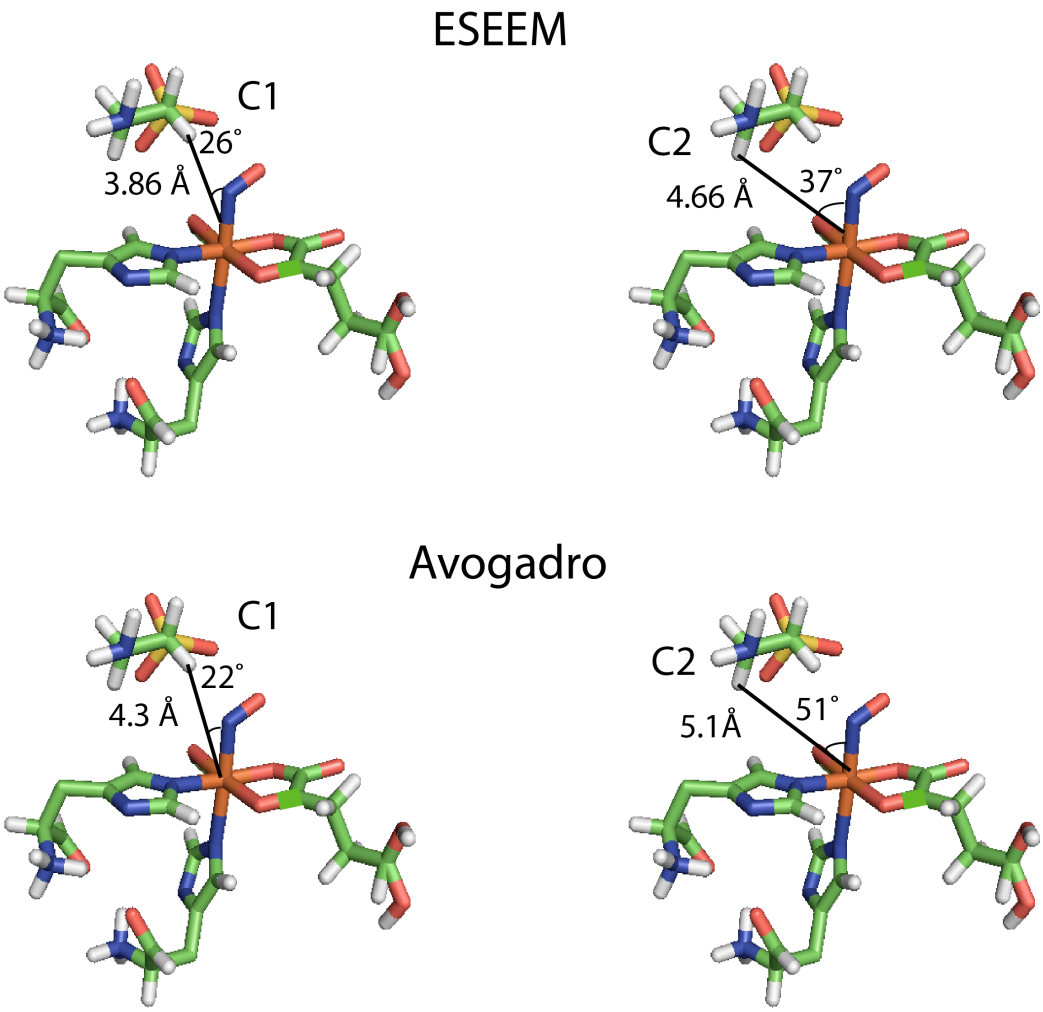

Figure 3.18. The distance measured by ESEEM is shown as an average location between the Fe and N because of delocalization of the unpaired spin density across the Fe-N=O moiety while the measurements in the Avogadro structures are referenced to the Fe.

The ESEEM measurements pictured in Figure 3.17 and summarized in Tables 3.2 and 3.4 were consistent with couplings to a single ^{2}H at each of the C1 and C2 positions. This is presumably because the orientation of the taurine makes for the positioning of the second deuterons at least 1 Å further from the spin center and roughly behind the taurine molecule with respect to the $\{FeNO\}^7$ complex. Because ESEEM amplitudes decay as ~ $1/r^6$, if there is any interaction with the second ^{2}H it would have a negligible contribution to the spectrum on the order of the observed peak amplitudes.

Measurement of the NQI tensor orientations gives the direction of the ^{2}H-C1 and ^{2}H-C2 bonds and allows for the inference of the orientation of the taurine molecule. The magnitude of e^2qQ/h (~0.22 MHz) measured in this study generally agrees with the previous study by Muthukumaran et al. **(19)** but the predicted tensor orientations are different. In their study the γ_{NQI} was not included in the fitting procedure. In the present study, the γ_{NQI} was allowed to vary in the fitting procedure for the reasons described above. Statistical analysis of the parameter set reported in the previous study for the C1 ^{2}H [r=3.4 Å, β_{HF} =17˚, e^2qQ/h=0.20 MHz, β_{NQI} =23˚, γ_{NQI} =0˚] where the γ_{NQI} was not considered gives a ratio of χ^2 to the χ^2 for the "best" parameter set in this study of 4.1. The same analysis of the parameter set reported in the previous study for the C2 ^{2}H [r=4.5 Å, β_{HF} =63˚, e^2qQ/h=0.20 MHz, β_{NQI} =23˚, γ_{NQI} =0˚] gives a ratio of χ^2 to the χ^2 for the "best" parameter set in this study of 3.3. However, although statistically supported, the β_{NQI} of 106˚ for the C2 ^{2}H and the γ_{NQI} of 155˚ for the C1 ^{2}H predicted in this

study do not agree visually with the Avogadro optimized crystal structure. Any β_{HF}, β_{NQI} or γ_{NQI} discrepancies can be rationalized by recognizing that the β_{HF}, β_{NQI}, or γ_{NQI} angles have inversion symmetry in the calculations. Figure 3.19 is a drawing that illustrates the inversion symmetry in the β_{HF}, β_{NQI}, and γ_{NQI} angles in the three dimensional (3D) space surrounding the $\{FeNO\}^7$ complex.

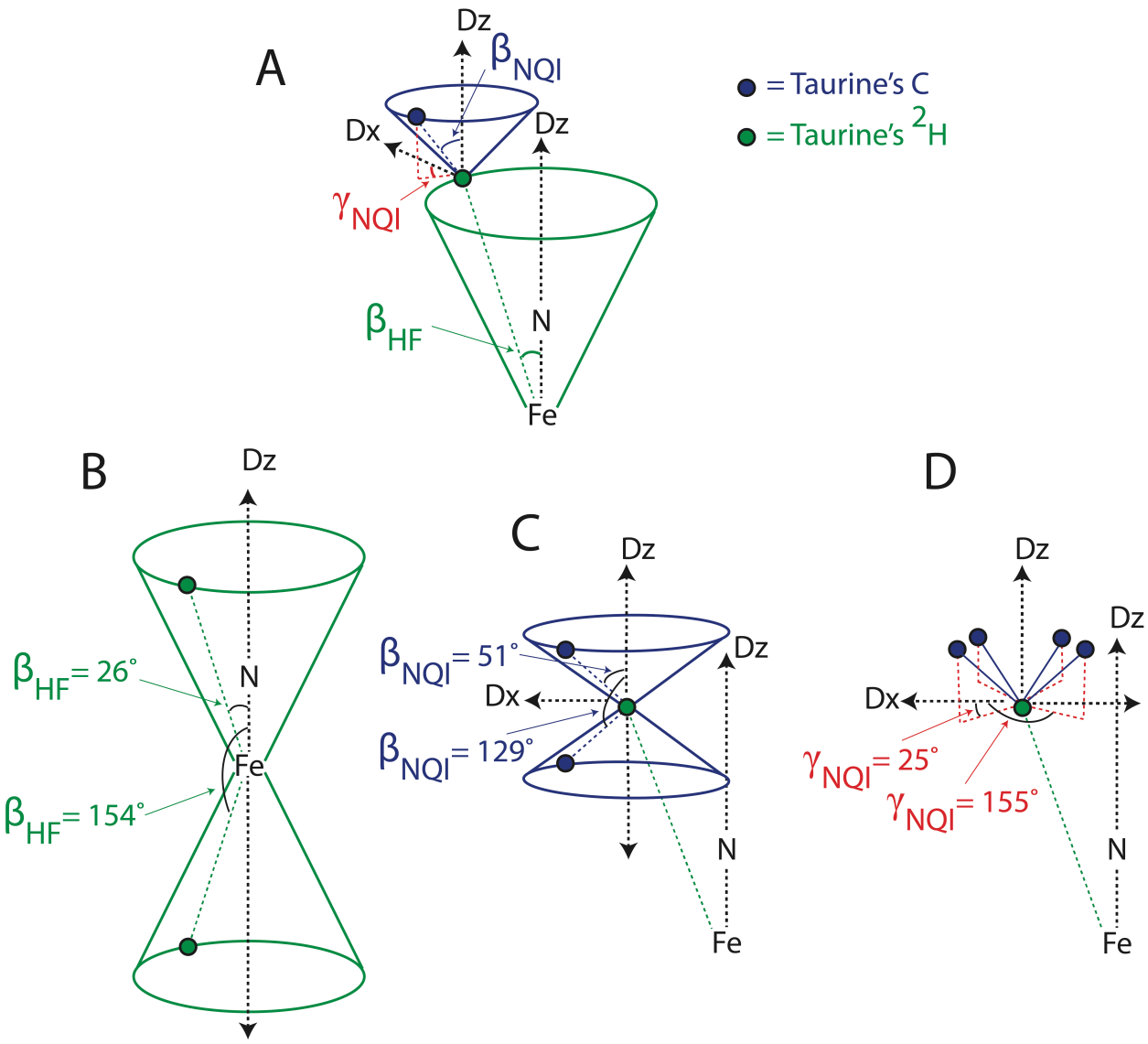

Figure 3.19. The picture labeled A is Figure 3.3 for reference. Pictures B and C illustrate the inversion symmetry for the β_{HF}, β_{NQI} angles for the ^{2}H-C1 bond, respectively, measured with ESEEM. B and C display the 3D space surrounding their inversion centers: Fe for the β_{HF} and ^{2}H for β_{NQI}. Picture D shows 4 of the 8 equivalent γ_{NQI} angles that would reduce the blue cones in C to a limited set of orientations. When visualizing the actual spacial position of the ^{2}H and C1 in the 3D model, any combination of the available β_{HF}, β_{NQI}, and γ_{NQI} angles and their inversion angles would result in the same calculated ESEEM spectrum.

This means that if the inversion angles are not considered unique (i.e. 26˚ = 154˚, 51˚=129˚, and 25˚ =155˚) and with the γ_{HF} angles indistinguishable (ZFS is axial, See Figure 3.3), the β_{HFI} angle can represent any of the unique spacial positions on the green cones in Figure 3.19B either above or below the $\{FeNO\}^7$ complex that result in the same relative angle of the principal axis of the ***A*** tensor to the principal axis of the ZFS tensor. Similarly, when the NQI and HFI are axial, the β_{NQI} angle can represent any of the unique projections of taurine's ^{2}H-C bond directed either away or toward the perpendicular plane of the ZFS tensor (blue cones in Figure 3.19C). By defining the γNQI angle, the cone of indistinguishable projections of the ^{2}H-C1 bond in Figure 3.19C is reduced to 8 indistinguishable positions at any possible projection of the ***A*** tensor (4 toward and 4 away from the perpendicular plane of the ZFS tensor. For visual aid, γ_{NQI}=0 is the same projection of the ^{2}H-C bond on the perpendicular plane of the ZFS tensor as that of the principal axis of the ***A*** tensor.) Any mixture of the complementary angle pairs will result in the same calculated spectra and fitting algorithms can pursue any given angle pair. A similar χ^2 value belongs to the parameter set in Table 3.1 that has this reflected γ_{NQI} angle. That they are not the same is simply a result of less than perfect precision of the complex calculation performed by MATLAB. Because the disparity between the reflected spacial positions is not apparent in the calculated χ^2, the fitting algorithm can choose any of the angle combinations with equal probabilities and easily decide on any of the combinations of angles as the "best" choice.

For convenience, the β_{HF} and β_{NQI} angles can be restricted to defining the quadrant above the $\{FeNO\}^7$ complex because it can be assumed that taurine is most likely bound in the

substrate pocket above the NO on the basis of previous structural data **(3, 4)** and intuition in the context of the mechanism. Figure 3.20 illustrates the logical ranges of Euler angles in the context of previous structural data and the mechanism with the inversion angles now defined as unique (i.e. 26˚ ≠ 154˚, 51˚ ≠ 129˚, and 25˚ ≠ 155˚) for ease of visualization.

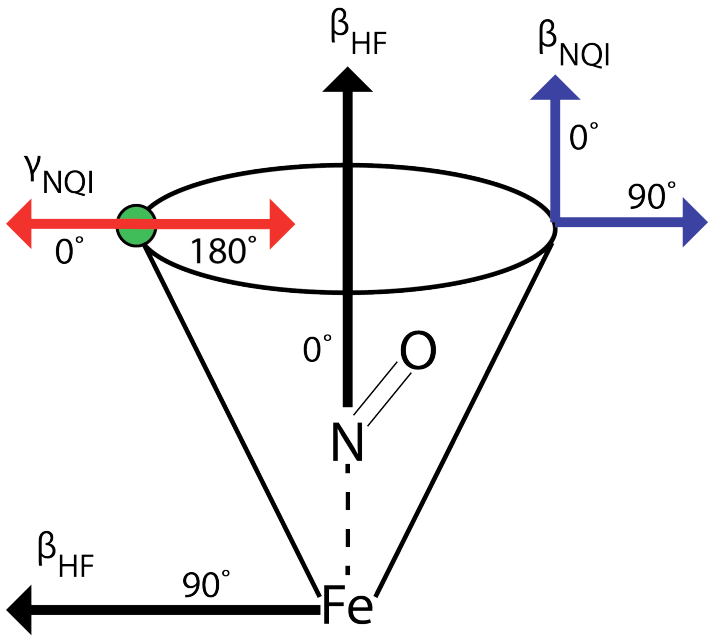

Figure 3.20. Because taurine is bound in the substrate pocket above the NO, any β_{HF} angle is interpreted as defining ^{2}H positions above the $\{FeNO\}^{7}$ complex. The direction of the principal axis of the NQI tensors is toward the taurine carbons along the ^{2}H-C1 and ^{2}H-C2 bonds so the β_{NQI} angle are interpreted as placing the taurine molecule above the NO as opposed to beside it. The relative orientations of the NQI and HFI tensors described by the γ_{NQI} angle can be anywhere between 0˚ and 180˚ while still maintaining a logical position for taurine.

With this assumption, inversion of β_{NQI} would place the taurine directly beside the NO, both of which are not likely for proper function of the enzyme. This restricts the physical meaning of the β_{HF} and β_{NQI} to between 0˚ and 90˚ in Figure 3.20. The γ_{NQI} angle can still describe any projection ranging from towards the Fe-N(O) bond to away from it without completely

redefining taurine's position so any of the complementary angles corresponding to β_{NQI} angles between 0˚ and 90˚ in Figure 3.19D are still equally probable. Reflection of the "best" γ_{NQI} from Table 3.1 through the ^{2}H to direct the ^{2}H-C1 bond at γ_{NQI} = 25˚ instead of 155˚ results in a different spacial relationship but the same relative angle between the NQI and HFI tensors. While the restriction of the ^{2}H-C1 bond to orientations pointed away from the NO (0˚-90˚ in Figure 3.22) is applied to place the taurine molecule in the most logical position for proper function of the enzyme, the same restriction cannot simultaneously apply for the ^{2}H-C2 bond. The β_{NQI} and γ_{NQI} for the ^{2}H-C2 bond are likely complementary in nature to the β_{NQI} and γ_{NQI} for the ^{2}H-C1 bond if the normal staggered geometry of the C-H bonds is considered for the molecular shape of taurine (this is illustrated by any depiction of the taurine molecule in the previous figures). This means that if the ^{2}H-C1 bond is directed between 0˚ and 90˚, it is likely the β_{NQI} of the ^{2}H-C2 bond is directed between 90˚ and 180˚. With this interpretation of the β_{HF} and β_{NQI} angles the description of the orientation of taurine using the NQI Euler angles is greatly simplified but exact spacial descriptions using the angle pairs measured with ESEEM are still subject to multiple interpretations. The exact definitions of the angles can only be assumed. To visually reconcile taurine's orientation using these considerations, selection of the angle pair of β_{NQI} = 86˚ and γ_{NQI} = 143˚ for the ^{2}H-C2 bond is most likely to coincide with the suggested angle pair of β_{NQI} = 51˚ and γ_{NQI} = 25˚ for the ^{2}H-C1 bond. Figure 3.21 illustrates the two angle pairs put together in a drawing of taurine's position relative to the Fe-N(O) bond using the assumed definition of the Euler angles.

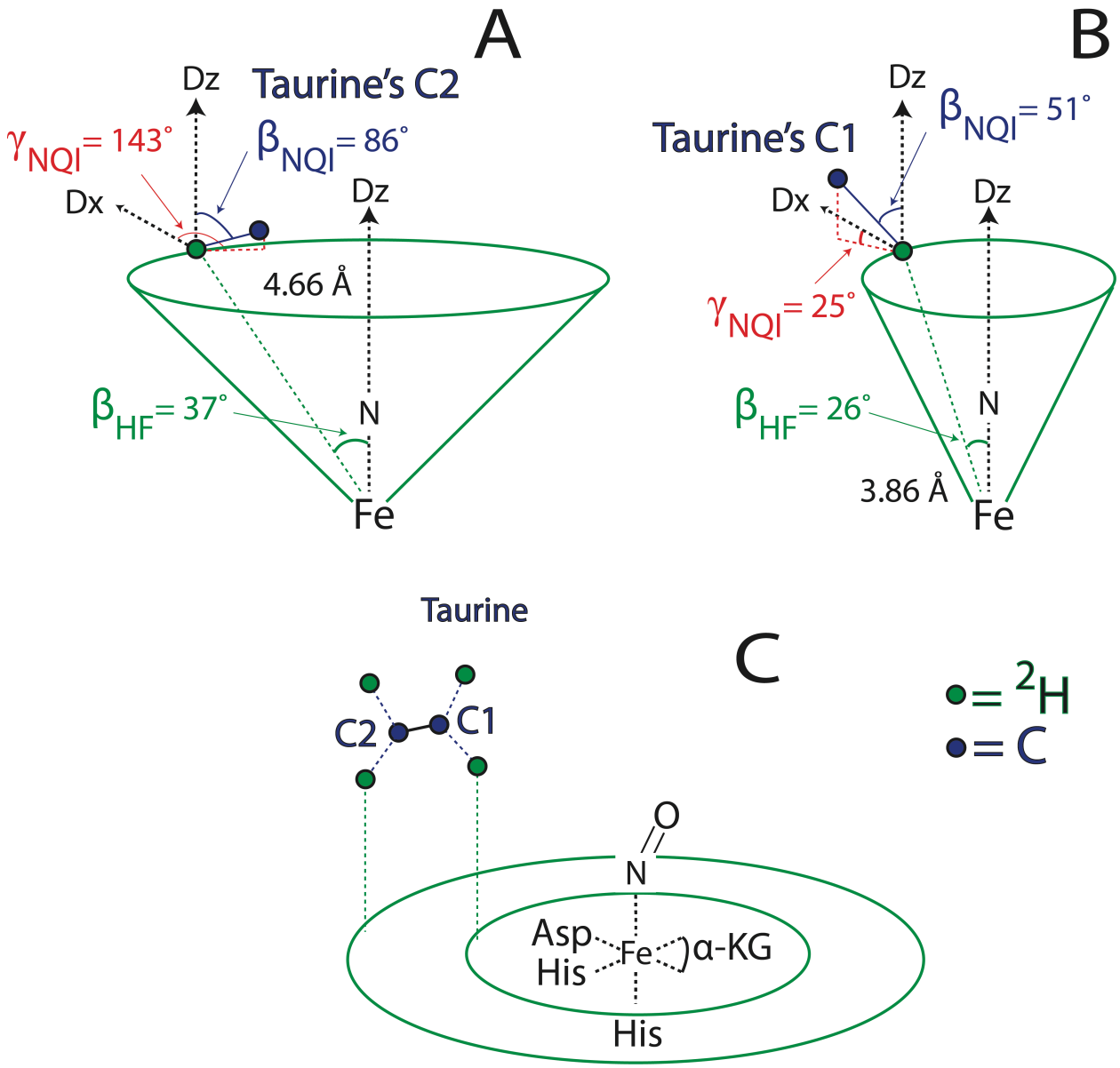

Figure 3.21. (A) The representation of the Euler angles describing the orientation of the ^{2}H-C2 bond. (B) The representation of the Euler angles describing the orientation of the ^{2}H-C1 bond. (C) A visual aid for imagining the relationship of the C1-C2 unit of taurine to the $\{FeNO\}^{7}$ complex using the ESEEM measurements that are represented in (A) and (B).

The confidence intervals for the parameters (Tables 3.2 and 3.4) indicate that measurements of the NQI parameters are the least certain while the HFI parameters can be reasonably trusted. The shapes and line widths in the ratio spectra are subject to more error from the division process than the amplitudes of the primary frequency because of less than perfect frequency precision in ESEEM experiments (see text following Table 3.2 on page 64). Since the HFI parameters contribute most to the amplitudes of the primary frequency peaks and NQI parameters contribute most to the width and shapes of the peaks (see Figure 2.12), less certainty in the NQI parameters is expected when extracting these parameters from ratio ESEEM spectra.

To assess the implications of the Avogadro results it can be considered that the ^{1}H-C1 and ^{1}H-C2 bond orientations can be reversed in the optimization of the crystal structure with little effect on the calculated energy. Figure 3.22 shows two Avogadro optimized orientations of the ^{1}H-C1 and ^{1}H-C2 bonds that resulted in the same calculated energy.

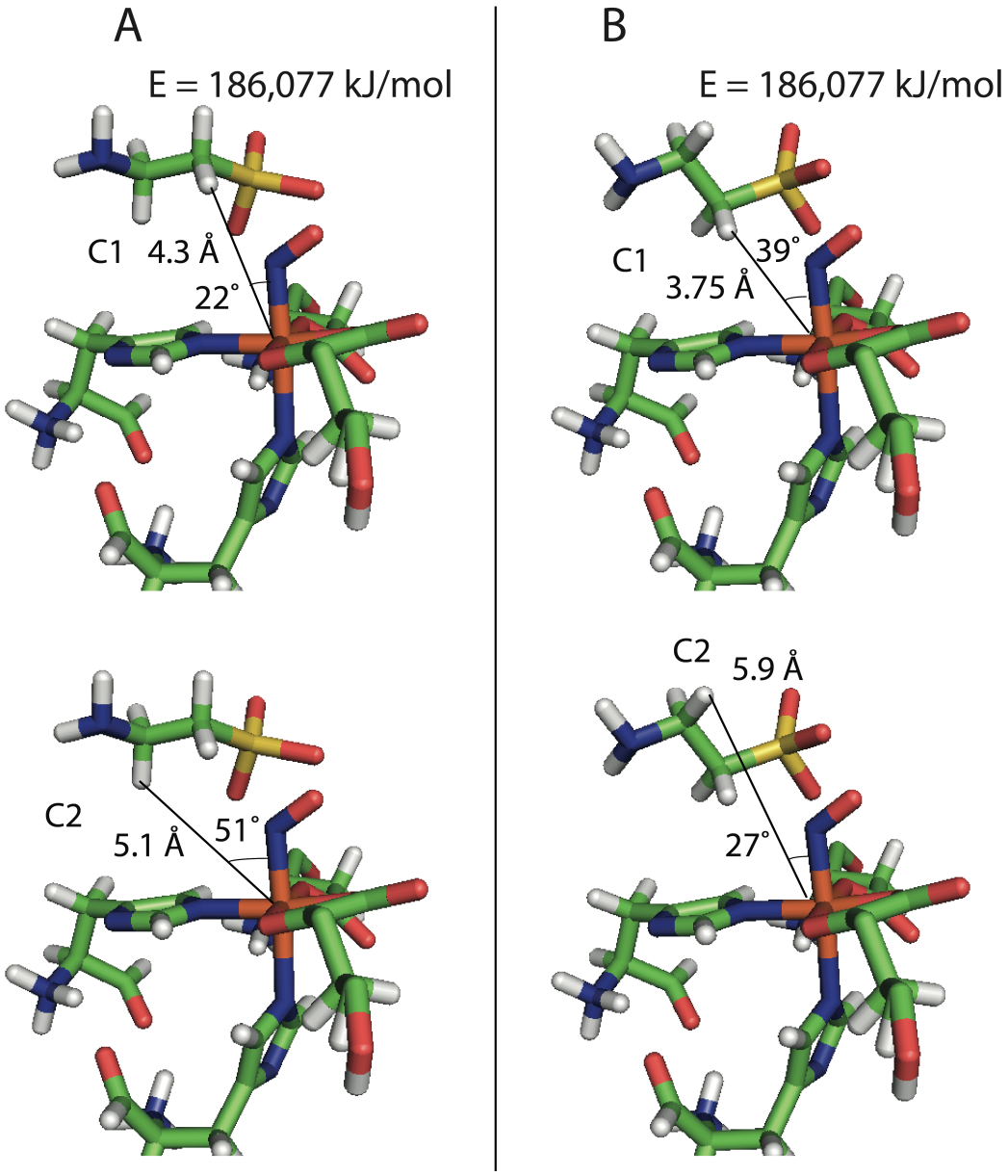

Figure 3.22. (A) The orientation of the ^{1}H-C1 and ^{1}H-C2 bonds predicted by the Avogadro optimized 1GY9 crystal structure. (B) The optimization was repeated after first manually reversing the ^{1}H-C1 and ^{1}H-C2 bond orientations. The two optimizations chose a different orientation for the bonds with an equal calculated energy.

The reversal of the ^{1}H-C1 and ^{1}H-C2 bonds pictured that is illustrated in Figure 3.22 is considered equally likely by the optimization. This means that instead of ESEEM being compared with the crystal structure's placement of taurine, the limited sets of Euler angle

combinations that will match the ESEEM results can instead be a guide for modeling the orientation of the taurine molecule in the crystal structure.

The distance of taurine from the $\{FeNO\}^7$ complex measured in this study supports the generally agreed upon mechanism that involves a hydrogen abstraction followed by radical rebound chemistry to be the most favorable mechanism for hydroxylating taurine **(7, 29)** of the two mechanisms mentioned above. The distance from the $\{FeNO\}^7$ complex provided by this ESEEM analysis would suggest the direct attack of the Fe(IV)=O on the C1 carbon of taurine that was suggested more recently based on rRaman data **(17)** is not as likely to compete with the favorable energetics of the generally agreed upon mechanism. However, their study provides compelling evidence for multiple intermediate species in the steps following the Fe(IV)=O in the mechanism and, with the implications of the ESEEM findings on the most likely reaction pathway only speculative, the present study cannot lead to a definitive conclusion on this topic.

Proton HYSCORE. The observation of cross peaks that are simulated as two sets of two protons that are oriented roughly 50˚ with regard to each other is consistent with what would be expected for the protons on the His ligands in the 1GY9 and 1OS7 crystal structures **(3, 4)**. Figure 3.23 shows the 1GY9 crystal structure **(3)** compared with a picture of the active site determined by HYSCORE.

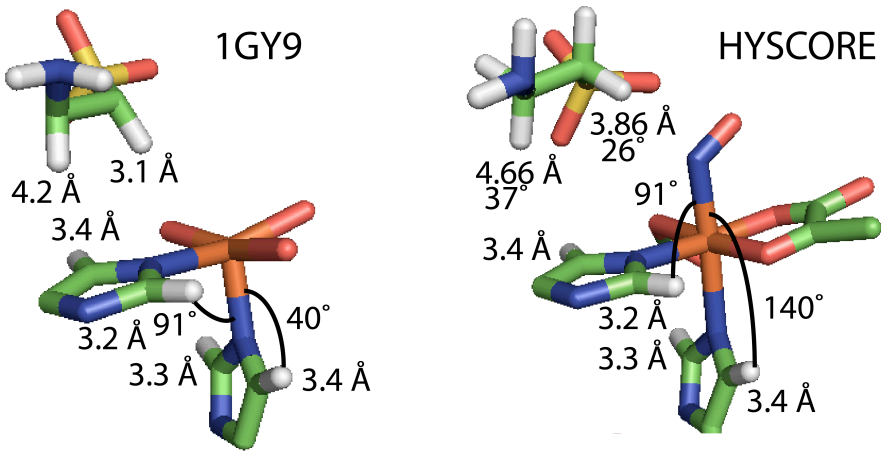

Figure 3.23. The crystal structure 1GY9 is absent of O_2 or NO so the angles relating the positions of the His protons to NO obtained with HYSCORE are not available for comparison. Instead, an assumption that the Fe-N(O) bond is exactly trans to the axial His bond is made to estimate the β_{HF} angle for beginning the simulation of the HYSCORE data.

Studying the trajectories of the cross peaks as a function of the orientation selective spectra allows for a more reliable assignment of couplings (Figure 3.12). The trajectory of the cross peaks as a function of the field position in orientation selective cases is unique to each combination of parameters. The broad arcs seen at low field (170 mT) that progress to tight spots at high field (330 mT) are characteristic of couplings to protons oriented roughly 90˚ to the principal axis of the ZFS (Figure 3.9 and 3.12B). The axially positioned protons will also show characteristic behavior that is opposite, tight spots at low field progressing to ovals in the high field spectra (Figure 3.10). The summed spectra shown in Figure 3.12 reflect these unique patterns observed in the data. For example, cross peaks assigned to taurine's protons are expected in a region that overlaps with the cross peaks owed to the protons on the axial His ligand. While

some intensity in those areas can be attributed to the taurine protons, the cross peaks are dominated by the stronger couplings with the His protons. Figures 3.13 and 3.14 illustrate the subtle contribution from the taurine protons to the HYSCORE spectra yet Figure 3.12A shows how tracking the behavior of all cross peaks in the spectra as a function of field strength can clearly isolate a pattern that can only be explained by couplings to the taurine protons.

The HYSCORE spectra for the samples that are missing taurine and α-KG suggest that the coordination environment is weakly dependent on the presence of taurine while it is strongly dependent on α-KG. In Figure 3.13 only subtle differences are noticeable when taurine is missing. However, in Figure 3.14 a complete loss of one set of cross peaks is observed when α-KG is missing. The loss is most easily observed at low field where orientation selective HYSCORE spectra are sampling orientations closest to the equatorial plane. The lost cross peaks correspond to the couplings with the protons on the equatorially bound His. Since complete reorientation of the coordination arrangement such that the binding of NO is trans to the Asp and cis to both His ligands is not likely as it would result in a different CW EPR spectrum **(8, 25, 30)**, it is possible that the missing α-KG allows the NO to bind in two positions: trans to His255 or trans to His 99. Both would result in the same relative orientation of NO to the "facial triad" ligand arrangement and possibly the same CW EPR spectrum but the equatorial His protons would assume different orientations relative to the principal axis of the ZFS. The observed disappearance of cross peaks that are signatures of perpendicularly oriented proton couplings would be expected. It is also possible that when α-KG is not present a protein conformational change re-orients the equatorial His ligand enough to change the β_{HF} angle in the same manner. Protein conformational changes were also suggested in metal and ligand binding studies of TauD

(13) and have been previously suggested for the absence of substrate and cofactor in a related class of amino acid hydroxylases that are dependent on terathydrobiopterin **(32-34)**. It is not likely that the coordination to the equatorial His is completely lost simply by removing α-KG. The "facial triad" coordination motif has been shown in many other studies of TauD to arrange even before the addition of taurine or α-KG and be a constant throughout the TauD mechanism **(35-37)**. The axial, single species, CW EPR spectrum for the TauD sample missing both α-KG and taurine suggests the same.

3.6 CONCLUSIONS

The assertion that TauD is the ideal non-heme Fe(II)/α-KG dependent dioxygenase for EPR study is supported by the observation that the CW EPR spectra show a minimal alteration of the magnetic properties of the $\{FeNO\}^7$ complex even in the absence of substrate and cofactor. This means that any observations made with ESEEM and HYSCORE can be made with confidence that mixtures of properties of different spin centers are not convoluting the analysis or introducing error.

The ^2H ESEEM results lend support to the previous study by Muthukumaran et al. **(19)** while providing a more complete analysis. The statistical fitting procedure was able to consistently select parameter sets in the same range. The grouping of similar parameter sets with similar χ^2 values suggest a global minimum. With the interpretation of the Euler angles presented in the discussion section the measurements agree reasonably with the energy optimized 1GY9 crystal structure **(3)** generated using Avogadro software **(26)**.

The method of analyzing orientation selective HYSCORE spectra as a sum provides a novel approach to assigning cross peaks. Congested spectra can still be analyzed in terms of individual couplings. This HYSCORE data represents the first direct confirmation of the binding of NO in the position trans to the axial His ligand when the α-KG and taurine are present in the complex. Previous studies have shown that NO is bound in this position **(8, 29, 38)** but this is the first direct correlation of the His ligands to each other. With the Fe-N(O) bond defining the principal axis of reference for measuring the dipolar coupling to the His protons with EPR, the observations of HYSCORE cross peaks owed to two sets of His protons oriented cis to each other can only be explained by having the NO bound in the "in line" position. By confirming this arrangement using HYSCORE the ESEEM measurements or the deviations in axial nature of the ZFS measured with CW EPR can be related to a structural reference frame defined by the His ligands. directly coordinated to the Fe center.

The absence of taurine has a subtle but measurable effect on the coordinated His ligands. The absence of α-KG, however, results in the loss of cross peaks owed to the protons on the His ligand that is supposed to be coordinated in plane with the α-KG when it is present. Since the CW EPR and previous structural data do not support a dramatic change in coordination arrangement, this suggests that either 1) the NO is allowed to bind trans to His99 instead of His255 or 2) a protein conformational change results in a measurable variability in the coordination to the equatorial His ligand when α-KG is not coordinated.

The CW EPR, ESEEM, and HYSCORE data together are in general agreement with what is already known for non-heme Fe(II)/α-KG dependent enzymes **(1)** and previous studies on TauD specifically **(8, 13, 14, 17, 39-41)**. The HYSCORE data contains directly measured

orientation and distance information that is usually inferred using crystallography data. The agreement of the two structures provides a metric for using HYSCORE to study the coordination of His ligands. Not only has this study added to the body of knowledge for TauD but has strongly suggested the efficacy of these EPR techniques for structural studies of paramagnetic enzyme complexes. The following chapter will detail the efforts to apply this methodology to study Xanthine hydroxylase (XanA) **(42-44)**, a poorly understood enzyme that is similar in sequence and biochemical properties to TauD but for which there does not exist a crystal structure or any detailed structural studies.

BIBLIOGRAPHY

BIBLIOGRAPHY

1. Hausinger, R. P. 2004. Fe(II)/alpha-ketoglutarate-dependent hydroxylases and related enzymes. Crit Rev Biochem Mol 39:21-68.

2. Eichhorn, E., J. R. vanderPloeg, M. A. Kertesz, and T. Leisinger. 1997. Characterization of alpha-ketoglutarate-dependent taurine dioxygenase from Escherichia coli. J Biol Chem 272:23031-23036.

3. Elkins, J. M., M. J. Ryle, I. J. Clifton, J. C. D. Hotopp, J. S. Lloyd, N. I. Burzlaff, J. E. Baldwin, R. P. Hausinger, and P. L. Roach. 2002. X-ray crystal structure of Escherichia coli taurine/alpha-ketoglutarate dioxygenase complexed to ferrous iron and substrates. Biochemistry-Us 41:5185-5192.

4. O'Brien, J. R., D. J. Schuller, V. S. Yang, B. D. Dillard, and W. N. Lanzilotta. 2003. Substrate-induced conformational changes in Escherichia coli taurine/alpha-ketoglutarate dioxygenase and insight into the oligomeric structure. Biochemistry-Us 42:5547-5554.

5. Ryle, M. J., and R. P. Hausinger. 1999. Kinetic investigation of alpha-ketoglutarate and taurine binding to E-coli taurine hydroxylase. J Inorg Biochem 74:284-284.

6. Zhang, Z. H., J. S. Ren, K. Harlos, C. H. McKinnon, I. J. Clifton, and C. J. Schofield. 2002. Crystal structure of a clavaminate synthase-Fe(II)-2-oxoglutarate-substrate-NO complex: evidence for metal centred rearrangements. Febs Lett 517:7-12.

7. Ye, S. F., and F. Neese. 2009. Quantum chemical studies of C-H activation reactions by high-valent nonheme iron centers. Curr Opin Chem Biol 13:89-98.

8. Ye, S. F., J. C. Price, E. W. Barr, M. T. Green, J. M. Bollinger, C. Krebs, and F. Neese. 2010. Cryoreduction of the NO-Adduct of Taurine:alpha-Ketoglutarate Dioxygenase (TauD) Yields an Elusive {FeNO}(8) Species. J Am Chem Soc 132:4739-4751.

9. Bassan, A., T. Borowski, and P. E. M. Siegbahn. 2004. Quantum chemical studies of dioxygen activation by mononuclear non-heme iron enzymes with the 2-His-1-carboxylate facial triad. Dalton T:3153-3162.

10. Price, J. C., E. W. Barr, B. Tirupati, J. M. Bollinger, and C. Krebs. 2003. The first direct characterization of a high-valent iron intermediate in the reaction of an alpha-ketoglutarate-dependent dioxygenase: A high-spin Fe(IV) complex in taurine/alpha-ketoglutarate dioxygenase (TauD) from Escherichia coli. Biochemistry-Us 42:7497-7508.

11. Bollinger, J. M., J. C. Price, E. W. Barr, B. Tirupati, and C. Krebs. 2003. Characterization of a high-spin Fe(IV) intermediate in the reaction of taurine/alpha-ketoglutarate dioxygenase (TauD). J Inorg Biochem 96:63-63.

12. Bollinger, J. M., J. C. Price, L. M. Hoffart, E. W. Barr, and C. Krebs. 2005. Mechanism of taurine: alpha-ketoglutarate dioxygenase (TauD) from Escherichia coli. Eur J Inorg Chem: 4245-4254.

13. Grzyska, P. K., R. P. Hausinger, and D. A. Proshlyakov. 2010. Metal and substrate binding to an Fe(II) dioxygenase resolved by UV spectroscopy with global regression analysis. Anal Biochem 399:64-71.

14. Grzyska, P. K., M. J. Ryle, G. R. Monterosso, J. Liu, D. P. Ballou, and R. P. Hausinger. 2005. Steady-state and transient kinetic analyses of taurine/alpha-ketoglutarate dioxygenase: Effects of oxygen concentration, alternative sulfonates, and active-site variants on the fe(IV)-oxo intermediate. Biochemistry-Us 44:3845-3855.

15. McCusker, K. P., and J. P. Klinman. 2009. Modular behavior of tauD provides insight into the origin of specificity in alpha-ketoglutarate-dependent nonheme iron oxygenases. P Natl Acad Sci USA 106:19791-19795.

16. Ryle, M. J., R. Padmakumar, and R. P. Hausinger. 1999. Stopped-flow kinetic analysis of Escherichia coli taurine/alpha-ketoglutarate dioxygenase: Interactions with alpha-ketoglutarate, taurine, and oxygen. Biochemistry-Us 38:15278-15286.

17. Grzyska, P. K., E. H. Appelman, R. P. Hausinger, and D. A. Proshlyakov. 2010. Insight into the mechanism of an iron dioxygenase by resolution of steps following the Fe-IV=O species. P Natl Acad Sci USA 107:3982-3987.

18. Ye, S. F., and F. Neese. 2011. Nonheme oxo-iron(IV) intermediates form an oxyl radical upon approaching the C-H bond activation transition state. P Natl Acad Sci USA 108:1228-1233.

19. Muthukumaran, R. B., P. K. Grzyska, R. P. Hausinger, and J. McCracken. 2007. Probing the iron-substrate orientation for taurine/alpha-ketoglutarate dioxygenase using deuterium electron spin echo envelope modulation spectroscopy. Biochemistry-Us 46:5951-5959.

20. Mims, W. B. 1972. Amplitudes of Superhyperfine Frequencies Displayed in Electron-Spin Echo Envelope. Phys Rev B 6:3543-&.

21. Stoll, S., and A. Schweiger. 2006. EasySpin, a comprehensive software package for spectral simulation and analysis in EPR. J Magn Reson 178:42-55.

22. Nelder, J. A., and R. Mead. 1965. A Simplex-Method for Function Minimization. Comput J 7:308-313.

23. Whitley, D. 1994. A Genetic Algorithm Tutorial. Stat Comput 4:65-85.

24. Kirkpatrick, S., C. D. Gelatt, and M. P. Vecchi. 1983. Optimization by Simulated Annealing. Science 220:671-680.

25. Aquino, F., and J. H. Rodriguez. 2009. Accurate Calculation of Zero-Field Splittings of (Bio)inorganic Complexes: Application to an {FeNO}(7) (S=3/2) Compound. J Phys Chem A 113:9150-9156.

26. Hanwell, M. D., D. E. Curtis, D. C. Lonie, T. Vandermeersch, E. Zurek, and G. R. Hutchison. 2012. Avogadro: an advanced semantic chemical editor, visualization, and analysis platform. J Cheminformatics 4.

27. Mazumder, D., and D. A. Case. 2007. AMBER Score in DOCK6: Application of molecular dynamics simulations and implicit solvent model (GB/SA) in protein-ligand docking. Abstr Pap Am Chem S 233:20-20.

28. Koehntop, K. D., J. P. Emerson, and L. Que. 2005. The 2-His-1-carboxylate facial triad: a versatile platform for dioxygen activation by mononuclear non-heme iron(II) enzymes. J Biol Inorg Chem 10:87-93.

29. Brown, C. A., M. A. Pavlosky, T. E. Westre, Y. Zhang, B. Hedman, K. O. Hodgson, and E. I. Solomon. 1995. Spectroscopic and Theoretical Description of the Electronic-Structure of S=3/2 Iron-Nitrosyl Complexes and Their Relation to O-2 Activation by Nonheme Tron Enzyme Active-Sites. J Am Chem Soc 117:715-732.

30. Solomon, E. I., T. C. Brunold, M. I. Davis, J. N. Kemsley, S. K. Lee, N. Lehnert, F. Neese, A. J. Skulan, Y. S. Yang, and J. Zhou. 2000. Geometric and electronic structure/function correlations in non-heme iron enzymes. Chem. Rev. 100:235-349.

31. Yang, T. C., M. D. Wolfe, M. B. Neibergall, Y. Mekmouche, J. D. Lipscomb, and B. M. Hoffman. 2003. Substrate binding to NO-ferro-naphthalene 1,2-dioxygenase studied by high-resolution Q-band pulsed H-2-ENDOR spectroscopy. J Am Chem Soc 125:7056-7066.

32. Li, J., L. J. Dangott, and P. F. Fitzpatrick. 2010. Regulation of Phenylalanine Hydroxylase: Conformational Changes Upon Phenylalanine Binding Detected by Hydrogen/Deuterium Exchange and Mass Spectrometry. Biochemistry-Us 49:3327-3335.

33. Stokka, A. J., R. N. Carvalho, J. F. Barroso, and T. Flatmark. 2004. Probing the role of crystallographically defined/predicted hinge-bending regions in the substrate-induced global conformational transition and catalytic activation of human phenylalanine hydroxylase by single-site mutagenesis. J Biol Chem 279:26571-26580.

34. Pey, A. L., M. Thorolfsson, K. Teigen, M. Ugarte, and A. Martinez. 2004. Thermodynamic characterization of the binding of tetrahydropterins to phenylalanine hydroxylase. J Am Chem Soc 126:13670-13678.

35. Hegg, E. L., A. K. Whiting, R. Padmakumar, R. E. Saari, R. P. Hausinger, and L. Que. 1998. Iron coordination environment of alpha-keto acid-dependent enzymes. Abstr Pap Am Chem S 216:U160-U160.

36. Hegg, E. L., R. Y. N. Ho, R. E. Saari, R. P. Hausinger, and L. Que. 1999. Coordination chemistry and reactivity of non-heme iron alpha-keto acid-dependent dioxygenases. J Inorg Biochem 74:158-158.

37. Hegg, E. L., A. K. Whiting, R. E. Saari, J. McCracken, R. P. Hausinger, and L. Que. 1999. Herbicide-degrading alpha-keto acid-dependent enzyme TfdA: Metal coordination environment and mechanistic insights. Biochemistry-Us 38:16714-16726.

38. Enemark, J. H., and R. D. Feltham. 1974. Principles of Structure, Bonding, and Reactivity for Metal Nitrosyl Complexes. Coordin Chem Rev 13:339-406.

39. Grzyska, P. K., and R. P. Hausinger. 2007. Cr-II reactivity of taurine/alpha-ketoglutarate dioxygenase. Inorg Chem 46:10087-10092.

40. Grzyska, P. K., R. P. Hausinger, and D. A. Proshlyakov. 2009. Resolution of substrate oxygenation steps in a nonheme Fe(II) enzyme. Abstr Pap Am Chem S 238:802-802.

41. Grzyska, P. K., T. A. Muller, M. G. Campbell, and R. P. Hausinger. 2007. Metal ligand substitution and evidence for quinone formation in taurine/alpha-ketoglutarate dioxygenase. J Inorg Biochem 101:797-808.

42. Montero-Moran, G. M., M. Li, E. Rendon-Huerta, F. Jourdan, D. J. Lowe, A. W. Stumpff-Kane, M. Feig, C. Scazzocchio, and R. P. Hausinger. 2007. Purification and characterization of the Fe-II- and alpha-ketoglutarate-dependent xanthine hydroxylase from Aspergillus nidulans. Biochemistry-Us 46:5293-5304.

43. Li, M., T. A. Miiller, B. A. Fraser, and R. P. Hausinger. 2008. Characterization of active site variants of xanthine hydroxylase from Aspergillus nidulans. Arch Biochem Biophys 470:44-53.

44. Darlington, A. J. 1968. Evidence for an alternative pathway of xanthine oxidation in Aspergillus niculans. BIOCHEMICA ET BIOPHYSICA ACTA:569-571.

CHAPTER 4

STRUCTURAL INVESTIGATION OF THE CATALYTIC CENTER OF XANTHINE HYDROXYLASE WITH CW EPR, ESEEM, AND HYSCORE

INTRODUCTION

Xanthine Hydroxylase (XanA) is a poorly understood member of the non-heme Fe(II)/α-KG dependent dioxygenase class of enzymes **(1-3)**. Despite its discovery being more than 40 years ago **(1)** XanA has only recently been characterized biochemically and in terms of sequence homology with other enzymes of this family **(2, 3)**. To date, however, XanA has not been analyzed in depth from a direct structural standpoint. There is not an available crystal structure and in depth spectroscopic studies to identify key reaction intermediates or direct structural involvement of ligands or the substrate have not yet been reported. This chapter details the application of the EPR techniques and data analysis procedures refined in the study of TauD to propose a structural homology model.

4.1 XANTHINE HYDROXYLASE

Studies carried out in 1968 by Darlington et. al. **(1)** demonstrated the ability of Aspergillus nidulans to grow on xanthine as a sole source of nitrogen even after loss of activity of other nitrogen metabolism enzymes such as xanthine dehydrogenase, the enzyme usually responsible for this activity. Researchers have since located the gene (termed *xanA*) responsible for this additional xanthine degradation pathway and found it to be transcriptionally coregulated with all other genes for purine degradation pathways **(3)**. In 2007 the Hausinger group reported the first in-depth biochemical characterization of XanA **(3)** as well as a separate mutagenesis study **(2)** that confirmed most aspects of the homology model suggested in the first study. The

protein exhibits similar biochemical properties as well as 33% sequence identity to TauD in the substrate binding site leading to the assignment of XanA as a fellow member of the non-heme Fe(II)/α-KG dependent dioxygenase class **(1-3)**. Figure 4.1 shows the general reaction carried out by XanA.

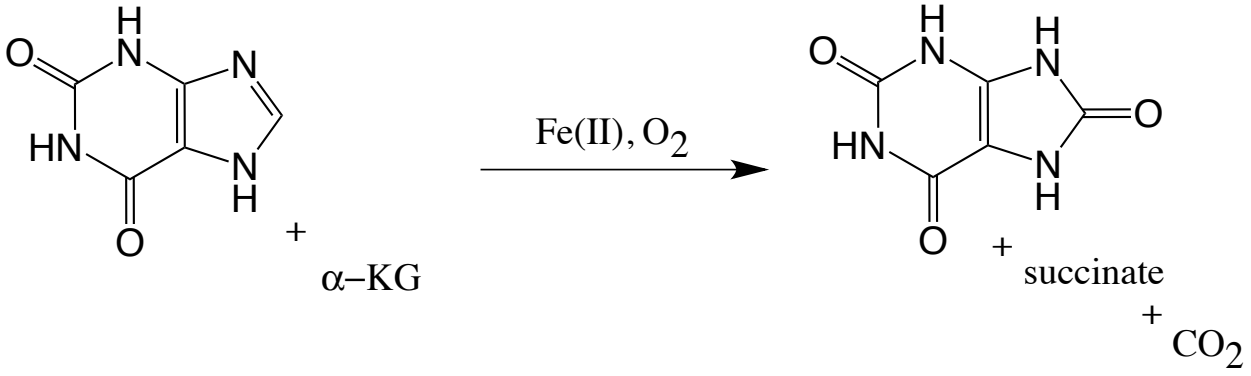

Figure 4.1. XanA converts xanthine and α-KG to uric acid, succinate, and CO_2 using O_2. Although the exact mechanism has not been studied, it is believed to be similar to other enzymes in the family.

As discussed in chapter 1, this class of enzymes is known for carrying out the same general reaction mechanism but with a diverse variety of substrate characters **(4)**. However, this is the first enzyme of this class to hydroxylate a free purine base. Although the inhibitory characteristics are typical for metal and ligand substitutions **(5)**, a clear isotope effect for [8-^{2}H]xanthine is not observed. Instead, a solvent deuterium isotope effect is observed **(3)**. This is atypical for enzymes of the non-heme Fe(II)/α-KG dependent dioxygenase family **(6-8)**. Other studies have also shown the existence of homologues of XanA in certain fungi **(9)** as well as its existence in parallel to other enzymes that perform the same reaction **(3)**. All of these findings

lead to open questions about the true homology and mechanistic similarities of this enzyme to other enzymes of the Fe(II)/α-KG dependent dioxygenase family.

4.2 PURPOSE

The study of TauD has established a systematic method for investigating structural aspects of non-heme Fe(II) dependent enzymes with CW EPR and pulsed EPR techniques. The general agreement of the findings with previous structural studies lends credibility to the use of EPR to study other enzymes for which there does not exist previous structural data. Application of the EPR techniques refined in the study of TauD could provide the first structural characterization of XanA and insight into the mechanistic similarities to other members of the enzyme family. The purpose of the work in this chapter is to: 1) investigate the similarities and differences between XanA and TauD using the EPR techniques refined in the study of TauD to confirm the identity of XanA as a non-heme Fe(II)/α-KG dependent hydroxylase and 2) apply CW EPR, ESEEM, and HYSCORE analysis techniques to propose a structural homology model.

4.3 EXPERIMENTAL

Sample preparation. The chemicals used in preparation were purchased from Sigma Aldrich. XanA protein was expressed, purified, and treated with 1 mM EDTA by the Hausinger group. Piotr Grzyska and William Kittleman performed the anaerobic preparation of the frozen XanA samples. The first sample was prepared by first suspending XanA apoprotein in degassed 50 mM Tris buffer at pH=8.0 that was then treated with degassed solutions of Fe(II), xanthine, and α-KG such that the final concentrations were: 0.3 mM XanA protein, 0.3 mM Fe(II), 1.2 mM xanthine

and 1.2 mM α-KG. The solution was then treated with NO by filling the headspace of the sealed sample vial with NO gas and lightly swirling the solution. Upon the observation of the solution changing to a yellow color the solution was quickly transferred anaerobically to an EPR tube with a syringe and frozen in liquid nitrogen. Additional samples were prepared in an identical fashion but were either treated with C8-^{2}H-xanthine in place of xanthine, prepared without xanthine, without α-KG, or without α-KG and xanthine. The sample prepared with C8-^{2}H-xanthine in place of xanthine differed in concentrations of Fe(II), C8-^{2}H-xanthine, and α-KG. The final concentrations were: 0.3 mM XanA protein, 0.5 mM Fe(II), 1.5 mM C8-^{2}H-xanthine, and 2.0 mM α-KG.

CW EPR experiments. CW EPR spectra were collected on a Bruker ESP300E X Band EPR spectrometer operating at 9.47 GHz. The sample temperature was maintained at 4 K using an Oxford Instruments ESR-900 liquid helium flow system. Helium flow was adjusted manually to maintain constant temperature. All EPR spectra were collected over a 300 mT range centered at 250 mT, with a modulation amplitude of 1 mT, a modulation frequency of 100 KHz, and at a power and video gain appropriate to each sample (judged by saturation of the EPR signal and signal to noise ratio of the spectrum at the optimum power). Spectra were averaged as necessary. Spectra were fit using the "esfit" function in the EasySpin software package to determine the ZFS and line width parameters.

ESEEM experiments. ESEEM spectra were collected using a Bruker E680 X band spectrometer using a model ER4118-MD-X-5-W1 probe with a 5 mm dielectric resonator. An Oxford instruments ITC-503 temperature controller and CR-935 liquid helium flow system was used to maintain a constant 4 K during ESEEM measurements. Data was collected using a three pulse

stimulated echo sequence that consisted of three 16ns π/2 (90°) microwave pulses as follows (π/2 - τ - π/2 - T1 - π/2). The time spacing τ was fixed and the spin echo was integrated as a function of T1. Data sets consisted of 512 points and were collected with a four step phase cycling procedure: (+,+,+), (-,+,+), (+,-,+), and (-,-,+) to remove unwanted echoes and baseline offsets. Plots of echo amplitude vs. time spacing (T1) were baseline corrected, treated with a Hamming window, zero filled to 1024 points, and cosine Fourier transformed to observe the frequency spectrum. Data sets were collected every 20 mT starting with 170 mT and ending at 330 mT.

Deuterium ESEEM. Identical ESEEM experiments were carried out on samples made with xanthine and C8-^{2}H-xanthine. Ratios of the normalized time domain spectra were taken to filter out unwanted ^{1}H and ^{14}N modulations and isolate the ESEEM from the C8 ^{2}H. The ratio spectra were baseline corrected, treated with a Hamming window, zero filled to 1024 points, and cosine Fourier transformed to observe the frequencies owed to the ^{2}H coupling.

HYSCORE experiments. HYSCORE spectra were collected using the same instrumentation and conditions as the ESEEM experiments. A four pulse sequence was used consisting of three 16 ns π/2 microwave pulses and one 32 ns π microwave pulse between the second and third π/2 pulses. The pulses were separated by three time spacings as follows (π/2 - τ - π/2 - T1 - π - T2 - π/2). A spin echo was integrated over a time width centered at τ after the fourth pulse as a function of both T1 and T2. The time spacing τ was chosen to suppress modulations from matrix protons. Data sets were 128 x 128 point square matrices consisting of 128 different T1 points for each of the 128 T2 points. The data sets were recorded with a four step phase cycling procedure to remove unwanted echoes and baseline offsets. For visualization of the two dimensional frequency spectrum each row and column of the square matrix was baseline corrected, treated

with a hamming window, and zero filled to 512 points. The entire matrix was subjected to two dimensional Fourier transformation. HYSCORE spectra for the XanA samples having α-KG and xanthine or C8-^{2}H-xanthine were collected at various field positions between 170 mT and 330 mT. The field positions 190 mT, 240 mT, and 320 mT were analyzed in depth. The data were interpreted by simulation using the EasySpin software package ***(10)*** operating in MATLAB. The simulations were performed using the ZFS parameters found by fitting the CW EPR spectra. Hamiltonian parameters were refined by manual adjustment from an initial set of parameters that were inferred from ESEEM and crystallographic data. The parameters that were varied when simulating the HYSCORE spectra were the isotropic HF coupling (a_{iso} in Equation 2.8), the dipolar coupling strength (T in Equation 2.8), and a β_{HF} Euler angle relating the principal axes of $\boldsymbol{A}$ tensor to the ZFS tensor. Isotropic HF coupling (a_{iso}) arises from a non zero probability of unpaired spin density at the coupled nucleus. The directly coordinated His ligands can share some of the unpaired spin by way of direct coordination to the paramagnetic $\{FeNO\}^{7}$ complex so a_{iso} was considered when interpreting the HYSCORE data.

4.4 RESULTS

CW EPR. The CW EPR spectra of the XanA samples are characteristic of the S=3/2 $\{FeNO\}^{7}$ complex having large ZFS ***(11)***. Figure 4.2 is the experimental and simulated CW EPR spectra for the various XanA samples.

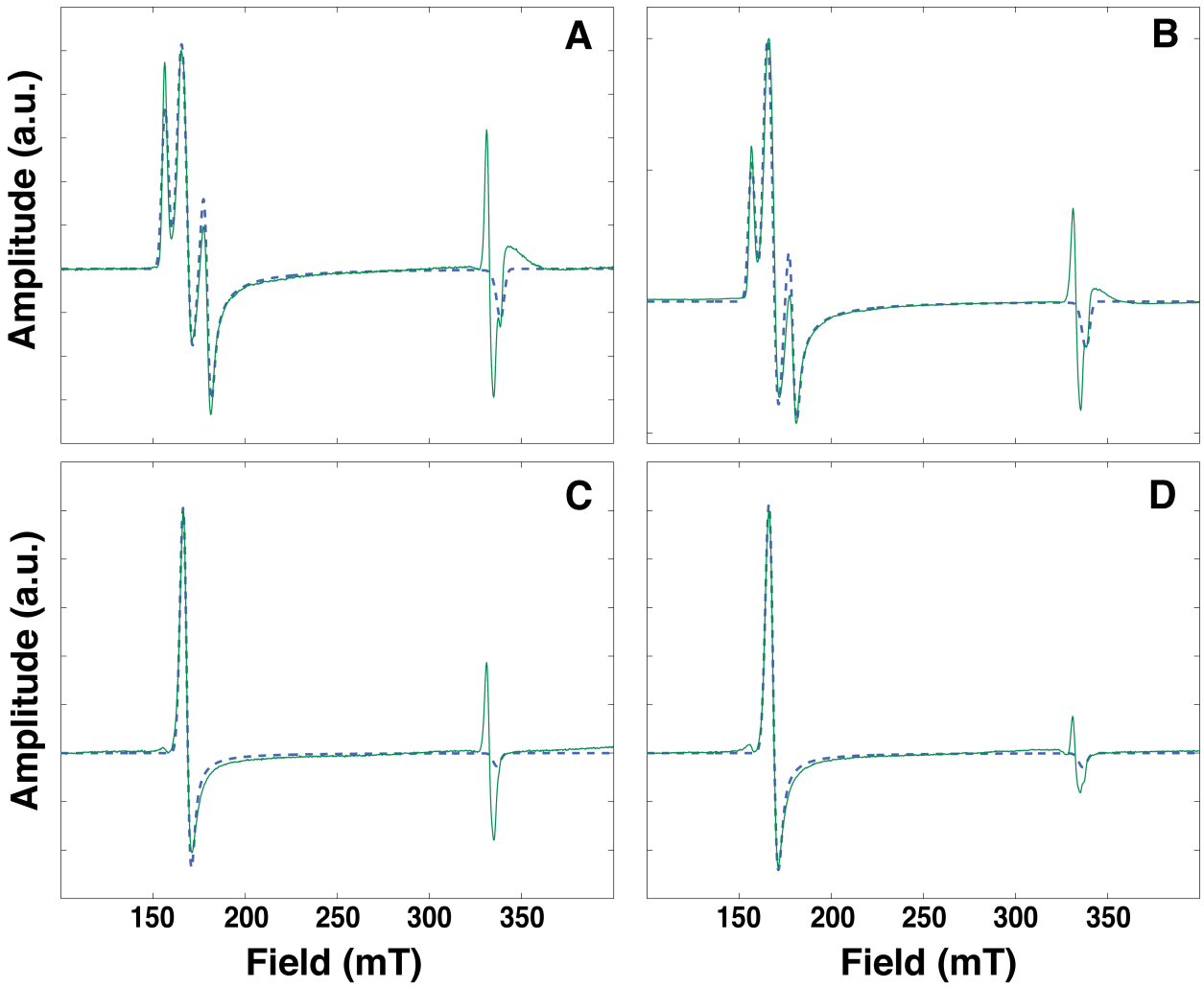

Figure 4.2. The experimental EPR spectra (in green) were fit (blue dashed line) with the "esfit" function of the EasySpin software package. In each case D = 10 cm^{-1}. The XanA sample that had α-KG and xanthine (A) was fit to a model where two species were present: a 75% contribution from a species with E/D=0.044 and 25% contribution from a species with E/D = 0.009. The sample that C8-^{2}H-xanthine was fit to a model where two species were present: a 63% contribution from a species with E/D=0.044 and 37% contribution from a species with E/D = 0.009. The samples that were missing α-KG or xanthine were fit to an axial model with E/D = 0. A line width parameter of 4.35 mT was used for all samples.

The EPR spectra for the samples that were missing either α-KG or xanthine were identical and characteristic of purely axial ZFS (E/D=0). The spectra were fit by varying only the line width parameter (lwpp). The EPR spectra for the samples having α-KG and xanthine or C8-^{2}H-

xanthine were characteristic of different degrees of mixtures of species having deviation from axial ZFS ($E/D \neq 0$) that can be read in the Figure 4.2 caption. When fitting these spectra by varying the ZFS parameters, the lwpp was assumed identical to the axial spectra. The differences in the relative amplitudes in the split peaks at g≈4 when C8-^{2}H-xanthine is substituted for xanthine are the result of different degrees of contribution from the two species contributing to the spectrum. The mixtures of species when xanthine or C8-^{2}H-xanthine are present suggests alterations in the binding of NO to the $\{FeNO\}^{7}$ complex induced by addition of the primary substrate. The study by Ye et al. ***(12)*** showed that different projections of the N=O bond over the equatorially bound ligands can result in different values of *E/D* suggesting that modification of the binding "mode" of NO, as it is described in chapter 3, would be the likely explanation for the significant splittings at $g_{\perp}$=4. The difference in the degree of contribution from each species between the two spectra can simply be a result of the two samples being prepared in a slightly different fashion. Because the *E/D* parameters are the same, this difference is not likely to describe different structural characteristics but simply reflect slight alterations in sample preparation steps involving freezing the samples. The XanA sample prepared without α-KG and xanthine showed the same axial spectrum and nearly the same lwpp as the TauD sample prepared without α-KG and taurine. Figure 4.3 is the CW EPR spectrum for the XanA sample prepared without α-KG and xanthine.

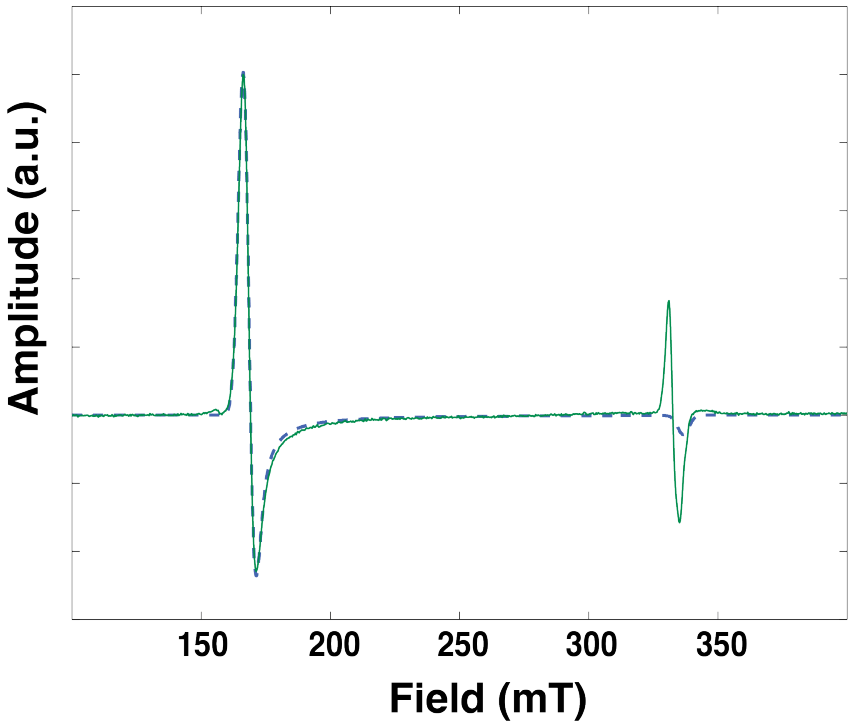

Figure 4.3. The experimental EPR spectrum for the sample missing α-KG and xanthine (in green) was fit (blue dashed line) with the "esfit" function of the EasySpin software package. Again the $D = 10$ cm^{-1}. The lwpp in this case was 4.4 mT.

The axial spectrum with a slightly enhanced lwpp indicates that, like TauD, there is a single energetically favored binding of NO that is allowed a slight variability in orientation by the conformational flexibility afforded by the absence of α-KG and xanthine.

Deuterium ESEEM. The ratio spectra meant to isolate the modulations owed to coupling with the ^{2}H at the C8 position on xanthine were inconclusive. Figure 4.4 is a stacked plot of the nine ratio spectra generated for XanA.

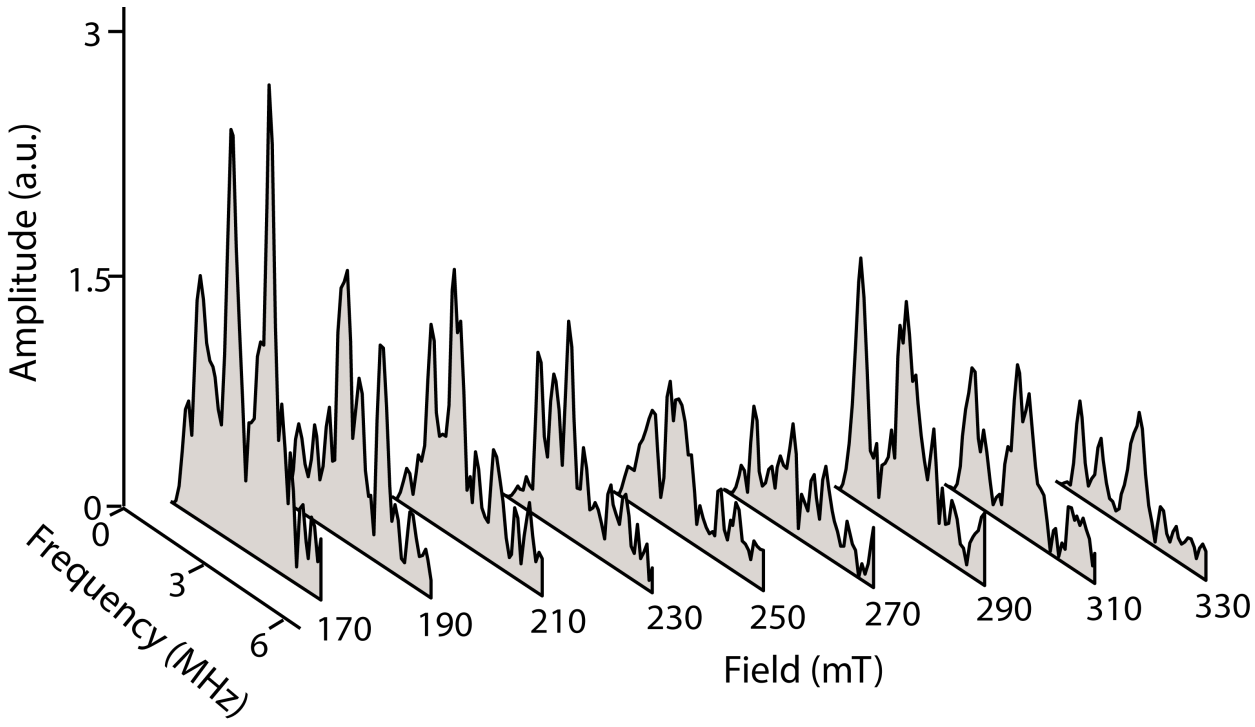

Figure 4.4. Ratios of ESEEM data were unable to isolate clear peaks centered at the ^{2}H Larmor frequency for studying the coupling with the C8 ^{2}H on xanthine.

Although fitting the ESEEM spectra using the procedure applied to the TauD ratio spectra could not yield reliable results, the lack of ESEEM from the C8 ^{2}H suggests either 1) that the ^{2}H is at a range beyond what is observable with ESEEM or 2) the ^{2}H is in a specific location relative to the principal axis of the ZFS that reduces the ESEEM effect. With considering the loss of signal to noise ratio introduced by taking the ratio of the two time domain ESEEM spectra, it can be estimated that any coupling beyond ~ 5 Å would not be resolvable. As discussed in chapter 2, the ESEEM effect is observed when the nuclear spin states are sufficiently mixed to allow for "branching" of EPR transitions. When the principal axis of the ***A*** tensor is aligned exactly with the canonical orientations of the ZFS, the modulation amplitudes are at a minimum. Also, the mixture of species in the EPR spectra for the two samples being studied could result in a broad

range of orientations of the ZFS tensor to the ***A*** tensors for each coupling including the interfering ^{1}H and ^{14}N couplings. This could have the effect of spreading out the frequency distribution for each coupling across the range of frequencies corresponding to the range of orientations of their ***A*** tensors with respect to the ZFS tensor. Not only would the individual frequency amplitudes be lower but the ratios would be less successful at isolating an individual interaction of interest. The coupling to each uniquely defined principal axis system would be slightly different and the frequencies for each ^{1}H and ^{14}N coupling would not line up exactly.

Proton HYSCORE. The cross peaks in the HYSCORE spectra collected for the XanA samples having both α-KG and xanthine were consistent with coupling to two sets of two protons. The couplings were similar in nature to what was observed with TauD for the protons on the directly coordinated His ligands. Figure 4.5 is HYSCORE spectra for the sample having α-KG and xanthine with simulations for the couplings with the two unique sets of protons.

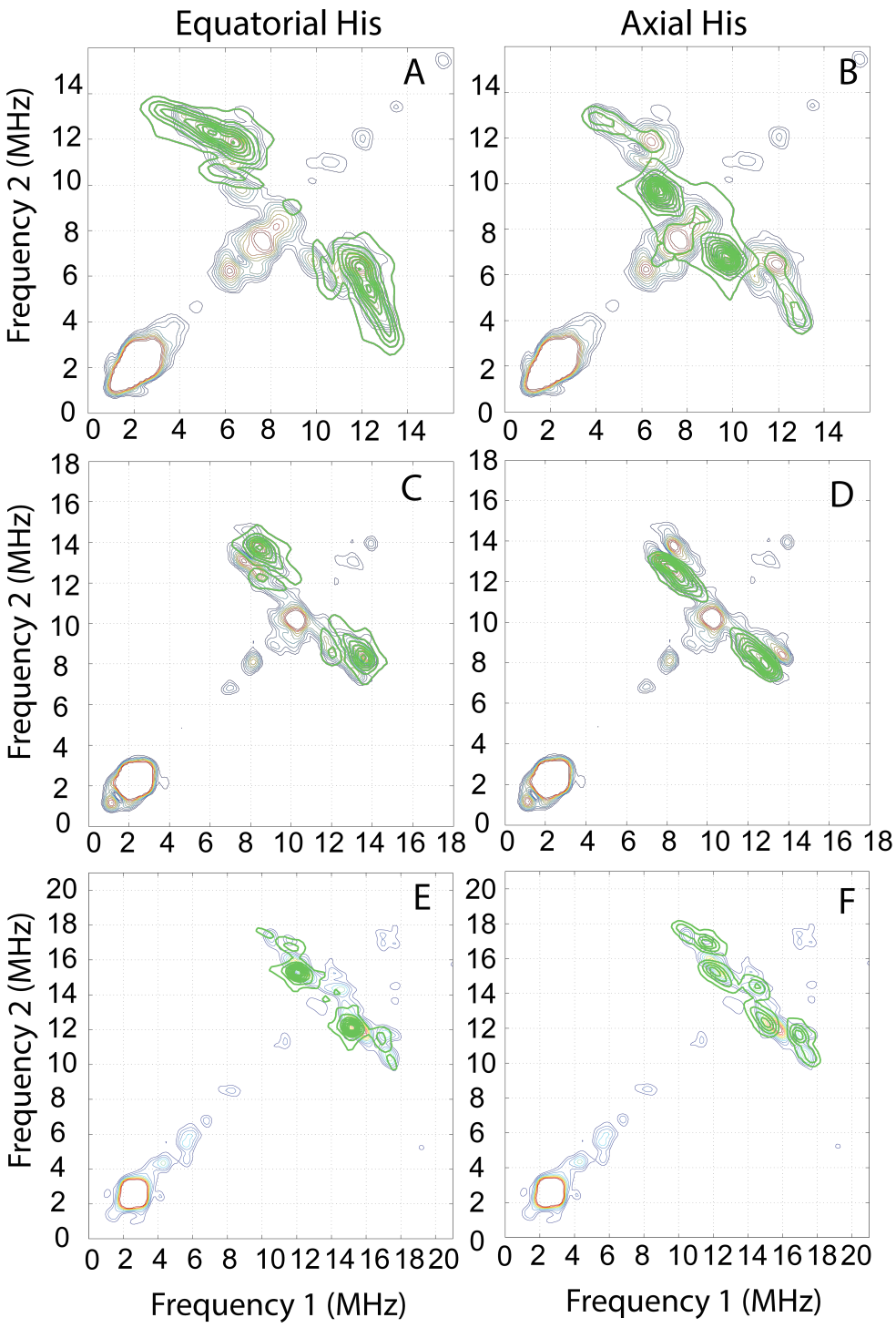

Figure 4.5. HYSCORE spectra collected at (A,B) 190 mT, (C,D) 240 mT, and (E,F) 320 mT for the XanA samples having α-KG and xanthine. The spectra A (190 mT), C (240 mT), and E (320 mT) were fit with a_{iso} = 0 MHz, T = 2.9 MHZ (r = 3 Å), and β_{HF} = 100˚. The spectra (B) 190 mT, (D) 240 mT, and (F) 320 mT were fit with a_{iso} = 0 MHz, *T* = 1.85 MHZ (r = 3.5 Å), and β_{HF} = 25-35˚.

Table 4.1 lists the Hamiltonian parameters used to simulate the XanA cross peaks.

	Equatorial His protons	Axial His protons
a_{iso} (MHz)	0	0
r (Å)	3.0	3.5
β_{HF} (˚)	100	25-35

Table 4.1. When simulating the cross peaks owed to couplings with protons on the His ligands and taurine, three parameters were considered variable: The isotropic HF coupling constant (a_{iso}), the dipolar distance (r) relating the ^{1}H dipole to the spin center, and the angle relating the principal axis of the HFI tensor to the direction of the Fe-N(O) bond (β_{HF}).

The lack of isotropic coupling represented in the spectra is consistent with weakly coordinated His ligands. Figure 4.6 is the comparison of the HYSCORE spectra in Figure 4.5 to identical spectra for the XanA samples with C8-^{2}H-xanthine in place of xanthine.

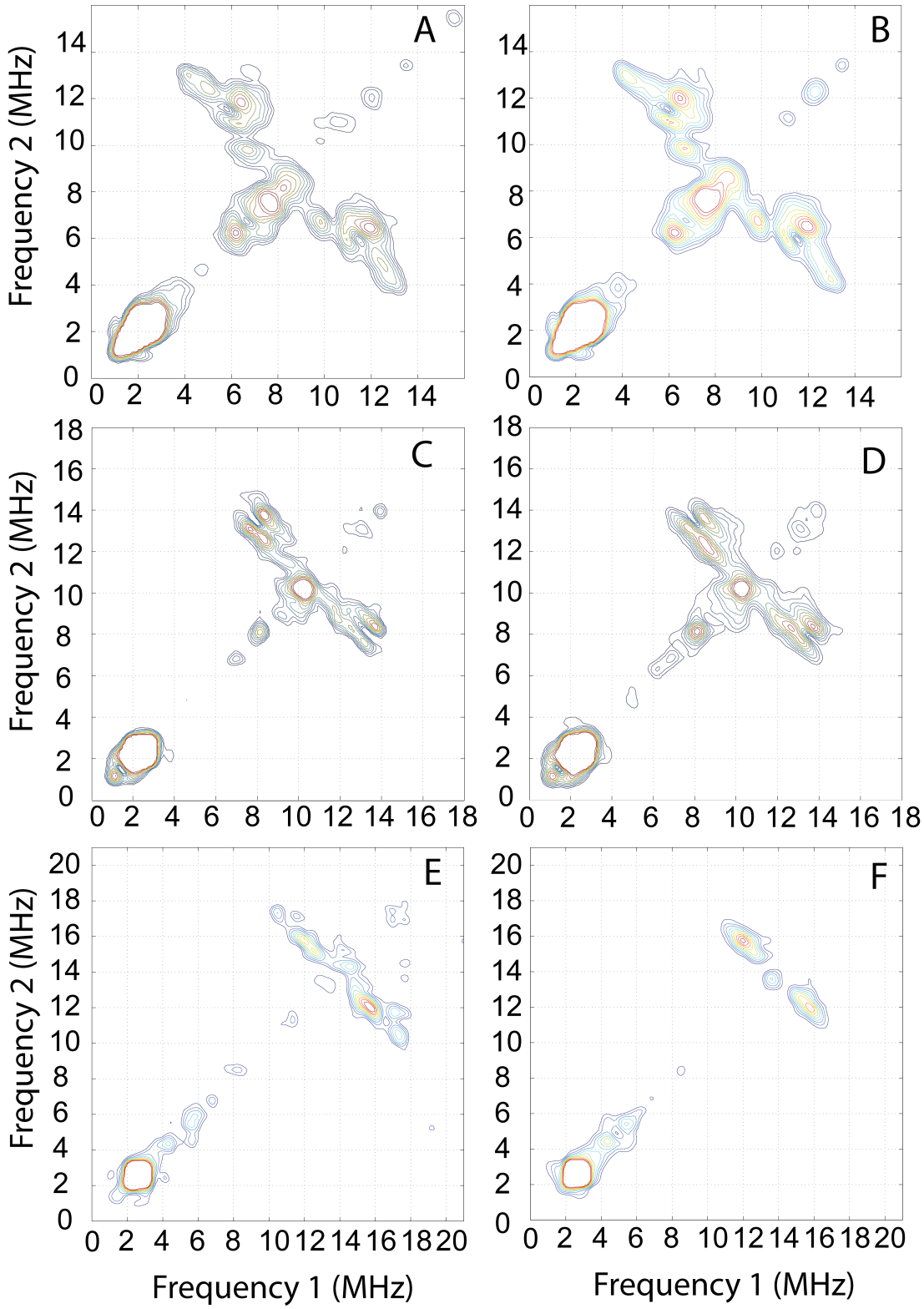

Figure 4.6. HYSCORE spectra A (190 mT), C (240 mT), and E (320 mT) for the sample with xanthine, (B) 190 mT, (D) 240 mT, and (F) 320 mT are for the sample with C8-^{2}H-xanthine.

The spectra for samples having C8-^{2}H-xanthine in place of xanthine are identical except for the weak features observed at 320 mT for the samples treated with xanthine at the frequency intersection of ~ 17.5 MHz and ~10.5 MHz that are not observed when C8-^{2}H-xanthine is substituted. If taken alone, these cross peaks are consistent with a strongly coupled proton that is aligned with the principal axis of the ZFS: *T, r* = 4 MHz, 2.7 Å and βHF = 0˚. The simulations in Figure 4.5E and F show that frequency amplitude in this region can be accounted for by the protons on the His ligands. The ESEEM data does not indicate a strong coupling with the ^{2}H on the C8-^{2}H-xanthine and the disappearance of cross peaks or loss of amplitude in the HYSCORE spectra at 190 mT and 240 mT is not observed.

4.5 DISCUSSION

Simulations of the XanA HYSCORE data identifies cross peaks that reflect two unique sets of protons coordinated in orientations similar to the protons on the His ligands for TauD. The dipolar distances to these protons are consistent with two weakly coordinated His ligands. While sequence identity and biochemical characterization suggests that XanA is a non-heme Fe(II) dependent hydroxylase **(1-3)**, the direct measurement of two coordinated His ligands oriented cis to each other strongly suggests the “facial triad” triad Fe(II) binding motif **(13)** and lends to the assignment of XanA to this class of enzymes. The differences in orientation of the His ligands and the dipolar distances to the His protons when compared to TauD are within what would be expected for two different enzymes and do not suggest a different coordination environment. Figure 4.7 shows comparison of XanA HYSCORE spectra with the corresponding TauD HYSCORE spectra.

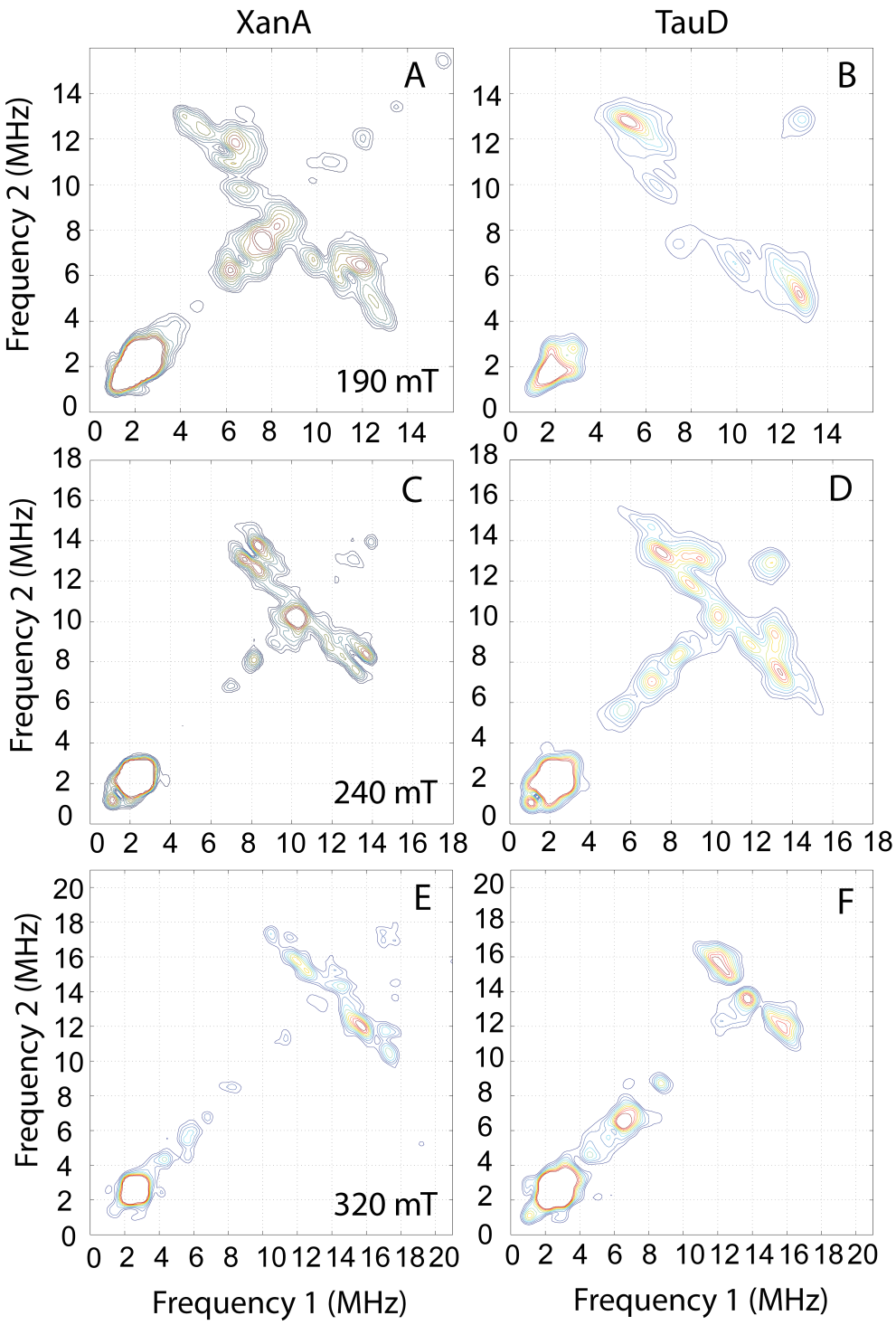

Figure 4.7. The HYSCORE spectra for XanA collected at A) 190 mT, B) 240 mT, and C) 320 mT show similarities with the corresponding spectra for TauD: D) 190 mT, E) 240 mT, and F) 320 mT. Although some differences are clear, the observation of cross peaks in the same regions with the same general character can only be possible with similar couplings.

Although the exact shapes of the cross peaks are different, the same general character of the cross peaks is only possible with similar couplings.

The CW EPR spectra also suggest a similarity in NO coordination in XanA to that observed in TauD. The clear preference for a single binding mode of NO in the CW EPR spectra of samples missing α-KG and/or xanthine is consistent with TauD. However, a clear difference in the coordination characteristics when both α-KG and xanthine are present is observed. The CW EPR data in chapter 3 for TauD suggests not only that a single binding "mode" for NO is preferred, but that it is most strictly preferred when the α-KG and taurine are present. With XanA the coincident presence of α-KG and xanthine triggers the introduction of a significant deviation in axial symmetry of the ZFS for a majority of the spin centers. If XanA were to exhibit the "off line" arrangement **(4)** discussed in chapter 1, the NO would be forced to bind in the coordination site trans to the equatorial His and pointed away from the substrate pocket. The report by Ye et al. **(12)** shows that a simple difference in projection of the N=O bond over the equatorial coordination plane of TauD's $\{FeNO\}^7$ complex can yield different *E/D* values. The ~ 25% increase in calculated *E/D* for the different projections they evaluated, however, is relatively modest. The > 4 fold increase in *E/D* between the two species in the CW EPR data for XanA suggests that the change in the NO binding is much more significant. Figure 4.8 provides a visual for the "off line" binding mode as it would look in the XanA active site.

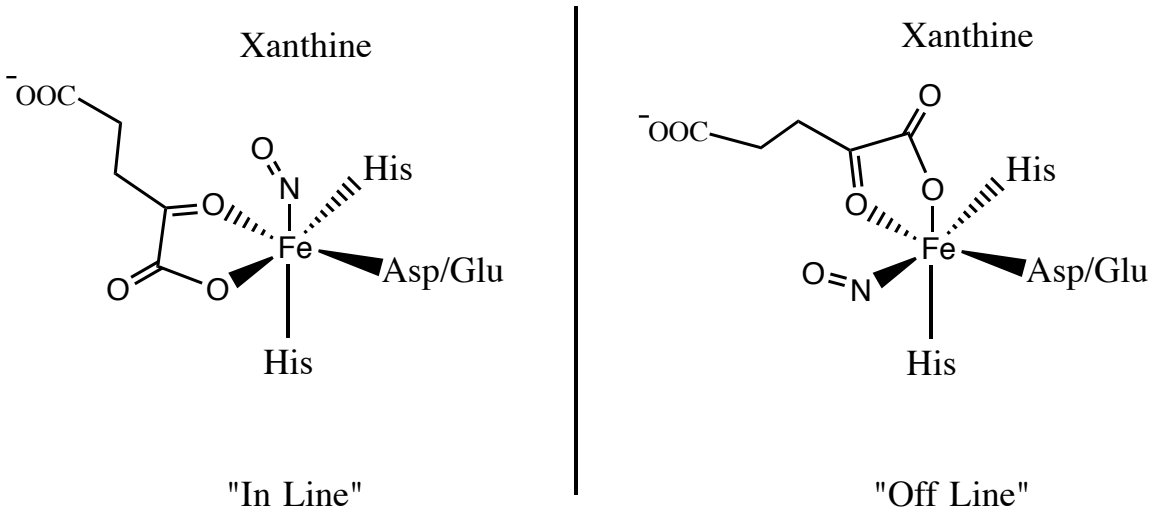

Figure 4.8. The "in line" arrangement of α-KG positions the open coordination site for NO towards the substrate binding pocket. This arrangement is observed exclusively in TauD and the resulting NO position has been shown to be preferred even when α-KG is not present. The "off line" arrangement is seen in some non-heme Fe(II)/α-KG dependent enzymes. The resulting binding orientation of NO is similar in relation to the directly coordinated ligands but is now trans to the substrate binding pocket.

While the TauD data suggests that the difference in NO binding "positions" in the absence of α-KG may not be discernible with CW EPR, the different NO position forced by the "off line" arrangement while α-KG is present in XanA may be the cause of the observed increase in *E/D*. With TauD, the HYSCORE data suggested that a variability in NO positions was allowed only when α-KG wasn't present while, with XanA, the variability would be forced by α-KG presence. The forced change in NO binding could be accompanied by an alteration in projection of the N=O bond or a forced bending of the Fe-N(O) bond resulting in deviation of the ZFS tensor from axial symmetry. Because the EPR samples are composed of unreacted catalytic centers, the mixture of the two species in the CW EPR spectra suggests that the two NO binding modes are available simultaneously prior to the catalytic reaction. The "off line" mechanism has been suggested to allow for flexibility between the two α-KG arrangements prior to the catalytic

mechanism as a possible explanation for the retention of reactivity **(4)**. The "off line" mode being the majority in the unreacted enzyme complex could also suggest that the "ferryl flip" **(14)** after the decarboxylation of α-KG is the likely mechanism for interaction of O_2 with xanthine.

The lack of ^2H ESEEM in the ratio spectra for the substitution of xanthine with C8-^2H-xanthine is consistent with dipolar couplings that are too weak to be observed. While this could be the result of xanthine simply being bound further from the $\{FeNO\}^7$ complex, it could also be explained by the prevalence of the species in the CW EPR spectra that has a larger *E/D*. If this second species is the "off line" arrangement, the C1 carboxylate group of the α-KG would be positioned directly between the xanthine molecule and the $\{FeNO\}^7$ complex (Figure 4.8). The axial species representing the "in line" arrangement where interaction of the ^2H on C8-^2H-xanthine with the $\{FeNO\}^7$ complex would not be blocked by the α-KG is only a minority species in the CW EPR spectra and would not be enough to make extraction of ^2H couplings from the spectral ratio procedure possible. In addition, the ratio of ESEEM spectra collected for samples that have different degrees of mixtures (See Figure 4.2) of active site arrangements would be unreliable. The redefinition of the principal axes of the ZFS by the forced binding of NO in the "off line" position would change the orientation of the dipolar couplings to the principal magnetic axes. There would be a mixture of the two orientations of the dipolar couplings to the principal magnetic axes that would be different for each sample. Some frequencies in the two spectra used in taking the ratio would not have a counterpart and they would survive the division and introduce noise to the ratio spectra. It is less likely that the xanthine is bound considerably further from the $\{FeNO\}^7$ complex since hydroxylase activity

has been shown to take place with typical kinetic behavior **(3)**. The loss of the high frequency peaks at the intersection of ~17 MHz and ~11 MHZ in the HYSCORE for the sample with the C8 ^{2}H substituted xanthine would suggest the coupling belongs to the C8 ^{1}H on xanthine. However, the parameters necessary to simulate these cross peaks would indicate a ^{1}H coupling with a dipolar distance of only ~2.7 Å and a βHF of ~0˚. The ESEEM results are not consistent with a strong coupling that would result from this positioning of the C8 ^{2}H.

4.6 CONCLUSIONS

The HYSCORE data supports the assignment of XanA to the non-heme Fe(II)/α-KG dependent hydroxylase class of enzymes (1-3). The well characterized TauD enzyme was used as a subject to confirm the crystallography data with HYSCORE and the application of the same analysis to XanA reveals a close similarity. Observation of cross peaks owed to protons on axially and equatorially bound His ligands is a signature of the "facial triad" Fe(II) binding motif (13). While the HYSCORE measurements yield confirmation of the His ligands and strongly suggest the "facial triad" motif (13), the CW EPR spectra and ESEEM data suggest a difference in coordination characteristics when α-KG and xanthine are present. The CW EPR spectra collected on samples having α-KG and xanthine are consistent with what may be observed if XanA exhibited the "off line" binding mode for α-KG (4). The result would be a forced binding of NO to a different coordination position possibly accompanied by a change in N=O bond projection in the complex (12). Mixtures of two distinctly different species in the EPR spectrum suggests that conformational rearrangement can take place as would be necessary in order for enzymes exhibiting the "off line" mechanism to retain activity (4). The dominant species being

the different binding mode in the unreacted complex suggests that the reorientation of NO (O_2 in the mechanism) to the "in line" position occurs after decarboxylation of α-KG. This is consistent with the proposed "ferryl flip" (14) to allow for the interaction of O_2 with xanthine. The likely cause for the lack of ^2H ESEEM in the ratio spectra is that the "off line" coordination of α-KG in XanA is positioning the C1 carboxylate of α-KG directly between the ^2H on xanthine and the $\{FeNO\}^7$ complex. The binding of xanthine a long distance from the $\{FeNO\}^7$ complex while retaining hydroxylase activity would likely be accompanied by slow reaction kinetics that are not observed in the biochemical characterizations (2, 3).

The CW EPR and HYSCORE data for XanA support the proposal that XanA is a non-heme Fe(II)/α-KG dependent hydroxylase. The observation of interesting differences in the CW EPR data lead to questions about the similarity in mechanism to other members of the same enzyme family. With the observation of variability in the coordination environment when α-KG and xanthine are present and the suggestion of the "off line" α-KG binding mode (4), structural characterization of XanA could represent direct analysis of the "off line" mechanism, an aspect of this enzyme family that has not received much attention. The following chapter will summarize the results of the study of TauD and XanA with EPR spectroscopy.

BIBLIOGRAPHY

BIBLIOGRAPHY

1. Darlington, A. J. 1968. Evidence for an alternative pathway of xanthine oxidation in Aspergillus niculans. Biochemica et Biophysica Acta:569-571.

2. Li, M., T. A. Miiller, B. A. Fraser, and R. P. Hausinger. 2008. Characterization of active site variants of xanthine hydroxylase from *Aspergillus nidulans*. Arch Biochem Biophys 470:44-53.

3. Montero-Moran, G. M., M. Li, E. Rendon-Huerta, F. Jourdan, D. J. Lowe, A. W. Stumpff-Kane, M. Feig, C. Scazzocchio, and R. P. Hausinger. 2007. Purification and characterization of the Fe-II- and alpha-ketoglutarate-dependent xanthine hydroxylase from Aspergillus nidulans. Biochemistry-Us 46:5293-5304.

4. Hausinger, R. P. 2004. Fe(II)/alpha-ketoglutarate-dependent hydroxylases and related enzymes. Crit Rev Biochem Mol 39:21-68.

5. Kalliri, E., P. K. Grzyska, and R. P. Hausinger. 2005. Kinetic and spectroscopic investigation of Co-II, Ni-II, and N-oxalylglycine inhibition of the Fe-II/alpha-ketoglutarate dioxygenase, TauD. Biochem Bioph Res Co 338:191-197.

6. Krebs, C., J. C. Price, E. W. Barr, B. Tirupati, T. E. Glass, M. T. Green, and J. M. Bollinger. 2004. Mechanistic studies on the oxygen activation by taurine : alphaketoglutarate dioxygenase (TauD) from E. coli. Abstr Pap Am Chem S 227:U1422-U1422.

7. Grzyska, P. K., E. H. Appelman, R. P. Hausinger, and D. A. Proshlyakov. 2010. Insight into the mechanism of an iron dioxygenase by resolution of steps following the Fe-IV=O species. P Natl Acad Sci USA 107:3982-3987.

8. Grzyska, P. K., R. P. Hausinger, and D. A. Proshlyakov. 2009. Resolution of substrate oxygenation steps in a nonheme Fe(II) enzyme. Abstr Pap Am Chem S 238:802-802.

9. Cultrone, A., C. Scazzocchio, M. Rochet, G. Montero-Moran, C. Drevet, and R. Fernandez-Martin. 2005. Convergent evolution of hydroxylation mechanisms in the fungal kingdom: molybdenum cofactor-independent hydroxylation of xanthine via alpha-ketoglutarate-dependent dioxygenases. Mol Microbiol 57:276-290.

10. Stoll, S., and A. Schweiger. 2006. EasySpin, a comprehensive software package for spectral simulation and analysis in EPR. J Magn Reson 178:42-55.

11. Brown, C. A., M. A. Pavlosky, T. E. Westre, Y. Zhang, B. Hedman, K. O. Hodgson, and E. I. Solomon. 1995. Spectroscopic and Theoretical Description of the Electronic-Structure of S=3/2 Iron-Nitrosyl Complexes and Their Relation to O-2 Activation by Nonheme Tron Enzyme Active-Sites. J Am Chem Soc 117:715-732.

12. Ye, S. F., J. C. Price, E. W. Barr, M. T. Green, J. M. Bollinger, C. Krebs, and F. Neese. 2010. Cryoreduction of the NO-Adduct of Taurine:alpha-Ketoglutarate Dioxygenase (TauD) Yields an Elusive {FeNO}(8) Species. J Am Chem Soc 132:4739-4751.

13. Koehntop, K. D., J. P. Emerson, and L. Que. 2005. The 2-His-1-carboxylate facial triad: a versatile platform for dioxygen activation by mononuclear non-heme iron(II) enzymes. J Biol Inorg Chem 10:87-93.

14. Zhang, Z. H., J. S. Ren, K. Harlos, C. H. McKinnon, I. J. Clifton, and C. J. Schofield. 2002. Crystal structure of a clavaminate synthase-Fe(II)-2-oxoglutarate-substrate-NO complex: evidence for metal centred rearrangements. Febs Lett 517:7-12.

CHAPTER 5

SUMMARY OF THE EPR INVESTIGATION OF TAURINE HYDROXYLASE AND XANTHINE HYDROXYLASE

INTRODUCTION

The structural investigation of metal centered enzymes with EPR spectroscopy provides a wealth of structural information **(1, 2)**. The complementary information available from CW EPR and pulsed EPR allows for the study of connections between structure and function using a single experimental technique. The confirmation of previously known characteristics of TauD **(3-10)** support the efficacy of CW EPR, ESEEM, and HYSCORE. The introduction of new analysis techniques has yielded some additional information for TauD and provides a means for more effective studies in the future. The comparison of data for XanA to the findings for TauD represents a direct structural correlation to accompany the observation of sequence identity **(11, 12)**. The ability to obtain interpretable structural information from an enzyme that had not yet been structurally characterized based on comparison to a similar enzyme gives a promising outlook for the use of EPR to gain structural information on other non-heme Fe(II) dependent enzymes for which there is little or no previous structural data. This chapter is a summary of the important findings for TauD and XanA.

5.1 SUMMARY OF TAUD AND XANA RESULTS

The wealth of information already available for TauD **(3-5, 7-10, 13-18)** made possible the refining of the data collection and analysis procedures using TauD as a subject. The HYSCORE results for TauD support the model of the coordinated ligands predicted in the crystal structures. The results for XanA suggest a similar structure. Figures 5.1 and 5.2 summarize the

HYSCORE results taken from chapters 3 and 4. With simulations, the cross peaks in the TauD spectra were successfully modeled by couplings with His protons that were in the same position relative to the Fe center that was predicted in the crystal structures. By applying the method of adding multiple orientation selective HYSCORE spectra, the nature of the couplings were clearly distinguished. The orientations of the couplings that explain the contours in the added spectra are consistent with two protons oriented perpendicular to the Fe-N(O) bond and two at 140˚ from the Fe-N(O) bond. This relative orientation of the two sets of protons is only possible with the NO trans to one of the His ligands. With the placement of the NO in a specific location relative to the other ligands, the ESEEM measurements and CW EPR have a better defined structural context. When evaluating the XanA HYSCORE, the observation of cross peaks consistent with coupling to two sets of two protons in similar orientations to the His protons in TauD suggest that XanA also possesses the "facial triad" binding motif that is characteristic for non-heme Fe(II) dependent enzymes. The assignment of XanA to this class of enzymes is confirmed. Figure 5.1 shows the comparison of the 1GY9 crystal structure to the results of the TauD HYSCORE.

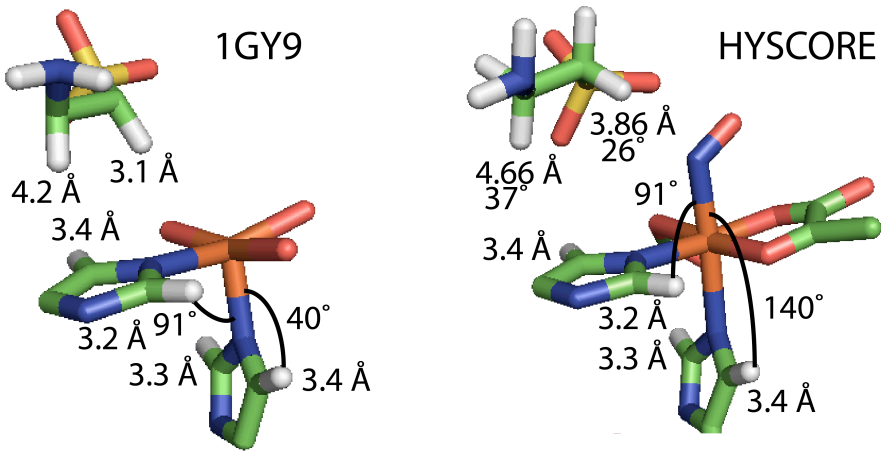

Figure 5.1. The resulting picture of the TauD active site derived from the analysis of the HYSCORE data for TauD presented in chapter 3.

Figure 5.2 shows the comparison of the XanA and TauD HYSCORE data.

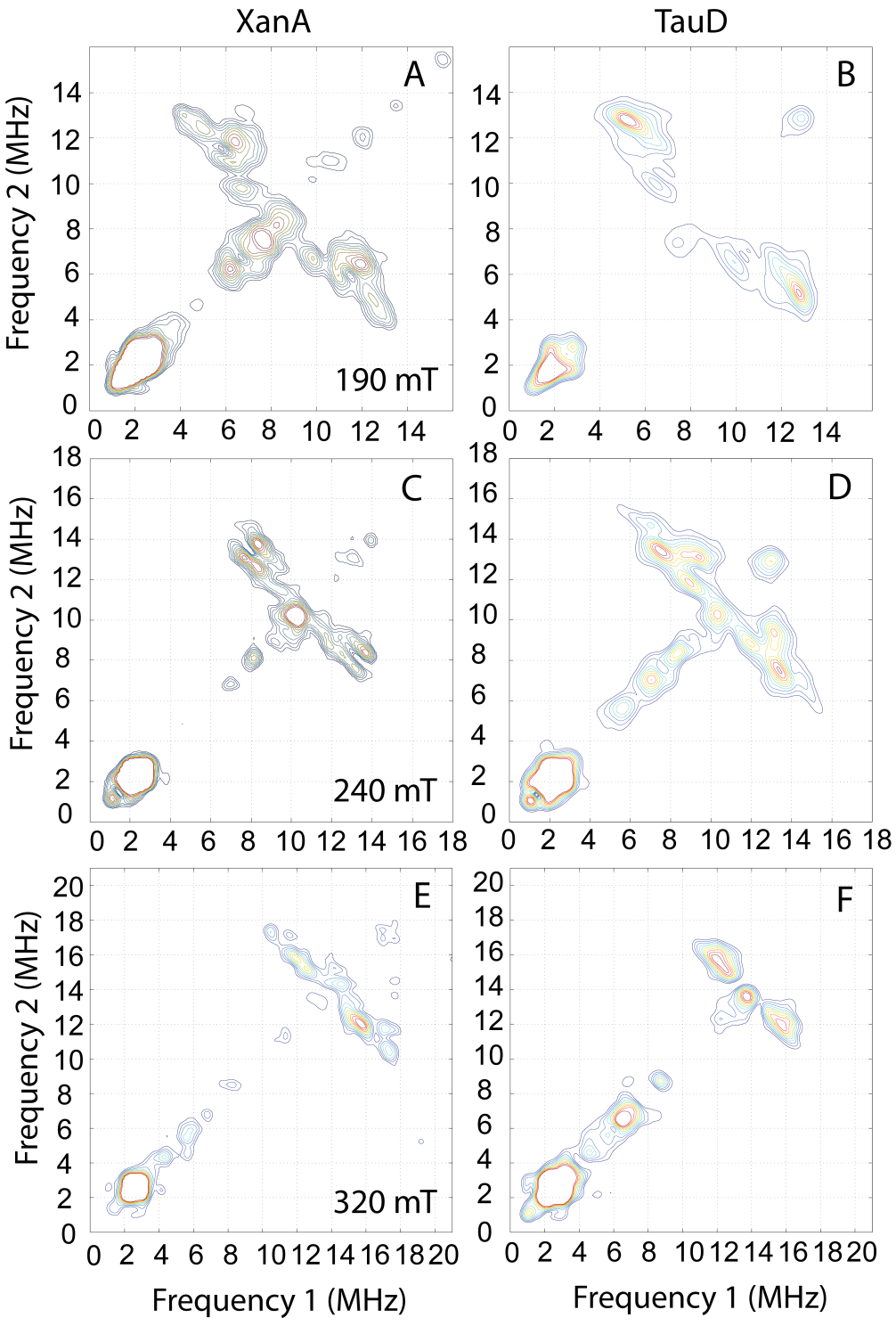

Figure 5.2. The comparison of the HYSCORE data for XanA at (A) 190 mT (C) 240 mT and (E) 320 mT to the data for TauD at (B) 190 mT (D) 240 mT and (F) 320 mT shows only a slight difference in proton couplings. The data for both enzymes was consistent with protons on the His ligands of the "facial triad" motif that is known for all non-heme Fe(II) dependent enzymes.

The CW EPR findings for TauD and XanA can be interpreted in the context of the structural characteristics of the "facial triad" Fe(II) binding motif **(19)**. Figures 5.3 summarizes the CW EPR results taken from Figures 3.4 and 4.2.

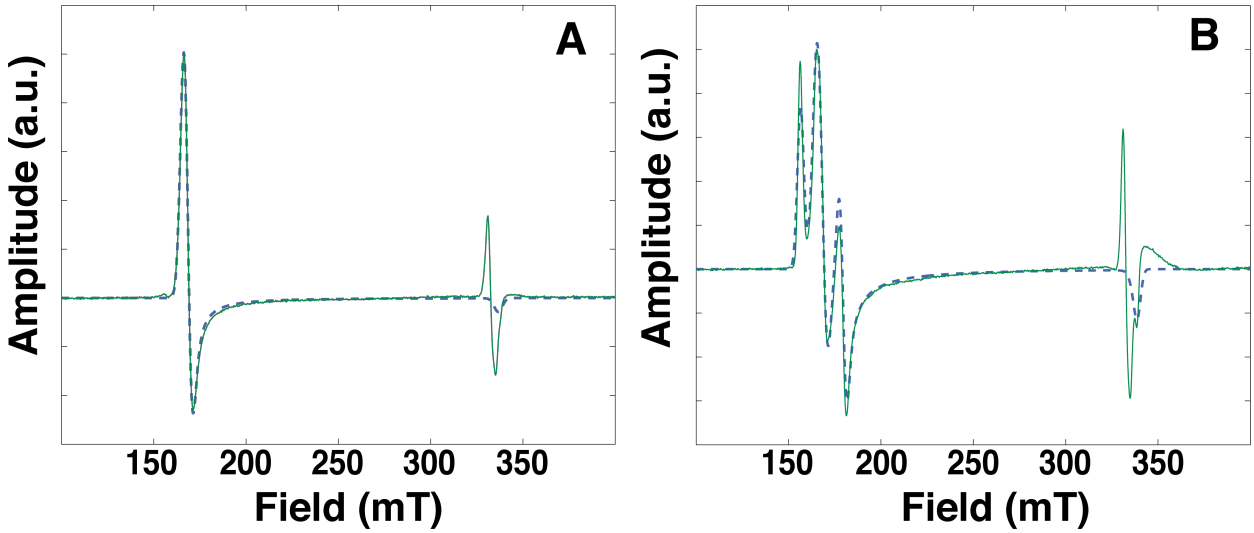

Figure 5.3. The CW EPR spectrum that shows a single axial species (A) is consistent with the preferred "in line" binding position for NO. This spectrum was observed with a slightly varying degree of line width for all TauD and XanA samples except for the XanA samples containing α-KG and xanthine. The spectrum for the XanA samples with α-KG and xanthine showed a mixture of two spectra with different ZFS parameters (B). The new species in the mixture was attributed to the "off line" binding mode. Complete analysis of the spectra are available in chapters 3 and 4.

The single preferred binding mode for NO in the $\{FeNO\}^7$ complex suggested in previous theoretical and structural studies **(8, 20, 21)** of TauD was confirmed. The "in line" arrangement of the TauD active site is also confirmed by the CW EPR and HYSCORE results that indicate a single binding mode for NO and a His ligand arrangement consistent with the crystal structures in the presence of taurine and α-KG **(9, 10)**. The observation of the preference for a single binding mode of NO in both XanA and TauD when α-KG and/or substrate are missing suggests

that the preferred binding of NO in the "facial triad" motif is constant regardless of the presence of α-KG or substrate. The observation of a second species with distinctly different ZFS parameters in the spectrum for the XanA samples having both α-KG and xanthine suggests that XanA may exhibit the "off line" α-KG binding arrangement. Based on theoretical studies **(8, 22, 23)**, a deviation from axial symmetry of the ZFS accompanies any difference in projection of the N=O bond over the complex. The distinct difference between the two species in the spectrum could be the result of redefinition of the N=O projection forced by the "off line" arrangement.

The position of taurine in the TauD active site measured with ESEEM is consistent with previous structural data for TauD **(9, 10, 18)**. The ESEEM results are summarized in Figure 5.4 is taken from Figures 3.19 and 3.22.

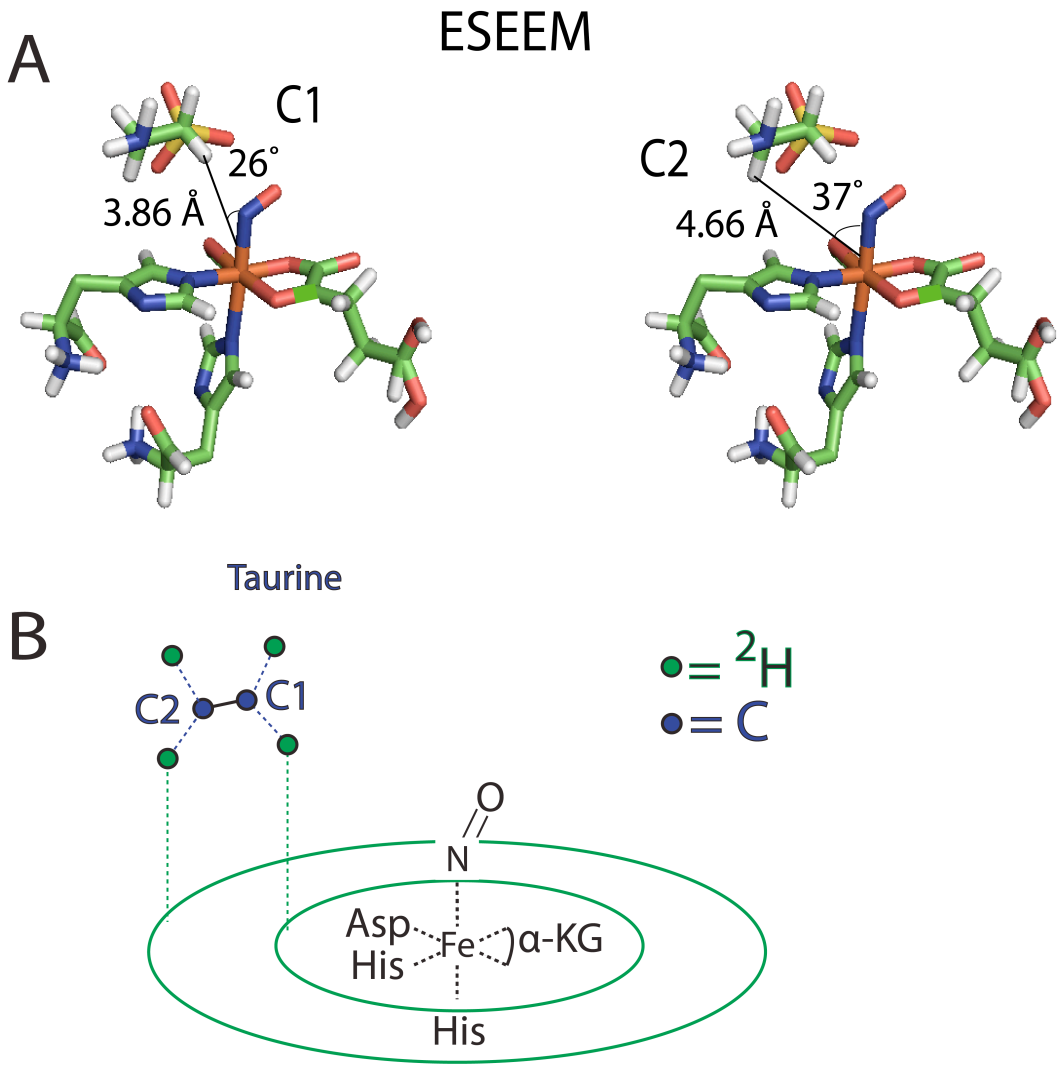

Figure 5.4. (A) Summary of the dipolar distances and β_{HF} angles measured with ESEEM for the deuterons on taurine. (B) A drawing to illustrate the likely orientation of the C1-C2 unit of taurine based on the NQI Euler angles measured with ESEEM. The green circles illustrate the uncertainty in the exact position of taurine's deuterons over the equatorial coordination plane when γ_{HF} cannot be determined.

The evaluation of the orientation of taurine by using Euler angles that describe the orientation of the ^{2}H-C bonds on taurine allows for EPR data to give a more precise placement of taurine. The structural context provided by the HYSCORE data allows for more reliable interpretations of the ESEEM measurements. The exact physical meaning of some of the measurements are subject to

multiple interpretations but confidence in the orientation of NO and the directly coordinated ligands afforded by the combined HYSCORE and CW EPR findings can restrict the complicated analysis to describing only positions of taurine that are consistent with the structural context. The results can aid in the correct positioning of taurine in the electron density map generated by crystallography experiments **(9, 10)**. At the resolution of the current crystallography data for TauD, the reliability of the placement of taurine is low and the ESEEM measurements provide a more refined picture. The use of energy optimization of the crystal structure's placement of taurine aids in providing a more reliable comparison to the ESEEM results because the optimized position of taurine is based on interactions of taurine with the surrounding protein.

5.2 CONCLUSIONS

The enzymes TauD and XanA are non-heme Fe(II)/α-KG dependent hydroxylases and show the characteristic "facial triad" coordination motif. The previous structural data for TauD **(9, 10, 18)** is generally confirmed. For XanA, a structural homology model to TauD now accompanies the sequence homology previously observed. The EPR techniques used in this thesis provide an effecient method for structural studies of non-heme Fe(II) dependent enzymes. The future use of these techniques can provide reasonably reliable structural information for enzymes without prior structural study.

BIBLIOGRAPHY

BIBLIOGRAPHY

1. Calle, C., A. Sreekanth, M. V. Fedin, J. Forrer, I. Garcia-Rubio, I. A. Gromov, D. Hinderberger, B. Kasumaj, P. Leger, B. Mancosu, G. Mitrikas, M. G. Santangelo, S. Stoll, A. Schweiger, R. Tschaggelar, and J. Harmer. 2006. Pulse EPR methods for studying chemical and biological samples containing transition metals. Helv Chim Acta 89:2495-2521.

2. Prisner, T., M. Rohrer, and F. MacMillan. 2001. Pulsed EPR spectroscopy: Biological applications. Annu Rev Phys Chem 52:279-313.

3. Bollinger, J. M., J. C. Price, E. W. Barr, B. Tirupati, and C. Krebs. 2003. Characterization of a high-spin Fe(IV) intermediate in the reaction of taurine/alpha-ketoglutarate dioxygenase (TauD). J Inorg Biochem 96:63-63.

4. Bollinger, J. M., J. C. Price, L. M. Hoffart, E. W. Barr, and C. Krebs. 2005. Mechanism of taurine: alpha-ketoglutarate dioxygenase (TauD) from Escherichia coli. Eur J Inorg Chem: 4245-4254.

5. Price, J. C., E. W. Barr, B. Tirupati, J. M. Bollinger, and C. Krebs. 2003. The first direct characterization of a high-valent iron intermediate in the reaction of an alpha-ketoglutarate-dependent dioxygenase: A high-spin Fe(IV) complex in taurine/alpha-ketoglutarate dioxygenase (TauD) from Escherichia coli. Biochemistry-Us 42:7497-7508.

6. Ryle, M. J., and R. P. Hausinger. 1999. Kinetic investigation of alpha-ketoglutarate and taurine binding to E-coli taurine hydroxylase. J Inorg Biochem 74:284-284.

7. Ryle, M. J., R. Padmakumar, and R. P. Hausinger. 1999. Stopped-flow kinetic analysis of Escherichia coli taurine/alpha-ketoglutarate dioxygenase: Interactions with alpha-ketoglutarate, taurine, and oxygen. Biochemistry-Us 38:15278-15286.

8. Ye, S. F., J. C. Price, E. W. Barr, M. T. Green, J. M. Bollinger, C. Krebs, and F. Neese. 2010. Cryoreduction of the NO-Adduct of Taurine:alpha-Ketoglutarate Dioxygenase (TauD) Yields an Elusive {FeNO}(8) Species. J Am Chem Soc 132:4739-4751.

9. O'Brien, J. R., D. J. Schuller, V. S. Yang, B. D. Dillard, and W. N. Lanzilotta. 2003. Substrate-induced conformational changes in Escherichia coli taurine/alpha-ketoglutarate dioxygenase and insight into the oligomeric structure. Biochemistry-Us 42:5547-5554.

10. Elkins, J. M., M. J. Ryle, I. J. Clifton, J. C. D. Hotopp, J. S. Lloyd, N. I. Burzlaff, J. E. Baldwin, R. P. Hausinger, and P. L. Roach. 2002. X-ray crystal structure of Escherichia coli taurine/alpha-ketoglutarate dioxygenase complexed to ferrous iron and substrates. Biochemistry-Us 41:5185-5192.

11. Li, M., T. A. Miiller, B. A. Fraser, and R. P. Hausinger. 2008. Characterization of active site variants of xanthine hydroxylase from Aspergillus nidulans. Arch Biochem Biophys 470:44-53.

12. Montero-Moran, G. M., M. Li, E. Rendon-Huerta, F. Jourdan, D. J. Lowe, A. W. Stumpff-Kane, M. Feig, C. Scazzocchio, and R. P. Hausinger. 2007. Purification and characterization of the Fe-II- and alpha-ketoglutarate-dependent xanthine hydroxylase from Aspergillus nidulans. Biochemistry-Us 46:5293-5304.

13. Grzyska, P. K., E. H. Appelman, R. P. Hausinger, and D. A. Proshlyakov. 2010. Insight into the mechanism of an iron dioxygenase by resolution of steps following the Fe-IV=O species. P Natl Acad Sci USA 107:3982-3987.

14. Grzyska, P. K., R. P. Hausinger, and D. A. Proshlyakov. 2010. Metal and substrate binding to an Fe(II) dioxygenase resolved by UV spectroscopy with global regression analysis. Anal Biochem 399:64-71.

15. Grzyska, P. K., T. A. Muller, M. G. Campbell, and R. P. Hausinger. 2007. Metal ligand substitution and evidence for quinone formation in taurine/alpha-ketoglutarate dioxygenase. J Inorg Biochem 101:797-808.

16. Grzyska, P. K., M. J. Ryle, G. R. Monterosso, J. Liu, D. P. Ballou, and R. P. Hausinger. 2005. Steady-state and transient kinetic analyses of taurine/alpha-ketoglutarate dioxygenase: Effects of oxygen concentration, alternative sulfonates, and active-site variants on the fe(IV)-oxo intermediate. Biochemistry-Us 44:3845-3855.

17. McCusker, K. P., and J. P. Klinman. 2009. Modular behavior of tauD provides insight into the origin of specificity in alpha-ketoglutarate-dependent nonheme iron oxygenases. P Natl Acad Sci USA 106:19791-19795.

18. Muthukumaran, R. B., P. K. Grzyska, R. P. Hausinger, and J. McCracken. 2007. Probing the iron-substrate orientation for taurine/alpha-ketoglutarate dioxygenase using deuterium electron spin echo envelope modulation spectroscopy. Biochemistry-Us 46:5951-5959.

19. Koehntop, K. D., J. P. Emerson, and L. Que. 2005. The 2-His-1-carboxylate facial triad: a versatile platform for dioxygen activation by mononuclear non-heme iron(II) enzymes. J Biol Inorg Chem 10:87-93.

20. Brown, C. A., M. A. Pavlosky, T. E. Westre, Y. Zhang, B. Hedman, K. O. Hodgson, and E. I. Solomon. 1995. Spectroscopic and Theoretical Description of the Electronic-Structure of S=3/2 Iron-Nitrosyl Complexes and Their Relation to O-2 Activation by Nonheme Tron Enzyme Active-Sites. J Am Chem Soc 117:715-732.

21. Enemark, J. H., and R. D. Feltham. 1974. Principles of Structure, Bonding, and Reactivity for Metal Nitrosyl Complexes. Coordin Chem Rev 13:339-406.

22. Solomon, E. I., T. C. Brunold, M. I. Davis, J. N. Kemsley, S. K. Lee, N. Lehnert, F. Neese, A. J. Skulan, Y. S. Yang, and J. Zhou. 2000. Geometric and electronic structure/function correlations in non-heme iron enzymes. Chem. Rev. 100:235-349.

23. Decker, A., J. U. Rohde, L. Que, and E. I. Solomon. 2004. Spectroscopic and quantum chemical characterization of the electronic structure and bonding in a non-heme Fe-IV=O complex. J Am Chem Soc 126:5378-5379.

APPENDICES

APPENDIX A

Derivation of $\hat{H}_{ZFS}$:

Starting with the term,

$$\hat{H}_{ZFS} = \hat{S} \bullet \underset{\sim}{D} \bullet \hat{S} \qquad \textbf{[A.1]}$$

The $\hat{S}$ operator can be written as vector,

$$\hat{S} = [\hat{S}_x, \hat{S}_y, \hat{S}_z] \qquad \textbf{[A.2]}$$

And the *D* matrix can be written as a traceless tensor,

$$\underset{\sim}{D} = \begin{pmatrix} -\frac{1}{3}D + E & 0 & 0 \\ 0 & -\frac{1}{3}D - E & 0 \\ 0 & 0 & \frac{2}{3}D \end{pmatrix} \qquad \textbf{[A.3]}$$

Taking the dot product,

$$\hat{H}_{ZFS} = [\hat{S}_x, \hat{S}_y, \hat{S}_z] \bullet \begin{pmatrix} -\frac{1}{3}D + E & 0 & 0 \\ 0 & -\frac{1}{3}D - E & 0 \\ 0 & 0 & \frac{2}{3}D \end{pmatrix} \bullet \begin{bmatrix} \hat{S}_x \\ \hat{S}_y \\ \hat{S}_z \end{bmatrix} \qquad \textbf{[A.4]}$$

yields,

$$\hat{\mathrm{H}}_{ZFS} = \hat{S}_x^2\left(-\frac{1}{3}D + E\right) + \hat{S}_y^2\left(-\frac{1}{3}D - E\right) + \hat{S}_z^2\frac{2}{3}D \qquad \textbf{[A.5]}$$

Simplification gives,

$$\hat{\mathrm{H}}_{ZFS} = \hat{S}_x^2 E - \hat{S}_y^2 E - \frac{D}{3}\hat{S}^2 + \frac{3}{3}D\hat{S}_z^2 \qquad \textbf{[A.6]}$$

Further simplification gives Equation 2.1.

$$\hat{\mathrm{H}}_{ZFS} = D\left(\hat{S}_z^2 - \frac{\hat{S}^2}{3}\right) + E\left(\hat{S}_x^2 - \hat{S}_y^2\right) \qquad \textbf{[A.7]}$$

Solving for Eigenvalues of the Hamiltonian expression that describes the EPR spectrum:

Starting with the complete form of the Hamiltonian Equation 2.3,

$$\hat{\mathrm{H}} = g\beta \underset{\sim}{B}_0 \bullet \underset{\sim}{\hat{S}} + D(\hat{S}_z^2 + S(S+1)/3) + E(\hat{S}_x^2 - \hat{S}_y^2) \qquad \textbf{[A.8]}$$

We can operate on the S=3/2 density matrix,

$$\underset{\sim}{\mathrm{M}}_D = \begin{pmatrix} \langle 3/2|\hat{\mathrm{H}}|3/2\rangle & \langle 3/2|\hat{\mathrm{H}}|1/2\rangle & \langle 3/2|\hat{\mathrm{H}}|-1/2\rangle & \langle 3/2|\hat{\mathrm{H}}|-3/2\rangle \\ \langle 1/2|\hat{\mathrm{H}}|3/2\rangle & \langle 1/2|\hat{\mathrm{H}}|1/2\rangle & \langle 1/2|\hat{\mathrm{H}}|-1/2\rangle & \langle 1/2|\hat{\mathrm{H}}|-3/2\rangle \\ \langle -1/2|\hat{\mathrm{H}}|3/2\rangle & \langle -1/2|\hat{\mathrm{H}}|1/2\rangle & \langle -1/2|\hat{\mathrm{H}}|-1/2\rangle & \langle -1/2|\hat{\mathrm{H}}|-3/2\rangle \\ \langle -3/2|\hat{\mathrm{H}}|3/2\rangle & \langle -3/2|\hat{\mathrm{H}}|1/2\rangle & \langle -3/2|\hat{\mathrm{H}}|-1/2\rangle & \langle -3/2|\hat{\mathrm{H}}|-3/2\rangle \end{pmatrix} \qquad \textbf{[A.9]}$$

using each of the $\hat{S}_x$, $\hat{S}_y$, and $\hat{S}_z$ operators separately.

$$\hat{S}_x = \frac{S_+ + S_-}{2} = \frac{1}{2}\begin{pmatrix} 0 & \sqrt{3} & 0 & 0 \\ \sqrt{3} & 0 & 2 & 0 \\ 0 & 2 & 0 & \sqrt{3} \\ 0 & 0 & \sqrt{3} & 0 \end{pmatrix} \qquad \textbf{[A.10]}$$

$$\hat{S}_y = \frac{S_+ - S_-}{2i} = \frac{1}{2i}\begin{pmatrix} 0 & \sqrt{3} & 0 & 0 \\ -\sqrt{3} & 0 & 2 & 0 \\ 0 & -2 & 0 & \sqrt{3} \\ 0 & 0 & -\sqrt{3} & 0 \end{pmatrix} \qquad \textbf{[A.11]}$$

$$\hat{S}_z = \begin{pmatrix} 3/2 & 0 & 0 & 0 \\ 0 & 1/2 & 0 & 0 \\ 0 & 0 & -1/2 & 0 \\ 0 & 0 & 0 & -3/2 \end{pmatrix}$$

[A.12]

Starting with $\hat{S}_Z$, operation on the spin state matrix gives,

$$\hat{\underset{\rightarrow}{H}}_z \left| \underset{\sim}{M}_D \right\rangle = \begin{pmatrix} D + \frac{3g\beta B_0}{2} & 0 & 0 & 0 \\ 0 & -D + \frac{g\beta B_0}{2} & 0 & 0 \\ 0 & 0 & -D - \frac{g\beta B_0}{2} & 0 \\ 0 & 0 & 0 & D - \frac{3g\beta B_0}{2} \end{pmatrix}$$

[A.13]

Because D = ~ 10-20 cm^{-1} for the $\{FeNO\}^7$ complex (1-3) and the typical X-Band EPR experiment uses energies on the order of ~ 0.3 cm^{-1}, excitations involving the M_S=+/-3/2 manifold are inaccessible. The 4 x 4 matrix can be reduced to,

$$\hat{\underset{\rightarrow}{H}}_z \left| \underset{\sim}{M}_D \right\rangle = \begin{pmatrix} -D + \frac{g\beta B_0}{2} & 0 \\ 0 & -D - \frac{g\beta B_0}{2} \end{pmatrix}$$

[A.14]

Solving for the eigenvalues by diagonalizing the 2 x 2 matrix gives the following eigenvalues:

$$\lambda = -D \pm \frac{g\beta B_0}{2}$$ **[A.15]**

The energy of excitations between the +/- spin states are given by,

$$\Delta\lambda = g\beta B_0$$ **[A.16]**

The effective g value observed for these excitations will be equal to g, ~ 2.

Excitations described by the $\hat{S}_y$ and $\hat{S}_x$ operators are subject to the same process and yield the following 2 x 2 matrices respectively,

$$\hat{\underset{\rightarrow}{H}}_y \left| \underset{\sim}{M}_D \right\rangle = \begin{pmatrix} -D & \frac{g\beta B_0}{i} \\ -\frac{g\beta B_0}{i} & -D \end{pmatrix}$$ **[A.17]**

and,

$$\hat{\underset{\rightarrow}{H}}_x \left| \underset{\sim}{M}_D \right\rangle = \begin{pmatrix} -D & g\beta B_0 \\ g\beta B_0 & -D \end{pmatrix}$$ **[A.18]**

Eigenvalues are,

$$\lambda = -D \pm g\beta B_0$$ **[A.19]**

With excitations between the +/- spin states now being,

$$\Delta\lambda = 2g\beta B_0 \qquad \textbf{[A.20]}$$

the effective g value observed for these excitations will be 2 x g = ~ 4.

APPENDIX B

Dock 6 Optimization. Figure 6.1 is the electrostatic spheres built by Dock6.

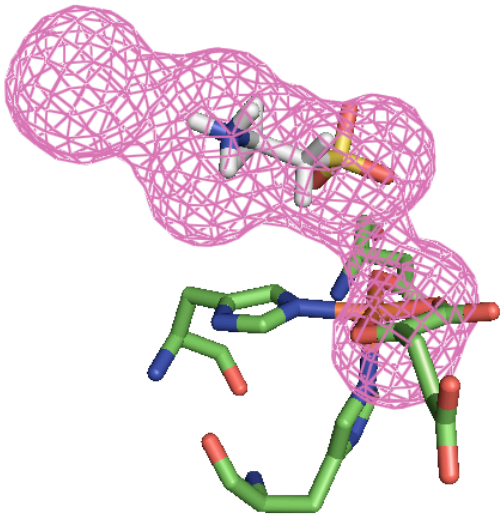

Figure 6.1. The pink mesh represents the space the taurine is allowed to move within during the Dock6 optimization **(4)**. Dock6 builds the mesh by using a water molecule to surface interactions with the surrounding protein. A surface of confinement is determined and the optimization orients the taurine molecule relative to the surface. The energy of the interactions is calculated as follows:

$$E = \sum_{i=1}^{lig} \sum_{j=1}^{rec} \left(\frac{A_{ij}}{r_{ij}^{a}} - \frac{B_{ij}}{r_{ij}^{b}} + 332 \frac{q_i q_j}{\varepsilon(r_{ij}) r_{ij}} \right) \quad \textbf{[B.1]}$$

The interaction energy (E) is a sum over all Van der Waals interactions between the "ligand" (taurine) and the "receptors" (surface contacts). Figure 6.2 is the predicted position for taurine relative to the Fe(II) complex made by Dock6.

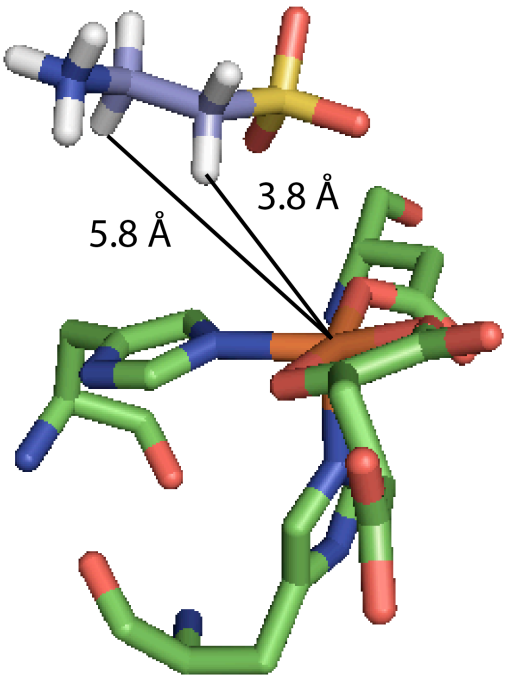

Figure 6.2. Measurement of taurine's C1 and C2 protons predicted by Dock6 optimization of the 1GY9 crystal structure. Special thanks to Rahul Banerjee and Dr. Robert Cukier for assistance with the optimization.

APPENDIX C

The simulated annealing **(5)** algorithm updates a temperature parameter as the optimization proceeds. Each generation, a number of parameter sets are randomly generated within a range specified by the user that surrounds the initially guessed parameters. The probability of choosing a parameter set out of a generation as the "best" parameter set is weighted by the temperature and the difference in χ^2 between that parameter set and the previous "best" parameter set. An "initial temperature" (T_0), an initial guess for the parameter values, and a temperature updating schedule are specified by the user. In this case, a logarithmic updating schedule is used. The optimization occurs in generations, the user specifies how many parameter sets should be tested in each generation. The χ^2 is calculated as,

$$\chi^2 = \sum_i \frac{\left(y_i^{data} - y_i^{simulation}\right)^2}{\sigma_i^2} \qquad \textbf{[C.1]}$$

and the difference in χ^2 is calculated as,

$$\Delta = \chi_i^2 - \chi_{Best}^2 \qquad \textbf{[C.2]}$$

The temperature (T_i) for each generation is updated by dividing the initial temperature (T_0) by the log of the annealing parameter (K_i), usually defined as the iteration number.

$$T_i = \frac{T_0}{\log(K_i)} \qquad \textbf{[C.3]}$$

The probability (P_i) that each parameter set (i) is chosen as the "best" parameter set for the generation it occurs in is given by:

$$P_i = \frac{1}{1 + \exp\left(\frac{\Delta}{T_i}\right)} \qquad \textbf{[C.4]}$$

The parameter sets that are closer to the "best" χ^2 have a higher probability of being chosen but, when the temperature is high, the parameters that result in a higher χ^2 also have a non zero probability of being chosen. In this way the simulated annealing algorithm can climb out of minima instead of getting stuck in the first minimum it finds. This helps avoid local minima in search of the global minimum.

APPENDIX D

MATLAB Code fragments:

See www.easyspin.org for detailed instructions for using the EasySpin **(6)** software package.

Fitting CW spectra. The following code will load your experimental spectrum, calculate a simulated CW EPR spectrum using EasySpin **(6)** with what has been specified in the "Sys0." and "Exp." fields, and attempt to optimize the variables specified in the "Vary." field to more closely match your spectrum using the "esfit" function. The numbers given in the "Vary." field are the +/- allowance for each parameter that is being varied.

```
clear
[B,spc,Params]=eprload('filename');

Sys0.S=3/2;
Sys0.g=[2.023,2.0059];
Sys0.D=[300000, 5000];
Sys0.lwpp=3.21;

Vary.g=[0.02,0.003];
Vary.D=[0, 2990];
Vary.lwpp=2;

Exp.mwFreq=9.4636;
Exp.CenterSweep=[250 300];
Exp.nPoints=1024;
Exp.Temperature=4;
Exp.ModAmp=1;

esfit('pepper',spc,Sys0,Vary,Exp,[],FitOpt)
```

Processing data, simulating spectra, and fitting to data.

This code will load the data using the EasySpin **(6)** function "`eprload`", correct the phase of time domain data, and select the real part of the data.

```
[B,spc]=eprload('filename');

im=imag(spc);
re=real(spc);
equals=im+re;
data=equals/max(equals);
```

This code will process the data by subtracting a 3rd order baseline, applying a hamming window, and zero filling by a factor of "`fillfac`".

```
%DATA FFT PROCESS
pcoeff= polyfit(B,data,3);
baseline= polyval(pcoeff,B);
norm(:,1)= B;
norm(:,2)= data-baseline(:,1);
timedata(:,1)=norm(:,1)-norm(1,1);
timedata(:,2)=norm(:,2);
amp=0.;
for i=1:length(norm)
   time1(i)=norm(i,1);
   amp1(i)=norm(i,2);
end;
npts=length(norm);
dcval=sum(amp)/npts;
for i=1:npts
   tprime1(i)=time1(i)-time1(1);
   cramp1(i)=amp1(i)-dcval;
end
%now begin the fft process, first the data are treated with a
hamming window
for i=1:npts
   wt=0.54+0.46*cos(tprime1(i)*pi/tprime1(npts));
   wamp(i)=wt*cramp1(i);
end
%zero fill factor
fillfac=2;
%
for i=1:fillfac*npts,
   pspec(i)=0.;
end
```

This code uses the cross term averaging procedure detailed in the paper by Vandoorslaer, et al. **(7, 8)** to average out line shape distortions introduced by taking the absolute value of the Fourier transformed spectra.

```
%cross term averaging steps
nsteps=10;
for ist=1:nsteps,
   YY=fft(wamp, fillfac*npts);
   for i=1:fillfac*npts,
      pspec(i)=pspec(i)+(real(YY(i)))^2+(imag(YY(i)))^2;
   end
   for k=1:npts-ist,
      wamp(k)=wamp(k+1);
   end;
   for k=npts-ist+1:npts,
      wamp(k)=0.;
   end;
   end;
yval=sqrt(pspec);
fm=1000/(tprime(2)-tprime(1));
frinc=fm/(fillfac*npts-1);
for i=1:fillfac*npts,
xval(i)=(i-1)*frinc;
end
datax=xval;
datay=yval;
```

This code can be added to a script using the above processing code to calculate simulated data using EasySpin **(6)**. You can process the simulated data in an identical fashion and this code will calculate a χ^2 (`res`) for comparison to the data. The χ^2 (`res`) value will be used by fitting algorithms to perform the optimizations.

```
Exp.Sequence = '3pESEEM';
Exp.mwFreq = 9.682;
Exp.Field= 320;
Exp.tau= .148;
Exp.dt = 0.012;
Exp.nPoints = 512;
Exp.ExciteWidth = 100;
Exp.T = 0.040;
Sys.S = 3/2;
Sys.D = [300000, 0];
Sys.g = [2.023,2.023,2.0057];
    Sys.Nucs = '2H';
    Sys.A_=[0, variables(1), 0];
    Sys.Apa=[0, variables(2), 0];
    Sys.Q=[variables(3), 0];
    Sys.Qpa=[0, variables(4), variables(5)];
[simx,simy]=saffron(Sys,Exp,Opt);
for ipt=fmin(ispec):fmax(ispec)
        if(ispec==1)
        res=res+((datay(ipt)-simy(ipt))^2)/(sig^2);
        end;
```

The following code will call any optimization script named "`fit`" for the specified algorithm (`simulannealbnd`). The initial guess for "`variables`" and each parameter set the algorithm generates and tests will be fed into a script having the same code shown above to calculate the various simulated spectra used to calculate χ^2. See the MATLAB documentation for how to set up and use the algorithms.

```
lb=[.19,.05,.18,.05,.05]; %lower bounds for varying parameters
ub=[0.27,1.57,0.25,1.57,3.14]; %upper bounds for varying
parameters
variables=[.23,.75,.215,.75,1.57]; %initial guess for parameters
options=saoptimset('Display','iter'); %list of options specified
by the user
bestvars=simulannealbnd(@fit,variables,lb,ub,options)
```

Statistical Analysis.

The following code will build the matrix containing the χ^2 distribution in each parameter that can be used to plot parameter value vs. χ^2 plots. It can use the same optimization script "fit":

```
function [var,res] = xdr(vars,varst,varen)

index=50; %number of points in the interval
res=zeros(index,length(vars)); %res matrix
var=zeros(index,length(vars)); %var input matrix

for k=1:length(vars)
    xdL=vars; %the changing parameters
    start=varst(k);
    endpt=varen(k);
    linc=(endpt-start)/index;
        for i=1:index
            xdL(k)=((i-1)*linc)+start;
            var(i,k)=xdL(k);
            res(i,k)=feval(@fit,xdL);
        end
end
```

The parabolic plots were fit to Equation D.1:

$$y_i = \frac{1}{e^{\left(-\frac{1}{2}\left(\frac{\left(x_i - x_{median}\right)}{\sigma}\right)^2\right)}} \qquad \textbf{[D.1]}$$

The parameter values (x), and the residual values (y) were supplied from the optimizations and the σ value was manually adjusted to fit the parabolic plot.

Figure 7.1 is a plot of χ^2 vs. each parameter value built with the above script for ESEEM data on the C1 ^{2}H on taurine.

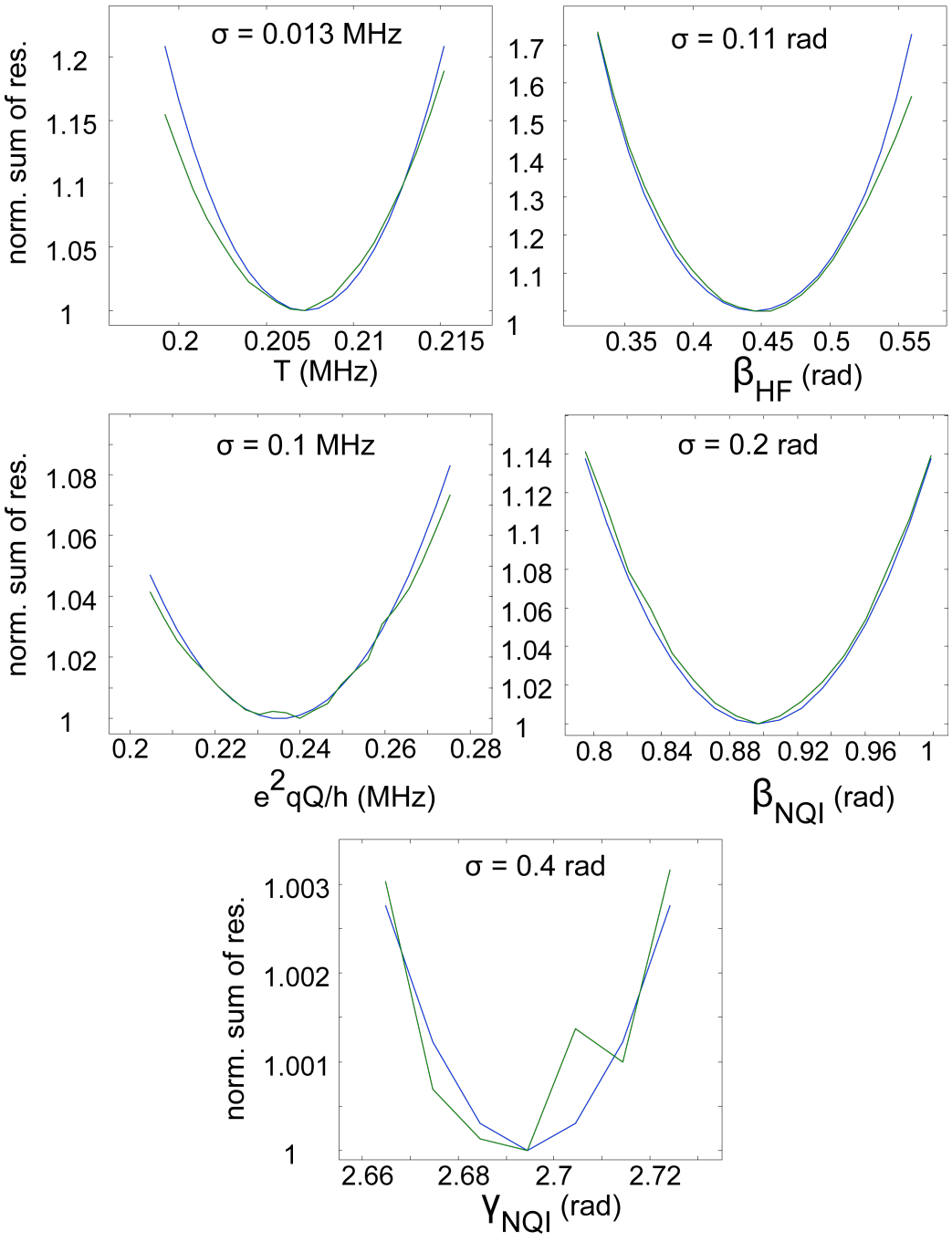

Figure 7.1. Each plot represents the adjustment of one parameter while holding constant all others. The residuals across all the data were summed and plotted against the parameter value. Each parabolic plot was manually fit to the exponential function Equation D.1.

Figure 7.2 is a plot of χ^2 vs. each parameter value built with the above script for ESEEM data on the C2 ^{2}H on taurine.

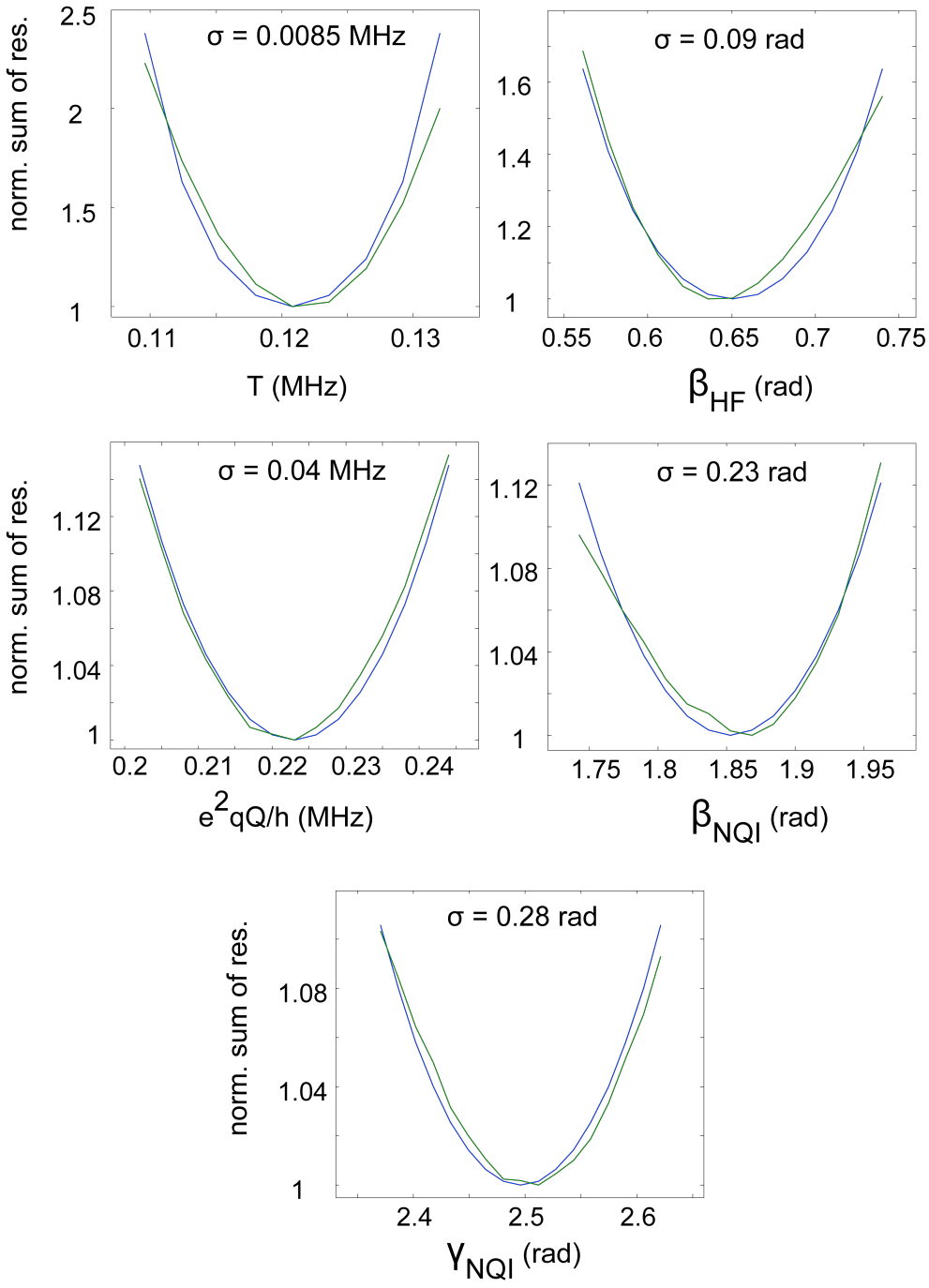

Figure 7.2. Each plot represents the adjustment of one parameter while holding constant all others. The residuals across all the data were summed and plotted against the parameter value. Each parabolic plot was manually fit to the exponential function Equation D.1.

Figure 7.3 is a two dimensional parameter correlation plot that can also be constructed from the data used to make the plots in Figures 7.1 and 7.2.

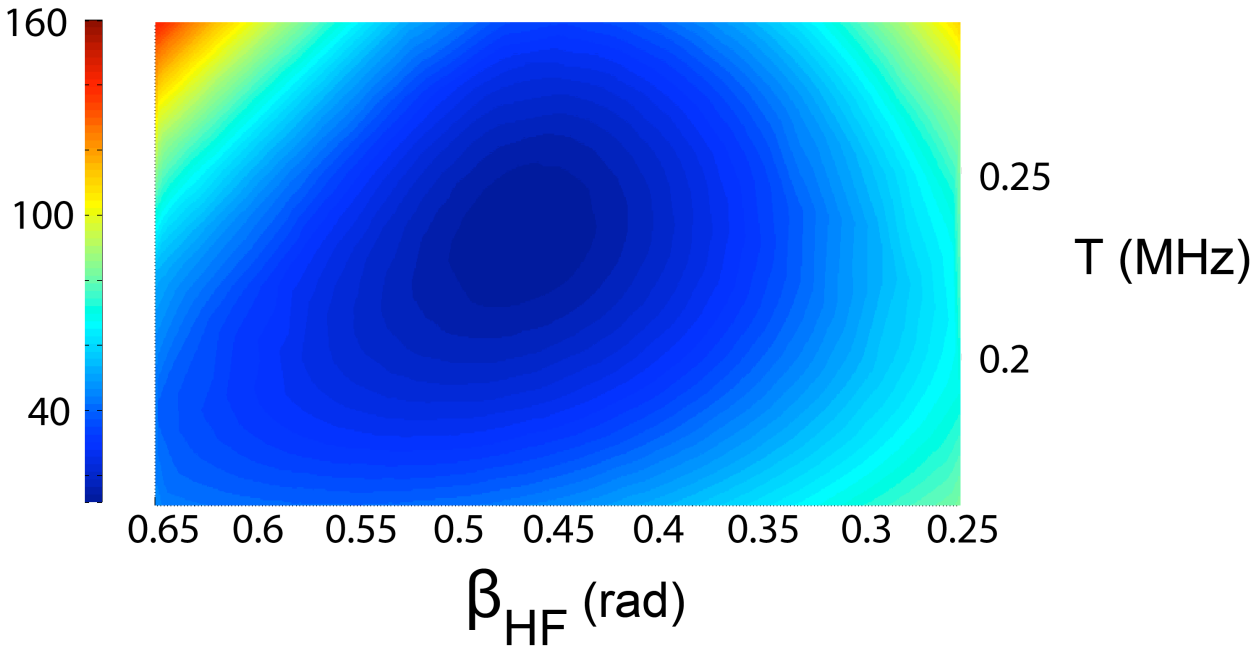

Figure 7.3. The same data used to make the plots in Figures 7.1 and 7.2 can be plotted against each other to form a 2 dimensional correlation plot. A clear minimum well is observed where the "best" values for each of the parameters intersect.

The following code will calculate covariance matrix (`Cov`) and use it to estimate a standard deviation (`std`) in each parameter. The code can call the same optimization script "`fit`" but the script must be modified (`fit*`) to output a vector containing the residual for each individual point as opposed to a single sum of residuals:

```
function [resids,std,Cov,Cor]=fitstats(estimates)

weights=1; % all parameters are weighted equally
fit=feval(@fit*,estimates);
resids=sum(fit(:).*fit(:))/(length(fit(:))-length(estimates));
% Calculate the jacobian matrix using a central difference
approximation
lx = length(estimates);
J  = zeros(length(fit(:)),lx);
dx=[.01,.1,.01,.1,.1];
for k = 1:lx
    xdp = estimates;
    xdm = estimates;
    xdp(k) = xdp(k)+dx(k);
    xdm(k) = xdm(k)-dx(k);
    rd = feval(@fitstatsres,xdp);
    rc = feval(@fitstatsres,xdm);
    J(:,k)=((rd-fit)+(rc-fit))/(2*dx(k)));
end
% Calculate the covariance matrix
Cov=resids*(J'*diag(weights(:))*J)^-1;
% calculate the standard deviation of the parameters
std=sqrt(eig(Cov));
Cor = Cov;
for j=1:lx
    for i=1:lx
    Cor(j,i)=Cov(j,i)/(std(j)*std(i));
    end
end
end
```

The shape of the parabolic wells in Figures D.1 and D.2 were used to estimate the appropriate step size "`dx`" for each parameter in the central difference approximation. With a χ^2 surface that has many local minima, a step size that is too large could result in sampling points in two closely spaced minima wells for the upward and downward step as opposed to within a single well. At the end, this script also computes the correlation matrix (`Cor`) but this was not examined in this study.

HYSCORE.

This code will calculate HYSCORE spectra using EasySpin **(6)** with a specified A_{iso}, T and β_{HF} for as many field positions and corresponding τ values as are specified and add them to display a single plot consisting of all the spectra together:

```
function [xx,yy,zz]=HYSCOREadd(Aiso,T,beta)
field=[170,...];
tau=[.14,...];

zz=0;
for i=1:length(field)

Exp.Sequence= 'HYSCORE';
Exp.Field = field(i);
Exp.tau = tau(i);
Exp.mwFreq= 9.68;
Exp.dt= .020;
Exp.nPoints= 128;
Exp.ExciteWidth= 100;

Sys.Nucs= '1H';
Sys.S=3/2;
Sys.D=[300000 0];
Sys.g= [2.023,2.023,2.0059];

Sys.A_=[Aiso,T];
Sys.Apa=[0,beta,0];

Opt.ZeroFillFactor=2;
Opt.nKnots=91;
Opt.ProductRule=0;

[x,y,p,d]=saffron(Sys,Exp,Opt);

zz=zz+(d.fd./max(max(d.fd)));

end

xx=d.f1;
yy=d.f2;
minu=0;
maxu=20;

contour(xx,yy,zz);grid 'on';xlim([minu maxu]);ylim([minu maxu]);
```

BIBLIOGRAPHY

BIBLIOGRAPHY

1. Aquino, F., and J. H. Rodriguez. 2009. Accurate Calculation of Zero-Field Splittings of (Bio)inorganic Complexes: Application to an {FeNO}(7) (S=3/2) Compound. J Phys Chem A 113:9150-9156.

2. Ye, S. F., J. C. Price, E. W. Barr, M. T. Green, J. M. Bollinger, C. Krebs, and F. Neese. 2010. Cryoreduction of the NO-Adduct of Taurine:alpha-Ketoglutarate Dioxygenase (TauD) Yields an Elusive {FeNO}(8) Species. J Am Chem Soc 132:4739-4751.

3. Brown, C. A., M. A. Pavlosky, T. E. Westre, Y. Zhang, B. Hedman, K. O. Hodgson, and E. I. Solomon. 1995. Spectroscopic and Theoretical Description of the Electronic-Structure of S=3/2 Iron-Nitrosyl Complexes and Their Relation to O-2 Activation by Nonheme Tron Enzyme Active-Sites. J Am Chem Soc 117:715-732.

4. Mazumder, D., and D. A. Case. 2007. AMBER Score in DOCK6: Application of molecular dynamics simulations and implicit solvent model (GB/SA) in protein-ligand docking. Abstr Pap Am Chem S 233:20-20.

5. Kirkpatrick, S., C. D. Gelatt, and M. P. Vecchi. 1983. Optimization by Simulated Annealing. Science 220:671-680.

6. Stoll, S., and A. Schweiger. 2006. EasySpin, a comprehensive software package for spectral simulation and analysis in EPR. J Magn Reson 178:42-55.

7. Van Doorslaer, S., G. A. Sierra, and A. Schweiger. 1999. Dead time-dependent line distortions in absolute-value electron spin echo envelope modulation spectra. J Magn Reson 136:152-158.

8. Mims, W. B. 1984. Elimination of the Dead-Time Artifact in Electron Spin-Echo Envelope Spectra. J Magn Reson 59:291-306.